JAERI-M
92-041

JAPANESE CONTRIBUTION OF ITER PF

SYSTEMS DESIGN DURING CDA

March 1992

Masafumi AZUMI, Mitsuru HASEGAWA[*1], Akihisa KAMEARI[*2]
Ken'ichi KURIHARA, Yukiharu NAKAMURA, Satoshi NISHIO
Yasuo SHIMOMURA, Kichiro SHINYA[*3], Masayoshi SUGIHARA
Minoru YAMANE[*1] and Ryuji YOSHINO

日 本 原 子 力 研 究 所
Japan Atomic Energy Research Institute

Japanese Contribution of ITER PF Systems Design during CDA

Masafumi AZUMI[+], Mitsuru HASEGAWA[*1], Akihisa KAMEARI[*2]

Ken'ichi KURIHARA[++], Yukiharu NAKAMURA[+], Satoshi NISHIO

Yasuo SHIMOMURA, Kichiro SHINYA[*3], Masayoshi SUGIHARA

Minoru YAMANE[*1] and Ryuji YOSHINO[+]

Fusion Experimental Reactor Team

Naka Fusion Research Establishment

Japan Atomic Energy Rsearch Institute

Naka-machi, Naka-gun, Ibaraki-ken

This report presents the brief summary of major part of Japanese contributions to the poloidal field coil systems design during CDA. Study of layout of poloidal field coil system is done to determine the coil location, which is consistent with various engineering constraints, such as extraction of in-vessel component, maintenance of PF coil itself, stored energy of PF coil system. Effects of plasma triangularity and current profile are examined. Alternative configurations such as semi-double null and single null divertor plasmas apart from the reference double null plasma are studied. Magnetic line tracing study is done for the detailed examination of the divertor plasmas. Repulsive force on the center solenoid for the volt-second saving operation scenario is evaluated. Study on typical operation scenarios is presented. General criteria of vertical stability by passive structure are determined. Following these criteria, stability performance of two types of passive structure, saddle loop type and twin loop type, is studied. In-vessel coil current and voltage are evaluated required

+ Department of Fusion Plasma Research
++ Department of Fusion Facility
*1 Mitsubishi Electric Corporation
*2 Mitsubishi Atomic Power Industries., INC.
*3 Toshiba Corporation

for active control of plasma vertical position. TOLFEX method for the identification of plasma shape and position for the control of ITER plasma and its application to ITER are briefly summarized. Control of horizontal plasma position during breakdown is examined. Attempts are made on the development of slow control algorithm for the plasma shape. Two typical means to reduce the effective divertor peak heat load are studied. Separatrix sweeping both by SC coils and in-vessel coils is examined. Feasibility to generate the ergodic magnetic layer by in-vessel coils for the vertical position control is also clarified. Simulation of plasma dynamic behavior after the thermal quench by TSC code is presented. Many of the results are not fully complete, while should be sufficient to demonstrate the feasibility of the CDA design. The studies are to be continued and deepened in future.

ITER（国際熱核融合実験炉）ポロイダルコイルシステムの概念設計
－ 日本からの貢献 －

日本原子力研究所那珂研究所核融合実験炉特別チーム

安積　正史[+]・長谷川　満[*1]・亀有　昭久[*2]・栗原　研一[++]
中村　幸治[+]・西尾　敏・下村　安夫・新谷　吉郎[*3]
杉原　正芳・山根　実[*1]・芳野　隆治[+]

　　本報告書は ITER（国際熱核融合実験炉）ポロイダルコイルシステムの概念設計に対する日本の貢献の主な結果をまとめたものである。ポロイダルコイル系の検討においては，まずその最適配置が各種工学的制約条件，例えば炉内構造物の引き抜き，コイル自身の保守，蓄積エネルギーなど，を考慮して決められた。さらにプラズマ三角度や電流分布の効果が調べられた。代替の配位である準ダブルヌル配位やシングルヌル配位が検討された。ダイバータプラズマの性能検討のために磁力線の精密な追跡がなされた。磁束節約運転シナリオにおける中心ソレノイドコイルに働く反撥力が求められた。次にプラズマ垂直位置制御の検討においては，最初に一般的な安定性の指針が導出され，これに従って二種類の受動安定化シェルの性能評価が行なわれた。また能動制御に関して簡単な検討が行なわれた。プラズマ制御に関しては，まず代表例として TOLFEX 法によるプラズマ位置・形状同定法の ITER への適用が検討された。さらにブレークダウン時のプラズマ水平位置の制御法が調べられ，また遅い制御法に関するアルゴリズムが開発された。次にダイバータの熱負荷を低減する手段としてセパラトリックス掃引と周辺磁気面のエルゴード化についての検討がなされた。最後に TSC コードによるディスラプション時の熱クエンチ後のプラズマの動的挙動のシミュレーションの検討を示した。これらの検討結果の多くはまだ完全なものではないが，ITER の成立性を示すための概念設計としては十分なものであり，その概念確立に大きく寄与したものである。これらの検討は EDA（工学設計活動）において継続され，さらに深められる予定である。

那珂研究所：〒311－01　茨城県那珂郡那珂町大字向山801－1
＋　　　炉心プラズマ研究部
＋＋　核融合装置試験部
＊１　三菱電機㈱
＊２　三菱原子力工業㈱
＊３　㈱東芝

Contents

目　　　　次

1. Introduction

ITER Conceptual Design Activity (CDA) has been carried out for three years and completed in 1990, during which technical feasibility of the ITER has been extensively examined and consistent conceptual design has been performed. This report presents the brief summary of major parts of Japanese contributions to the poloidal field coil systems design during CDA. More detailed descriptions of each of the contribution have already been reported separately elsewhere. Some part of the PF related issues are not covered in this report. They should be covered in the reports of other groups, which is more directly related and appropriate. Many of the study done have contributed largely to the ITER CDA, and, in fact, have been incorporated into the CDA final report [1].

In the following, brief descriptions of each chapter are presented. In Chap. 2, study of layout of poloidal field coil system is done to determine the coil location, which is consistent with various engineering constraints, such as extraction of in-vessel component, maintenance of PF coil itself, stored energy of PF coil system. Effects of plasma triangularity and current profile are examined. Alternative configurations such as semi-double null and single null divertor plasmas apart from the reference double null plasma are studied. Magnetic line tracing study is done for the detailed examination of the divertor plasmas. Repulsive force acting on the center solenoid for the volt-second saving operation scenario by lower hybrid waves is evaluated. Brief summary of the typical operation scenario is presented.

In Chap. 3, study of vertical position control is presented. First, general criteria of vertical stability by passive structure for the growth rate and the stability margin are determined. Following these criteria, stability performance of two types of passive structure, saddle loop type and twin loop type, is studied. Study of active control of plasma vertical position with use of twin loop shell is presented to identify the required capacity of the power supply systems.

In Chap. 4, plasma control issue is presented. First, as an example, the TOLFEX method for the identification of plasma shape

and position for the control of ITER plasma and its application to ITER are briefly summarized. Then, the control of horizontal plasma position during breakdown is examined. Attempts are made on the development of slow control algorithm for the plasma shape, which is based on the non-interfering control algorithm.

In Chap. 5, two typical means to reduce the effective divertor peak heat load are studied. Separatrix sweeping both by SC coils and in-vessel coils is examined to identify the effectiveness and engineering limitation of the method. Feasibility to generate the ergodic magnetic layer by in-vessel coils for the vertical position control is also examined.

In Chap. 6, simulation study of the plasma dynamic behavior after the thermal quench by TSC code, which includes the consistent plasma behavior with the simplified shell models, is presented. Brief summary is presented in Chap. 7.

2. Plasma Configuration and Operation

2.1 Outline

Hybrid poloidal field coil system was employed for the ITER as is usual in the recent tokamak reactor design. Study on the minimum number of PF coils and their optimum locations were carried out to control plasma shape and position for various combinations of plasma parameters, such as poloidal beta, internal inductance, elongation, triangularity and available volt-second. Partition of the center solenoid is another important point of shaping control and is connected closely to the minimization of useless magnetic field leakage into the plasma region at plasma current initiation and early startup phases.

Effect of the triangularity of the plasma cross section was emphasized from the view point of maximizing available volt-second and minimizing stored energy of PF coils. Engineering constraint, such as allowable coil current density and maximum magnetic field experience, was also included in the study. Final decision of the triangularity was made so that the resultant location of the null point was compatible with the reactor structure.

Further study of maximizing available volt-second was carried out for the definite plasma shape but different poloidal beta and internal inductance within the limit of the engineering constraint. The study showed that the optimum design was attained for the most probable plasma current distribution from the view point of volt-second maximization.

Although a double null (DN) divertor plasma is a reference for ITER, both semi-double null (SDN) divertor plasma and single null (SN) divertor plasma were also investigated for alternatives. Heat load onto divertor plate is a main discussion point for these different plasma configurations.

Precise tracing of magnetic line of force was made on the separatrix and several neighboring magnetic surfaces outside the plasma. The study provides information about many equilibrium quantities, such as ratio between poloidal and toroidal magnetic fields and expansion of the magnetic surface near the divertor plate.

Problem of repulsive forces acting on the center solenoid coils was investigated. The force becomes remarkable when the volt-second saving by non-inductive current drive is employed.

Finally, plasma operation scenario was developed based on the idea, in which plasma gradually increases its major and minor radii, elongation and triangularity, starting from circular plasma limited by inside first wall through elongated non-circular plasma and reaching at the final divertor plasma configuration. Relatively smooth time evolution of the PF coil currents was attained.

It should be noted that coils are treated as a single-turn coil in the following description, so that a notation of coil current also means ampere-turns of the coil. Another noticeable point is that some part of design studies in this chapter are carried out for the final design parameters and structure, which are slightly different from those of ITER.

More detailed discussions and descriptions for several parts of the results in this chapter are presented in Ref. [2].

2.2 Layout of poloidal field coil (PFC) system

Intensive and systematic study was carried out to investigate optimum PFC layout that consists of minimum number of coils with small amount of electric power requirement regarding both total power of the system and powers for individual coils. Studies were made in such a manner that any coils are eliminated from an initial coil layout in which coils are distributed almost continuously around the plasma.

The work was carried out as a preparatory study, so the plasma parameters and reactor structure are different from the final ITER design. Although the center solenoid is designed as a straight cylinder in ITER because of the easy maintenance of the solenoid, oval shape solenoid, which can fit an oval shape TFC with benefit of mechanical support, was also investigated for comparison.

Final PFC layout obtained in the above manner consists of seven coils in both the upper and lower halves of the reactor structure whose current can be controlled independently. Four of them constitute a straight center solenoid and are equally separated

for the reason described in the next paragraph. Three other coils act mainly as equilibrium coils, and three is a minimum number that can control plasma shape for wide range of poloidal beta and internal inductance. Two of three coils should exist at major radii larger than the major radius of the plasma. This point is inevitable for shaping plasma cross section adequately.

Partitioning of the center solenoid should also match the other two aspects, i.e., reactor structure and minimization of useless stray magnetic field into plasma region in early stage of plasma startup. From the view point of plasma shaping two coils are required to locate in the extent of the plasma height, but minimization of the stray field claims larger solenoid length than plasma height. Matching with the TFC height imposes four-coil partitioning of the center solenoid in the present ITER design. Two coils located at the end of the solenoid are not indispensable to plasma shaping.

Final locations of the poloidal field coils are shown in Fig. 2.2-1 and Table 2.2-I. Two outermost coils (PF6 and PF7) are located at the same major radius but different height because of the easy removal for the maintenance of these coils. This layout has increased ampere-turns and stored energy of PF6.

2.3 Effect of triangularity

There are two typical shaping parameters in tokamak plasma configuration study. Most decisive parameter is elongation of plasma cross section, and is determined by confinement and MHD stability studies. The other is triangularity, which has rather secondary effect on the above aspects but has definite effect on the coil ampere-turns and electric power requirement.

Available volt-second was investigated for the same plasma parameters and PFC configuration that were employed in the preparatory study described in the preceding section. Engineering constraint on the allowable current density and magnetic field experience of the super-conducting magnet was imposed in the investigation. Total stored energy and total ampere-turns were also evaluated for that volt-second.

Figure 2.3-1 depicts three types of the solenoid whose

performances were tested, and Fig. 2.3-2 show the triangularity dependencies of the total stored energy and available flux swing (volt-second). Dependence of the total ampere-turns on the triangularity is shown in Fig. 2.3-3. From the view point of minimizing both total stored energy and total ampere-turns, triangularity of 0.4 or more is preferable, but available flux swing is rather limited in this high triangularity region. Considering suitability for the rector structure such as divertor plate setting, selecting triangularity of the range from 0.3 to 0.4 has a benefit. Final design employs 0.4 as a triangularity.

2.4 Effect of plasma current profile on available volt-second

Effect of plasma current profile on the available volt-second was investigated for the plasma shape with elongation of 2.0 and triangularity of 0.4. The elongation and triangularity are measured at the 95% flux surface. In this study major radius of the plasma is 5.8m and minor radius is 2.2m, so the aspect ratio is somewhat smaller than that of the final plasma parameter.

Poloidal field coil current can be represented by a linear combination of the linkage flux supplied by PF coils (Ψ_p), poloidal beta (β_p) and internal inductance (l_i) as the following. Coefficients are constant for fixed plasma shape but are different for different coils.

$$I = c_1 \Psi_p + (c_2 \beta_p + c_3 l_i + c_4) I_p \qquad (2.4\text{-}1)$$

Table 2.4-I summarizes the coefficients for PF1, PF2 and PF3. Reactor structure imposes a rigid constraint on the maximum currents of the super-conducting solenoid coils. Among the solenoid coils PF1 and PF2 have decisive effect on the plasma shaping and are most sensitive to the change in poloidal beta and internal inductance. Linear programing was applied for evaluating maximum volt-second within a limit of the coil currents. Maximum current in the negative direction for 12T magnetic field experience is -20.5MAT if the solenoid coils are not graded.

Figure 2.4-1 shows operation regions for two different poloidal beta values. For both cases maximum volt-seconds are limited by

PF1 and PF2, though PF1 and PF3 seem to limit the volt-second at further high β_p. In the range of β_p investigated here, the maximum value is attained at internal inductance of about 0.6, which is somewhat smaller than the ITER reference value and corresponds to a plasma current profile with safety factor of about unity on the magnetic axis.

Figure 2.4-2 depicts variations of the maximum volt-second and internal inductance, at which volt-second attains maximum, as a function on β_p. Available volt-second increases as β_p becomes large because of an increase of the equilibrium magnetic field at higher β_p, which is associated with an increase of external flux linkage without increasing solenoid coil currents.

Initial magnetization of the solenoid coils is 93vs for maximum field experience of 12T. Total flux swing amounts to about 275vs when poloidal beta is 1 at the end of burn. Preliminary study of grading of the solenoid coils showed that grading increases the maximum coil current up to about 22MAT, which adds available volt-second by amount of $\Delta I/c_1=-7.5vs$.

2.5 SDN/SN alternatives

Although the ITER reference is a double null divertor plasma, alternative configurations, e.g., semi-double null (SDN) or single null (SN) divertor plasma were also examined. Generally, total stored energy or total ampere-turns of the poloidal field coils becomes minimum for single null divertor plasma with appropriate up-down asymmetry. No qualitative difference between SDN and SN is not observed, because SN is a smooth deviation from DN that passes through SDN.

Level of the up-down asymmetry can be measured by the ratio of flux differences between magnetic axis and passive separatrix to that between magnetic axis and active separatrix. Figure 2.5-1 shows dependencies of the total stored energy and total ampere-turns on the level of up-down asymmetry. Choosing a value around 1.1 for the ratio is optimum on the view point of minimizing electric power rating of the poloidal field coils.

Typical plasma configurations are depicted in Fig. 2.5-2. In the

single null divertor plasma passive separatrix is completely isolated from the active separatrix, which defines plasma surface, so heat flow is directed only to the divertor plate that intersects the active separatrix. The coil current profile is largely up-down asymmetric. On the other hand, coil current profile for the semi-double null divertor plasma is almost up-down symmetric, while heat flow is marginally directed to the divertor plate.

Another discussion point of SDN/SN alternatives is how to expand divertor space to attain cold and dense divertor plasma and to increase pumping speed at divertor throat. Single null divertor plasma seems to be preferable for this viewpoint, while the trade-off that total heat to the divertor region doubles still remains.

Several SN plasma options were investigated to select best match to the final ITER reactor structure. The options are summarized in Table 2.5-I. Except the SN3 and SN3b, geometrical safety factor is kept constant, while MHD safety factor measured at the 95% flux surface is slightly different. Level of the up-down asymmetry is selected to be almost 1.1. Location of the plasma is shifted upward to provide large divertor region, while PFC locations remain unchanged. Plasma configurations of DN and SN1b are shown in Fig. 2.5-3.

Figure 2.5-4 compares ampere-turns profile between double null plasma and typical single null plasmas (SN1, SN1b, SN3 and SN3b) at the same flux linkage of -195vs, which corresponds to the end of burn for the DN plasma. Apparent difference between DN and SN plasmas is large amount of decrease of the PF5U current for the SN plasmas, while others are relatively unchanged. Increase of PF1U current, though the amount is still small, will reduce available volt-second.

Total energy and ampere-turns are compared between DN and SN plasma options in Fig. 2.5-5. Reduction of these values from the values of DN can clearly be seen. Same tendency for the AT-m, which is a measure of the amount of super conductor, is featured in Fig. 2.5-6.

One of the important parameters to evaluate SN plasma is separatrix separation, which is defined by the distance between active and passive separatrices measured on the median plane. If the separation is adequately large, both heat and particle flow will be

confined in the region between active and passive separatrices. The divertor plate will, therefore, collect all the heat and particles which flow into the scrape-off layer. If, on the other hand, the separation is not adequately large, some part of the heat and/or particles flows to the opposite side of the divertor plate and will damage the first wall, where the passive separatrix strikes.

Figure 2.5-7 illustrates a map of the options in the plane of separatrix separation and MHD safety factor at 95% magnetic flux surface. If we assume that the width of the particle flow is about 10 cm, SN1 and SN1b options seem to be adequate from the view point of separatrix separation.

Another important parameter is skew of the equilibrium magnetic field, $<K>$, which induces coupling between horizontal and vertical motions of the plasma in positional instability. Map is shown in Fig. 2.5-8 in the $<K>$ and $<n>$ space for both cases with and without aspect ratio correction. SN1b seems to be least unstable. The sign of a skew determines direction of the plasma motion in positional instability. If the sign is positive, inward displacement of a plasma due to e.g., thermal quench, leads to a vertical motion toward the divertor plate.

Finally, in conjunction with the SDN configuration, natural separation of the active and passive separatices due to the vertical drift is important, since the power scrape-off width at the midplane is fairly narrow, e.g., 3-5 mm for ignition operation and 1-2 mm for the steady state operation. Thus, even a small separation could lead to virtual SN configuration with respect to the heat load on the divertor. Fig. 2.5-9 shows the separatrix separation vs vertical displacement obtained by the equilibrium code. In this calculation, the boundary flux value is kept constant as the plasma is shifted vertically, which will correspond to the natural vertical displacement in a flux conserving manner. From this figure, it is seen that vertical displacement must be kept below 1 cm to keep the separation below 5 mm. It is expected that the control accuracy of the plasma vertical displacement within 1 cm will be marginally possible, while, actually, other direct monitor system of the divertor heat load should also be necessary in addition to the magnetic control scheme to balance the heat load on the upper and lower divertor plate, since some intrinsic physics processes producing the up/down asymmetry, such as grad B

drift effect, surely exist.

2.6 Magnetic line tracing for divertor plasma

Precise topology of the magnetic flux surface near the separatrix was investigated for the mechanical design of the divertor structure and for the divertor plasma analysis. Location of the magnetic line of force, strength of both poloidal and toroidal magnetic fields, lengths of the line from the starting point on the horizontal plane that has same height as the magnetic axis, etc., were calculated for the DN plasma by tracing the typical magnetic line of force. For SN plasma these quantities were calculated from one divertor plate to another plate around the plasma.

Figure 2.6-1 shows magnetic line tracing for the ITER physics baseline double null divertor plasma. The result of a typical SN option (SN1c) is depicted in Fig. 2.6-2. The ratio of the toroidal magnetic field to the poloidal magnetic field is about 20 at the location where the poloidal projection length is 1m from the null point to separatrix hitting point on the divertor plate, though the value changes significantly for the different length from the null point and different flux surfaces. This means that hitting angle of the magnetic line of force to the tangential of the plate decreases to 1 degree for the poloidal inclination of 20 degree.

2.7 Repulsive force on center solenoid

Although the current profile on the center solenoid can be flat at initial magnetization, it becomes distributed as plasma evolves because of the requirement of different equilibrium magnetic field component for each coil. For the ITER physics baseline plasma with final plasma shape, current profile on the center solenoid has its minimum (negative value) at a coil located near the median plane (PF1) and in many cases increases monotonically toward the edge coil (PF4).

If the two coils (PF1 and PF2) are connected in series or controlled in the same manner, PF2 current decreases (absolute

value increases because of its negative sign) and PF3 current, on the contrary, increases from the original value resulting in a large gap between PF2 and PF3 coil currents. At some linkage flux there occurs a situation that the absolute values of PF2 and PF3 coil current are equal but signs are different. At this moment repulsive force between PF2 and PF3 might become intolerably large.

For the same plasma shape this tendency is remarkable at low poloidal beta and high plasma current. Quantitative study of the repulsive force was made based on the formulation of the coil current derived from the equilibrium analysis. The formulation is represented in the following equation.

$$I = c_1 \Psi_p + (c_2 \beta_p + c_3 l_i + c_4)I_p \tag{2.7-1}$$

Variation of the linkage flux, Ψ_p, can be represented by subtracting inductive and resistive flux consumption from initial magnetization flux Ψ_{ini} such as

$$\Psi_p = \Psi_{ini} - (L_p + 0.4\mu_0 R_p - \phi_{sav})I_p , \tag{2.7-2}$$

where $\phi_{sav}I_p$ denotes volt-second saving by non-inductive current drive and Ejima's type of formulation of the resistive flux consumption (proportional to product of the major radius and the plasma current) is assumed. From equations (2.7-1) and (2.7-2) coil current can be represented as

$$I = c_1 \{\Psi_{ini} - (\bar{L}_p - \alpha - \phi_{sav})I_p\} \tag{2.7-3}$$

Finally, using the normalization summarized in Table 2.7-I coil current can be written in the following equation for each coil.

$$\bar{I} = \phi_{ini} - (\bar{L}_p - \alpha - \phi_{sav})\bar{I}_p \tag{2.7-4}$$

Repulsive force between two coils is estimated by the product of their coil currents. For the ITER case it is a product of PF2 and PF3 coil currents as follows:

$$\bar{F} = \bar{I}_2 \bar{I}_3 = (\bar{L}_p - \alpha_2 - \phi_{sav})(\bar{L}_p - \alpha_3 - \phi_{sav})(\bar{I}_p - \bar{I}_{pax})^2 + \bar{F}_0 \tag{2.7-5}$$

where

$$\bar{I}_{pax} = \frac{\bar{L}_p - \phi_{sav} - \dfrac{\alpha_2 + \alpha_3}{2}}{(\bar{L}_p - \alpha_2 - \phi_{sav})(\bar{L}_p - \alpha_3 - \phi_{sav})} \phi_{ini} ,$$

$$\bar{F}_0 = -\frac{1}{4}\phi_{ini}^2 \cdot \frac{(\alpha_2 - \alpha_3)^2}{(\bar{L}_p - \alpha_2 - \phi_{sav})(\bar{L}_p - \alpha_3 - \phi_{sav})} . \tag{2.7-6}$$

Since the force is represented as a parabolic equation and the axis is a function of volt-second saving, maximum force should be

verified in two categories. When the axis exists below $\tilde{I}_p = 1$, maximum value of the repulsive force occurs simply at the axis. On the contrary in the case that the axis locates beyond $\tilde{I}_p = 1$, maximum repulsive force will potentially appears at $\tilde{I}_p = 1$, i.e., at the SOFT (start of flattop). Table 2.7-II shows results of maximum values of the repulsive force for different volt-second savings. Series connection of PF1 and PF2 implies at least 5 times larger value of repulsive force will be imposed on the solenoid coils.

More detailed evaluation of the total repulsive force on the solenoid coil at SOFT including the contribution from all of the coils is shown in Fig. 2.7-1.

2.8 Operation scenario

Operation scenario for the ITER physics baseline plasma was studied to establish a relevant scenario within the engineering constraints, such as both maximum current density and field experience of the super-conducting magnet, voltage of the electric power supply, etc.

Plasma with a circular cross section of minor radius of 1m is initiated near the inner first wall and is limited by a material limiter. Plasma current is assumed to be ramped up to 500kA in 0.5 s with careful horizontal position control. After this level of the plasma current ramp-up is controlled at a rate of 0.5MA/s up to 10MA in 20 seconds. Minor radius gradually increases and the cross section is elongated up to 1.6 at the end of the limiter (EOL) discharge.

Limiter to divertor transition is done in the following 20 seconds, during which plasma current is also increased by 5MA. Once the divertor plasma is established, plasma keeps its cross section in spite of slight changes in poloidal beta and plasma current profile. Finally plasma reaches the reference shape and current 70 seconds after the plasma initiation, i.e., at the start of flattop (SOFT).

Table 2.8-I summarizes the operation scenario. Coil currents change gradually, except a few intervals for some coils, resulting in attainment of reasonable electric power supply voltage. Figure 2.8-1 shows the time evolution of the plasma configuration.

Table 2.2-I Dimensions and turns of poloidal field coils.

Coil No.	Rc (m)	Zc (m)	$\delta R(m)$	δZ (m)	Turns
PF1	1.725	0.95	0.65	1.84	550
PF2	1.725	2.85	0.65	1.84	550
PF3	1.725	4.75	0.65	1.84	550
PF4	1.725	6.65	0.65	1.84	550
PF5	3.9	8.9	0.9	0.9	400
PF6	11.5	6.0	0.5	1.5	320
PF7	11.5	3.0	0.5	0.9	200

Table 2.4-I Coefficients of coil current formulation.

Coil No.	C_1	C_2	C_3	C_4
PF1	0.19906	0.35818	-0.38875	0.58596
PF2	0.17424	0.26859	0.90119	-0.3227
PF3	0.25385	0.19998	1.1489	0.26122

Table 2.5-I Plasma parameters of DN and optional SN plasma.

	DN	SN1	SN2	SN2-1	SN3	SN1b	SN1c	SN3b
R_p	6.0	←	←	←	6.1	6.0	6.0	6.1
a	2.15	←	←	←	2.25	2.15	2.15	2.25
R_n	4.71	←	←	←	←	5.01	5.355	←
Z_n	-4.78	-4.78	←	←	-4.48	-3.98	-3.98	-3.78
κ	2.0	←	←	←	←	←	←	←
δU	0.4	0.36	0.16	←	←	0.36	0.36	0.16
δL	0.4	←	←	←	0.41	0.31	0.2	0.32

DN   Physics baseline plasma

SN1   Single null plasma with the same null point location as DN

SN2   Modification from SN1 by reducing triangularity of the upper half

SN2-1   PF1U and PF1L are connected in series. Plasma parameters are same as SN2

SN3   Expanded minor radius plasma of SN2 to recover q^Ψ with keeping position of inner plasma surface constant

SN1b   Null point is shifted outward and upward from SN1

SN1c   Null point is shifted further from SN1b

SN3b   NUll point is shifted outward and upward from SN3

Table 2.7-I Normalizations for repulsive force calculation.

Quantity	Normalization
Plasma current	$\tilde{I}_p = I_p/I_{p0}$
Coil current	$\tilde{I} = I/c_1 I_{p0}$
Initial Magnetization	$\phi_{ini} = \Psi_{ini}/\tilde{I}_{p0}$
Plasma inductance	$\tilde{L}_p = L_p + 0.4\mu_0 R_p$
Poloidal beta+Internal inductance	$\alpha = (c_2\beta_p + c_3 i + c_4)/c_1$
Repulsive force	$\tilde{F} = F/(c_{12}c_{13}I_{p0}^2)$

Table 2.7-II Maximum repulsive force for different Vs saving.

Case	PF1-PF2	Lp (μH)	α_2	α_3	Saving (Vs)	$\tilde{I}_p$	$\tilde{F}$	I_p (MA)	$\tilde{F}_{23}$ (MAT²)
No saving	Series	12.33	1.27	7.21	0.	0.726	-4.02	18.15	-78.61
	Separate	12.33	3.44	6.02	0.	0.688	-0.77	17.7	-14.75
Axis at SOFT	Series	12.33	1.27	1.27	23.35	1.0	-7.25	22.0	-109.69
	Separate	12.33	3.44	3.44	34.17	1.0	-1.59	22.0	-23.70
Complete saving	Series	12.33	1.27	1.27	66.35	1.0	-8.34	22.0	-126.16
	Separate	12.33	3.44	3.44	66.35	1.0	-0.25	22.0	-3.78
Maximum at SOFT	Series	12.33	1.27	1.27	50.97	1.0	-8.83	22.0	-133.56
	Separate	12.33	3.44	3.44	40.22	1.0	-1.66	22.0	-24.83

Table 2.8-I Physics Base Plasma

	Inl. Mag	BBD	ABD	A3S	A10S	EOL	SOD	SOFT	SOB	EOB	EOC	EOP
Time(sec)	0	0.1	0.5	3	10	20	~40	70	90	190	230	260
PF 1	17.88	17.63	16.65	13.86	8.42	-1.25	-9.50	-18.73	-17.84	-20.94	-20.54	-2.98
PF 2	17.75	17.51	16.53	13.76	8.36	2.60	-8.14	-19.14	-17.86	-20.58	-20.78	-2.62
PF 3	18.59	18.34	17.32	14.41	8.76	2.62	-1.26	-9.38	-16.36	-20.32	-13.37	-3.82
PF 4	18.67	18.41	17.39	14.47	8.80	1.23	1.39	-1.05	-1.79	-3.35	-4.00	-1.51
PF 5	5.16	6.07	5.24	4.28	2.40	4.39	11.33	14.69	14.12	12.84	7.93	-1.23
PF 6	0.83	0.82	0.42	-0.32	-0.46	-1.67	-7.92	-12.70	-11.14	-11.21	-8.56	-0.07
PF 7	0.02	0.02	0.02	-0.07	-0.94	-2.18	-0.80	-0.62	-3.33	-3.37	-1.48	-0.04
I_p (MA)	0.0	0.0	0.5	2.0	5.0	10.0	15.0	22.0	↓	↓	17.0	0.0
β_p			0.01	0.02	0.04	0.06	0.08	0.1	1.0	↓	0.1	
R_p (m)			4.25	5.19	5.54	5.64	5.80	↓	↓	↓	↓	
a (m)			0.80	1.74	2.09	2.19	2.20	↓	↓	↓	↓	
K			1.03	1.10	1.20	1.51	1.86	↓	↓	↓	↓	
δ			0.01	0.04	0.04	0.14	0.32	↓	↓	↓	0.30	
α_ℓ			0.74	0.71	0.70	0.63	0.70	0.66	0.63	↓	0.71	
L_p (μH)			11.25	9.71	9.31	8.15	8.63	8.47	9.09	↓	8.69	
q_Ψ			7.79	8.97	5.53	4.76	4.22	2.88	3.02	↓	3.70	
q (0)			4.99	5.25	3.07	2.26	1.26	1.21	0.85	↓	1.11	
Ψ_p (VS)	93.4	92.1	84.3	64.9	27.5	-22.0	-73.0	-137.0	-167.0	-182.6	-137.4	-15.0

Fig. 2.2-1 Cross-sectional view of ITER.

(a) Straight Solenoid

(b) Mild Oval Solenoid

(c) Strong Oval Solenoid
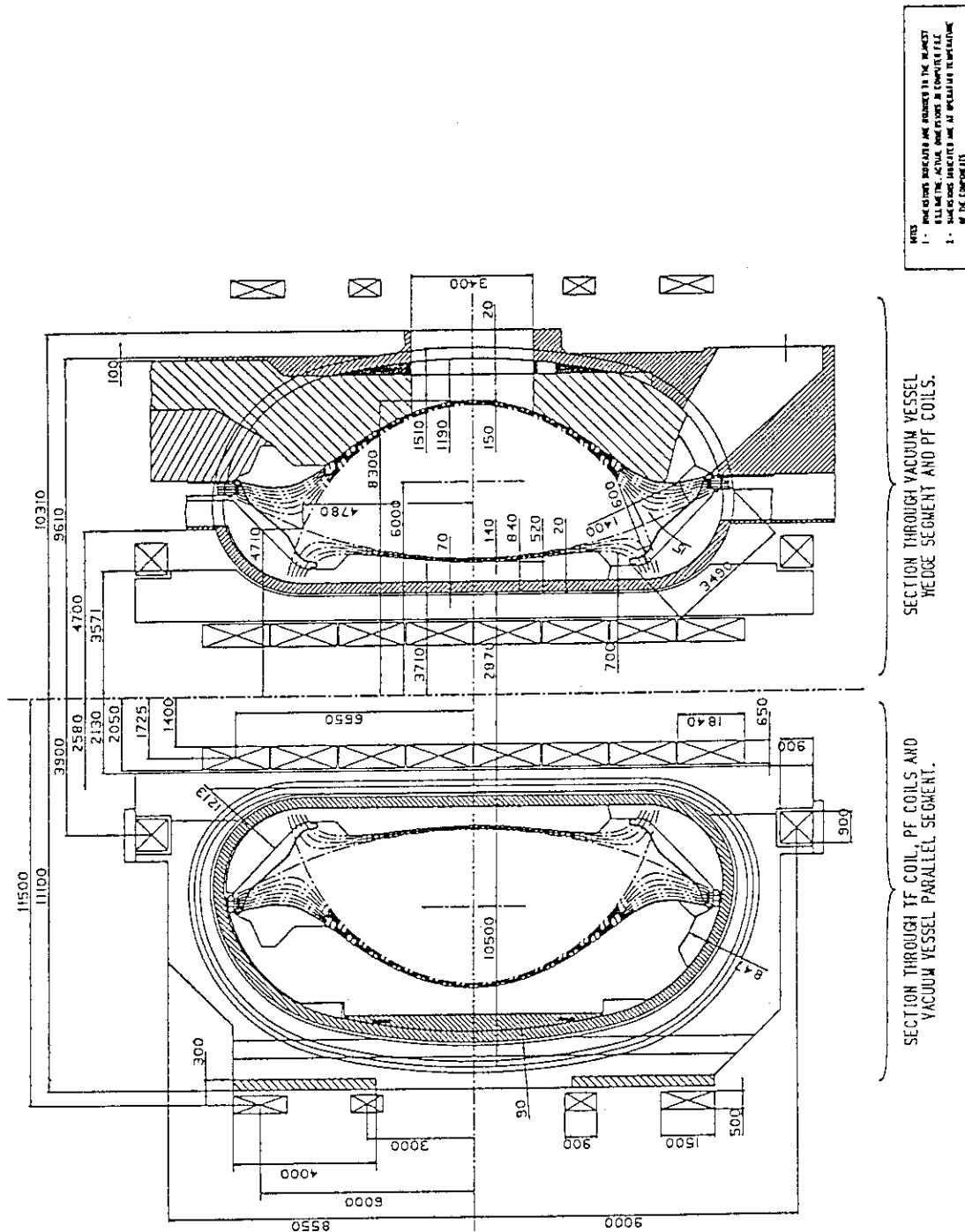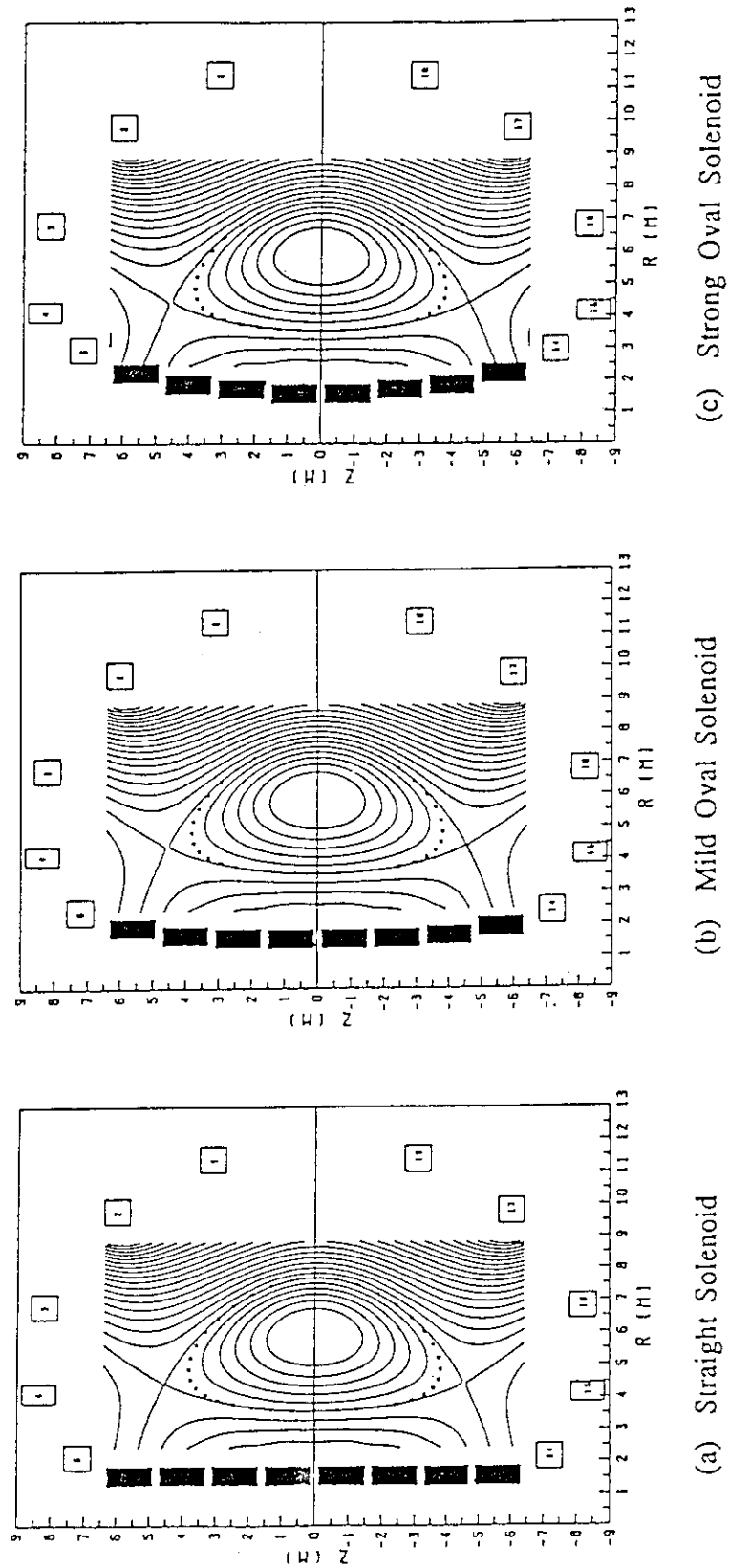
Fig. 2.3-1 Three types of the solenoid shape whose electric performance were examined.

Fig. 2.3-3 Triangularity dependence
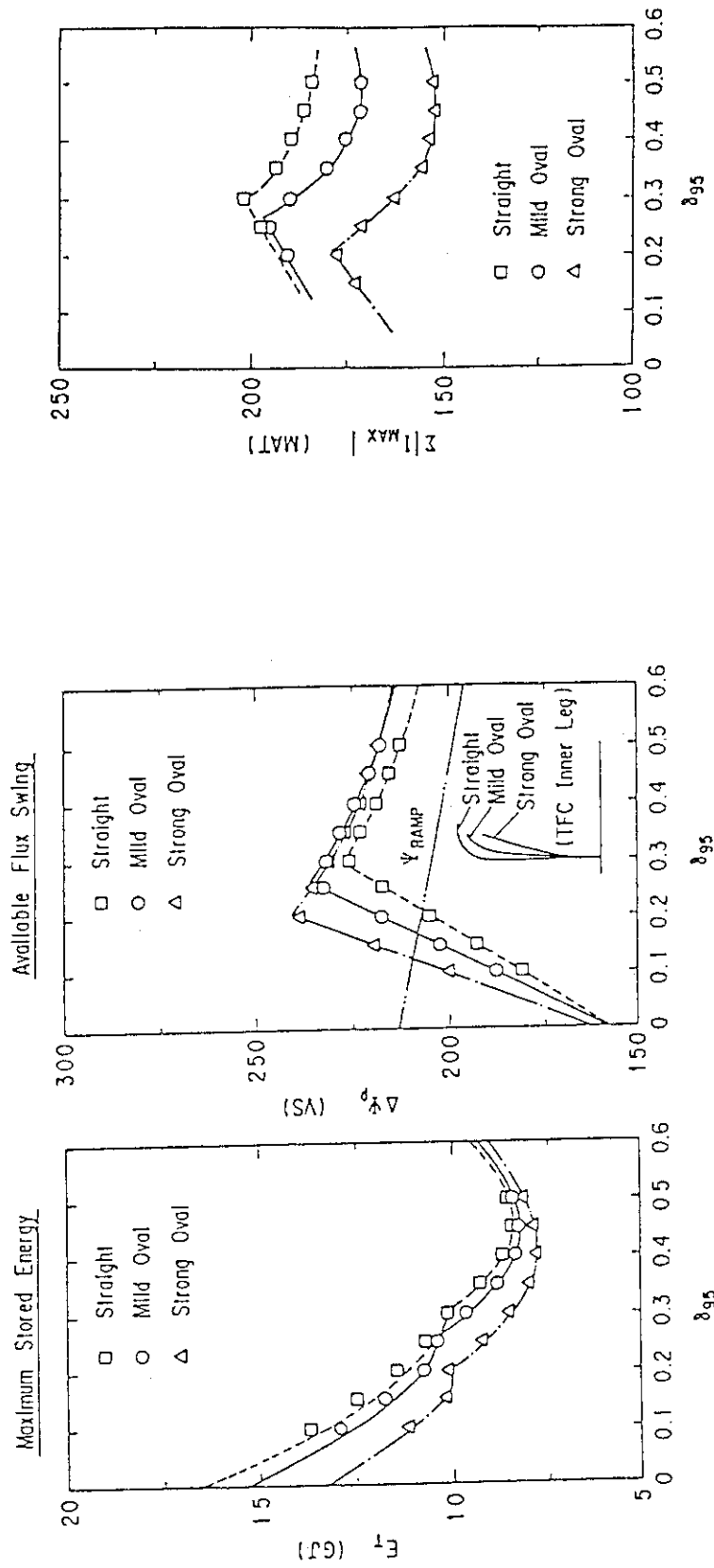of the total ampere-
turns.

Fig. 2.3-2 Triangularity dependence of the total stored
energy and available flux swing. The break
point corresponds to the transition point
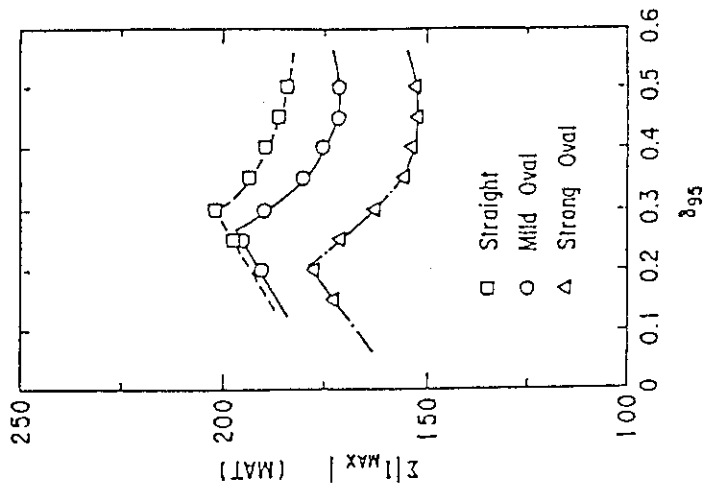from current density limited region to magnetic
field limited region of the solenoid coils.

Operation region for maximum field experience of 12T

Flux linkage (Vs)
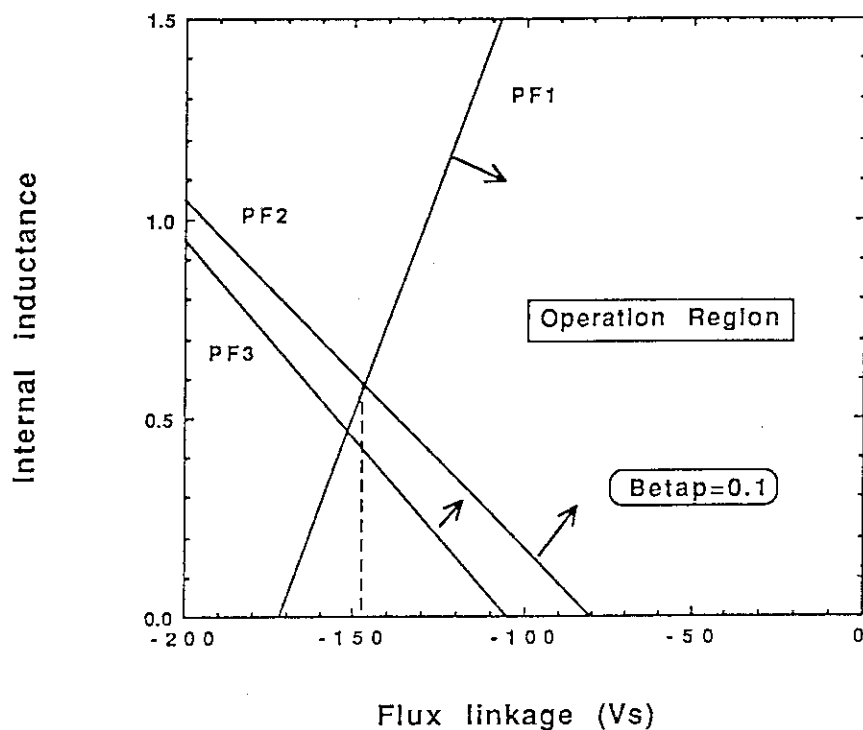
Operation region for maximum field experience of 12T
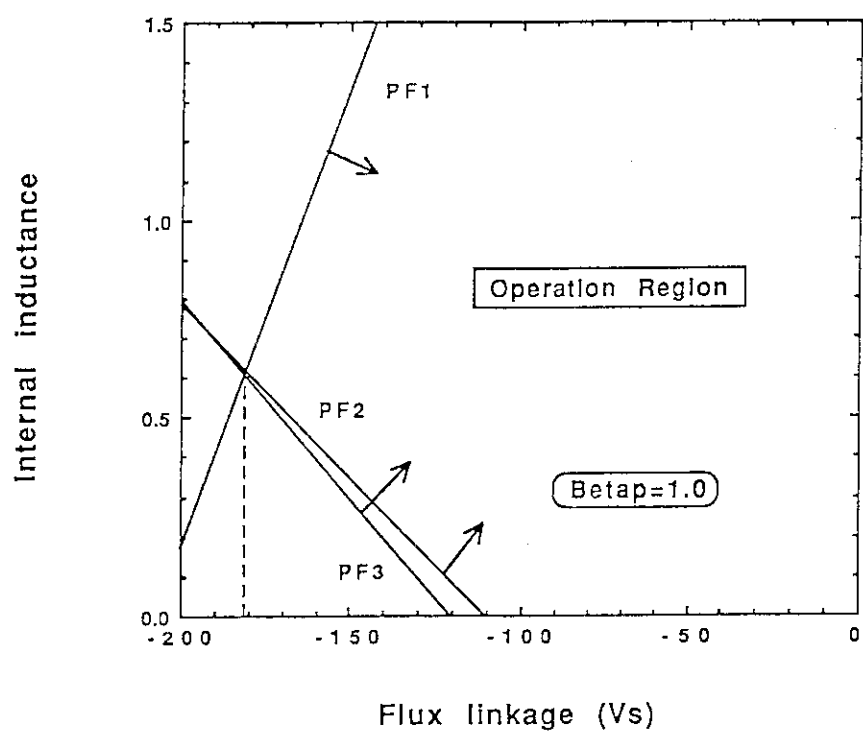
Flux linkage (Vs)

Fig. 2.4-1   Operation region spanned by internal inductance and flux
linkage.   Maximum field experience of the solenoid coils
are 12T and only three coils near the mid-plane are
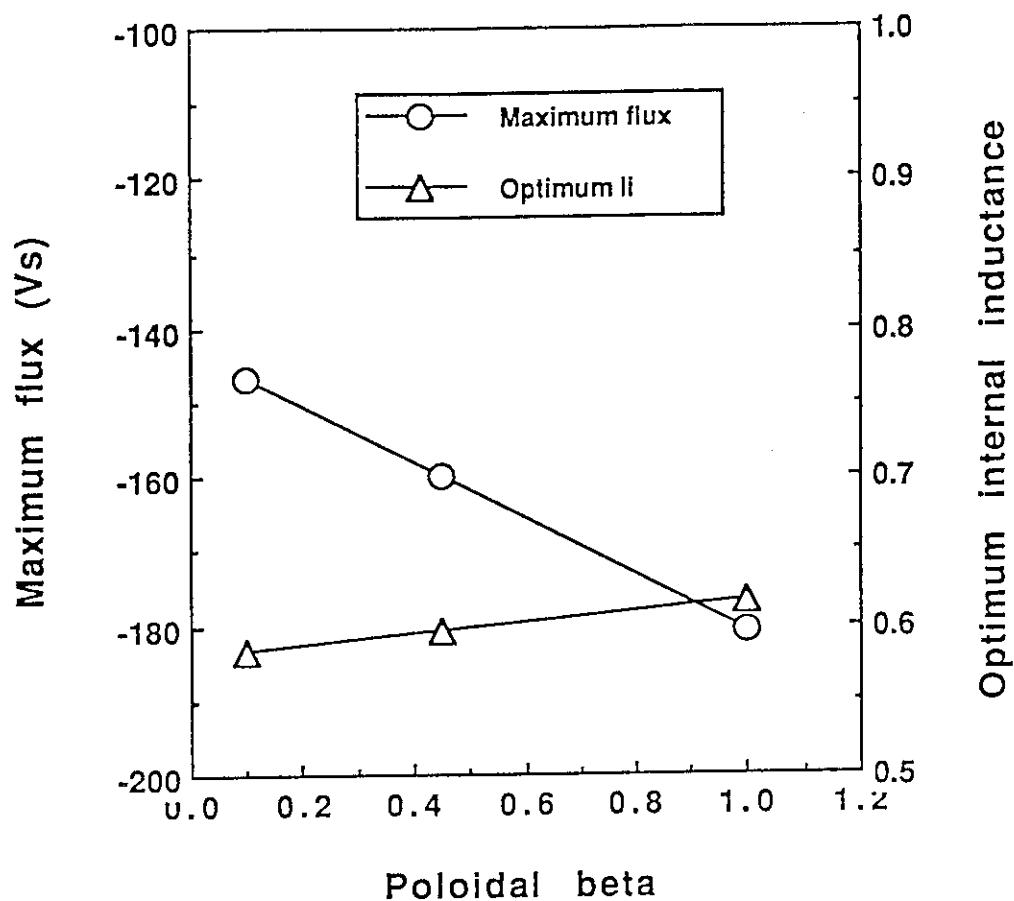evaluated as limiting coils.

Fig. 2.4-2 Maximum attainable flux linkage as a function of poloidal
beta. Optimum internal inductances at which flux linkage
attains maximum are also shown. High βp plasma can
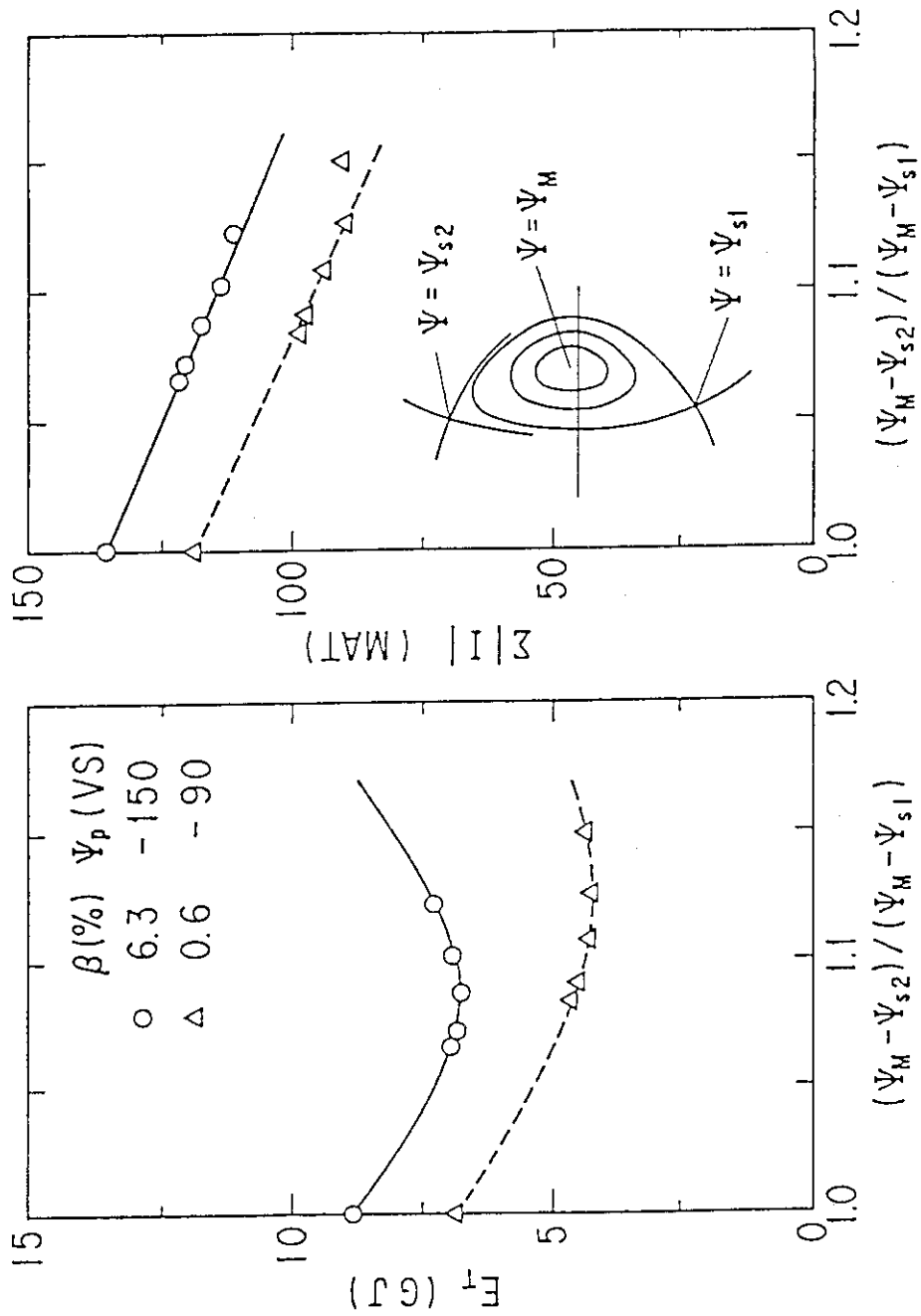utilize larger flux swing.

Fig. 2.5-1 Effect of the flux difference between active and passive nulls on the total stored energy and total ampere-turns. Single null plasma with appropriate up-down asymmetry has the minimum stored energy.

Single Null

Semi-Double Null

Double Null

$$\frac{\psi_M - \psi_{S2}}{\psi_M - \psi_{S1}} = 1.09$$

$$\frac{\psi_M - \psi_{S2}}{\psi_M - \psi_{S1}} = 1.02$$

$$\frac{\psi_M - \psi_{S2}}{\psi_M - \psi_{S1}} = 1.0$$

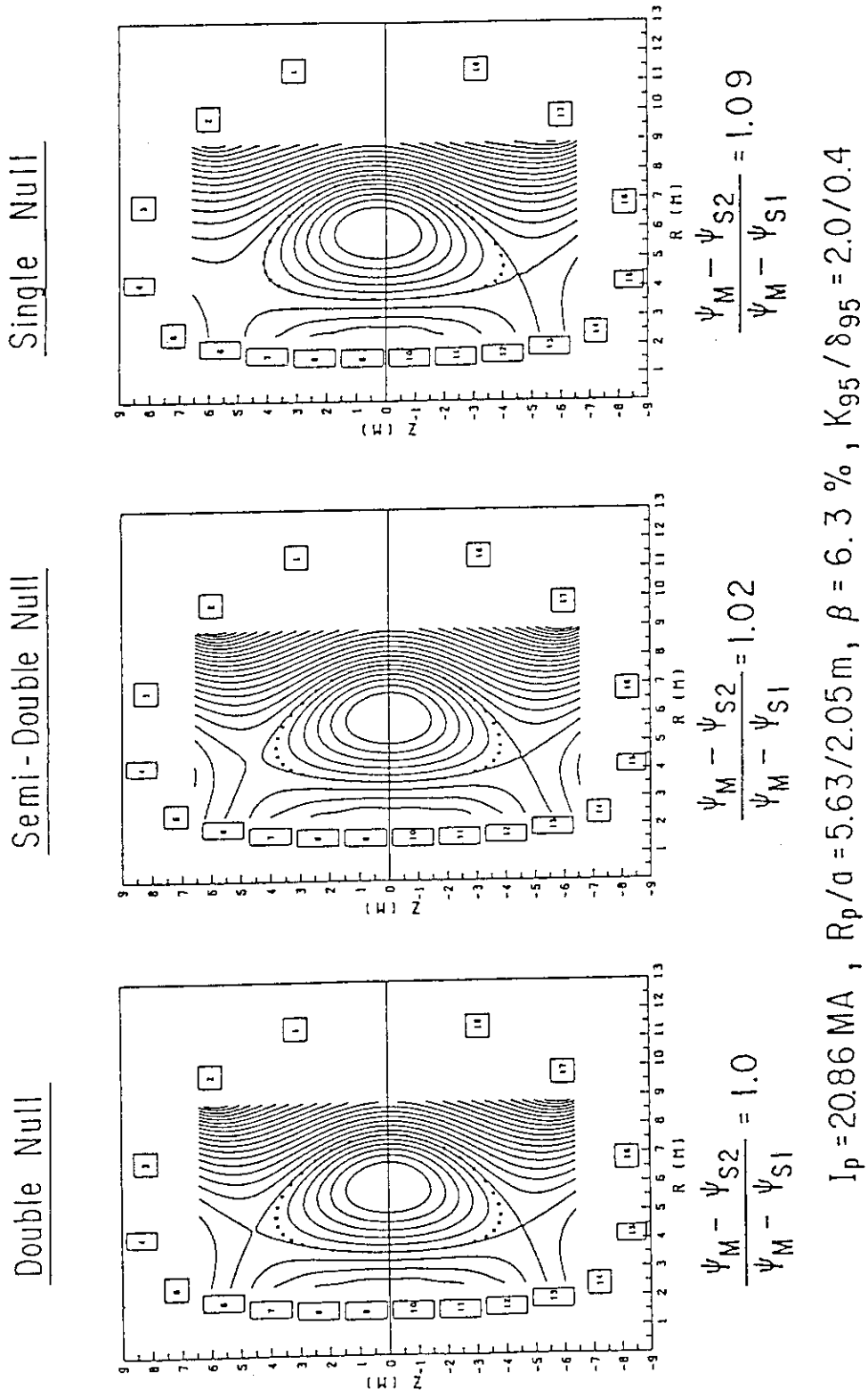$I_p = 20.86\,MA$, $R_p/a = 5.63/2.05\,m$, $\beta = 6.3\,\%$, $K_{95}/\delta_{95} = 2.0/0.4$

Fig. 2.5-2 Typical plasma equilibria with different degrees of up-down asymmetry.
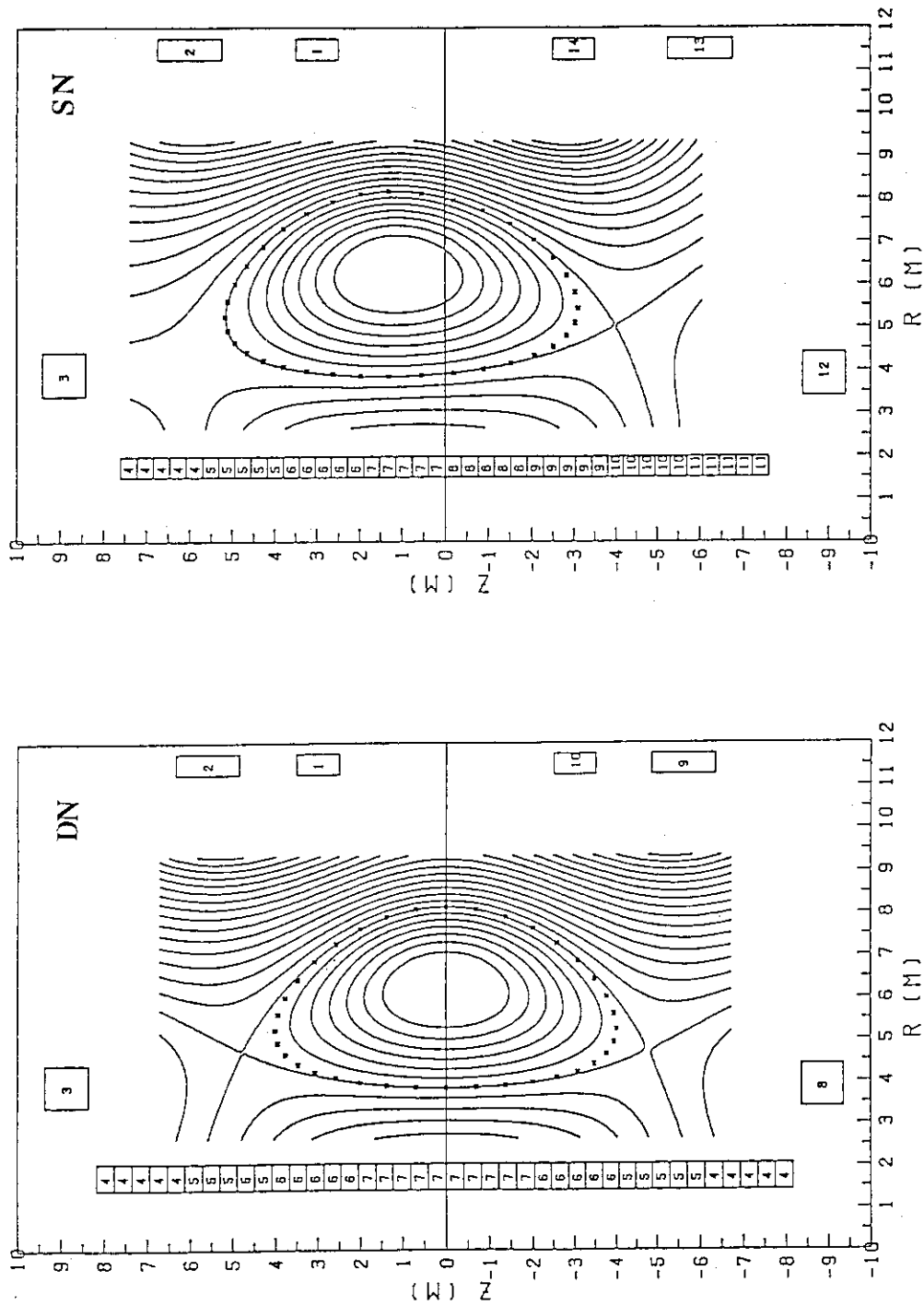
Fig. 2.5-3 Typical double null (DN) and single null (SN) plasma configuration with the same plasma current, major radius, minor radius, elongation, poloidal beta and internal inductance. Triangularity of the SN is smaller than that of DN. Vertical position of the SN plasma is shifted upward by about 1 m to fit containing structure.

Ampere-turns Profile Comparison between DN, SN1 and SN1b for Betap=0.6
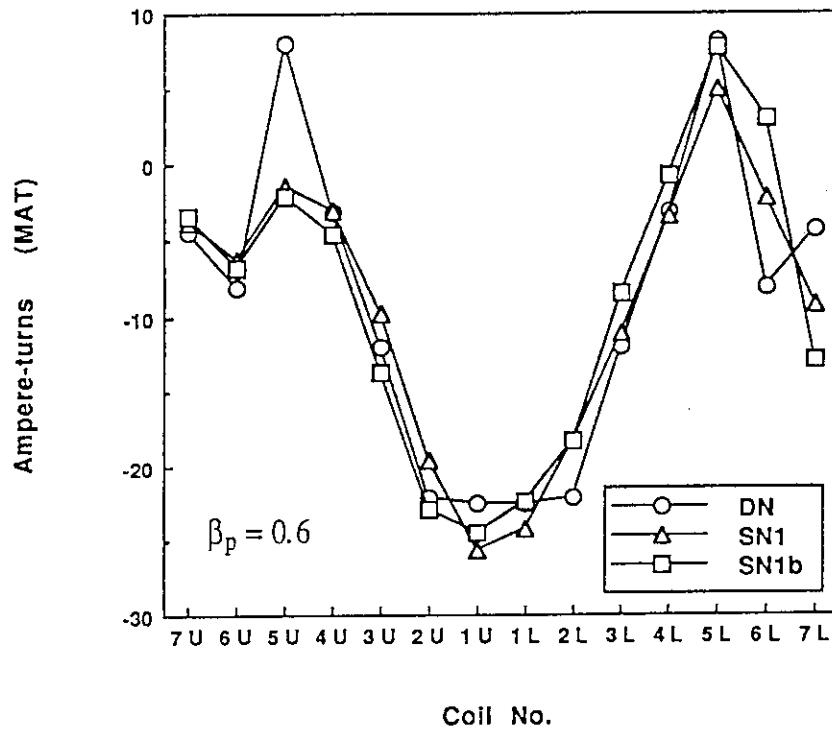
Ampere-turns Profile Comparison between DN, SN3 and SN3b
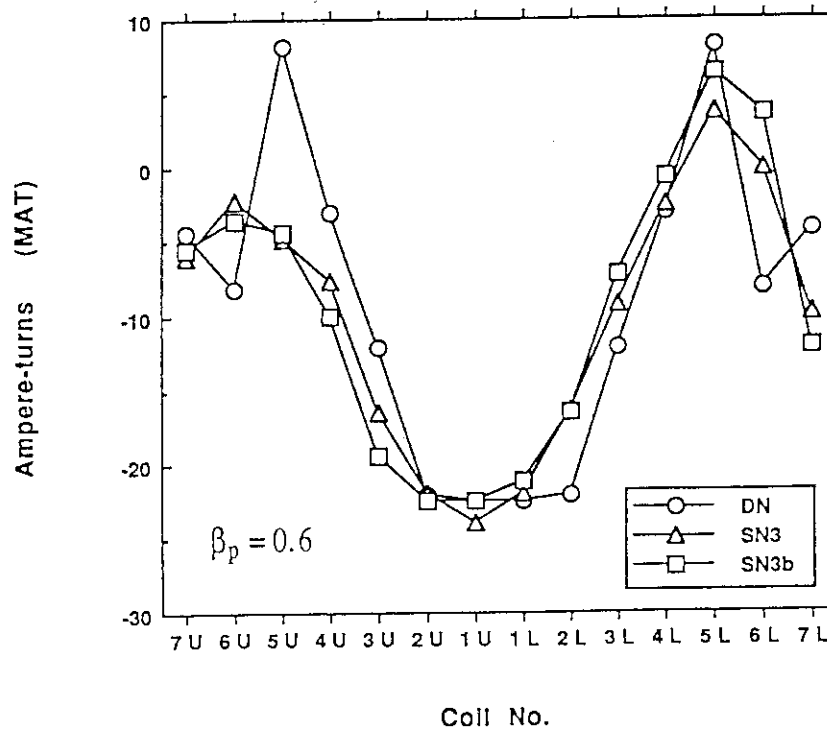

Fig. 2.5-4 Comparison of the ampere-turns profile between (a) DN, SN1 and SN1b and (b) DN, SN3 and SN3b. Reduction of the PF5U ampere-turns are clearly shown for the single unll plasmas.

Comparison of Energy and Ampere-turns between DN and SN Plasmas

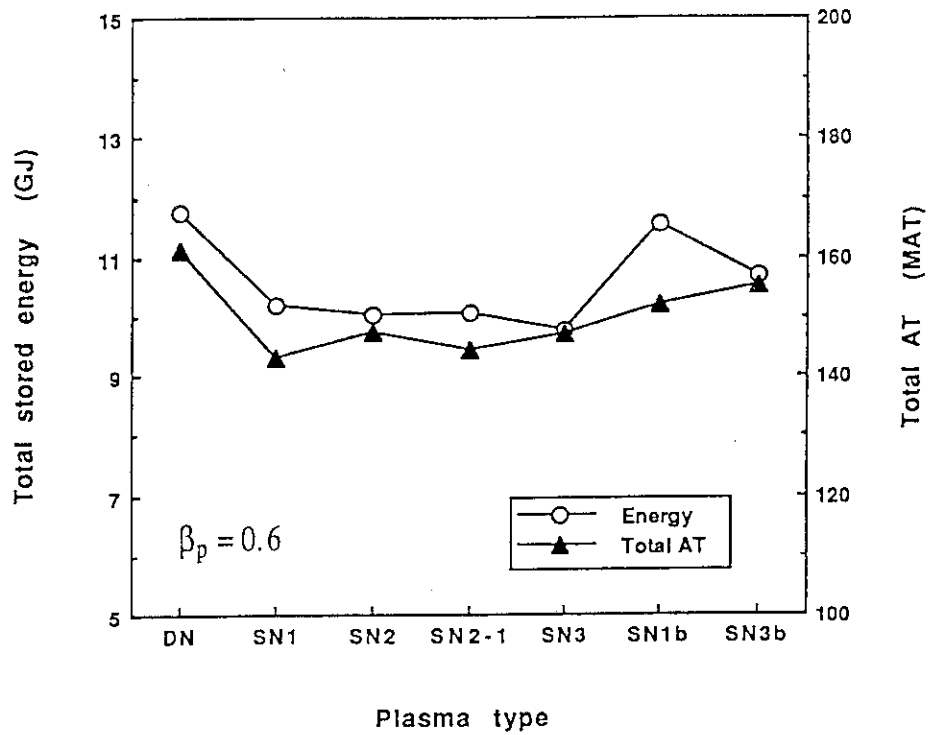Fig. 2.5-5 Comparison of Total stored energy and ampere-turns between DN and SN plasmas.

Comparison of Total Ampere-turn meter between DN and SN Plasmas
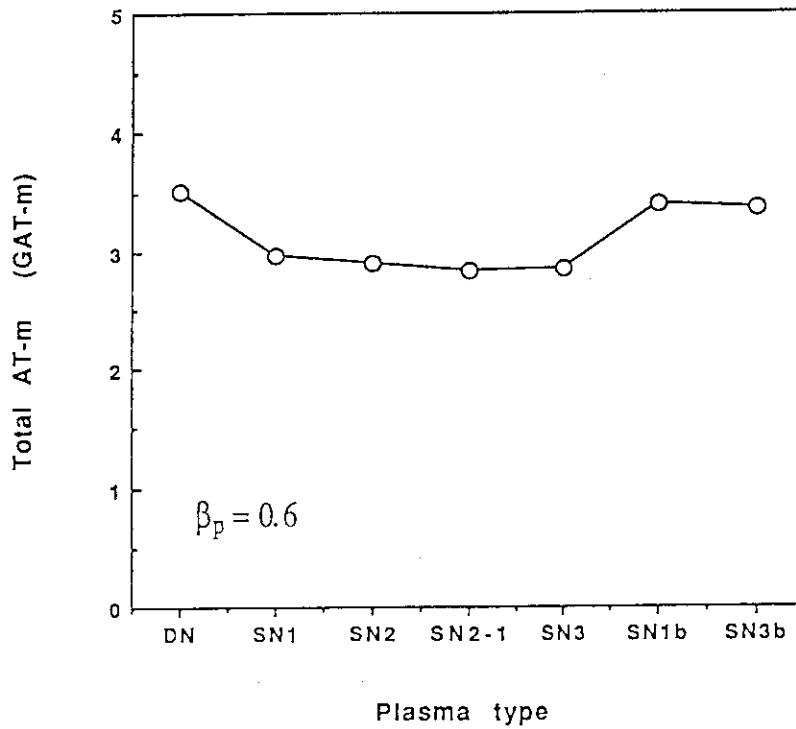
Fig. 2.5-6 Comparison of total ampere-turns meter between DN and SN plasmas.

Safety Factor vs Separatrix Separation

Fig. 2.5-7 Mapping of DN and SN plasmas in the space spanned by separatrix separation and safety factor at 95% flux surface.

Decay Index vs Skew
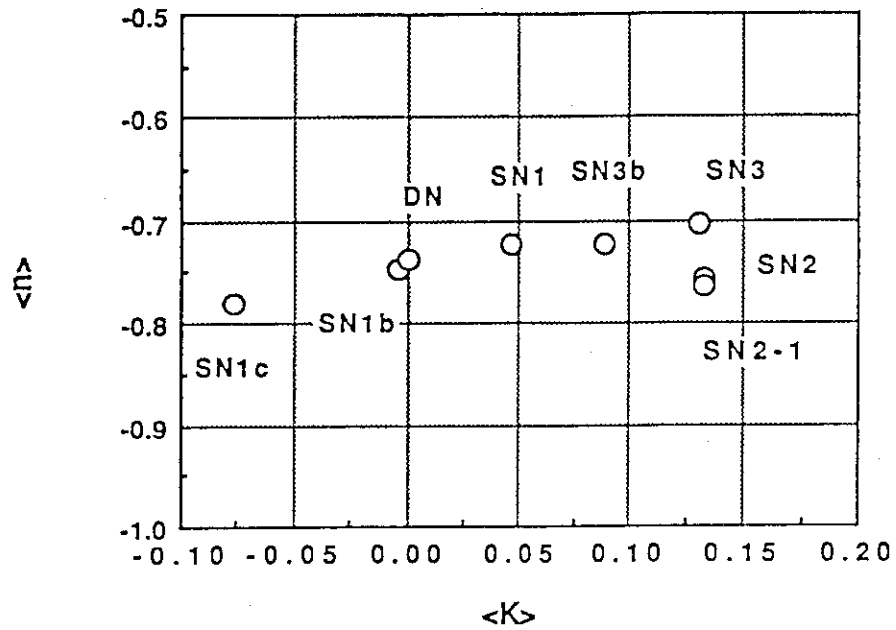
Decay Index vs Skew with Aspect Ratio Correction
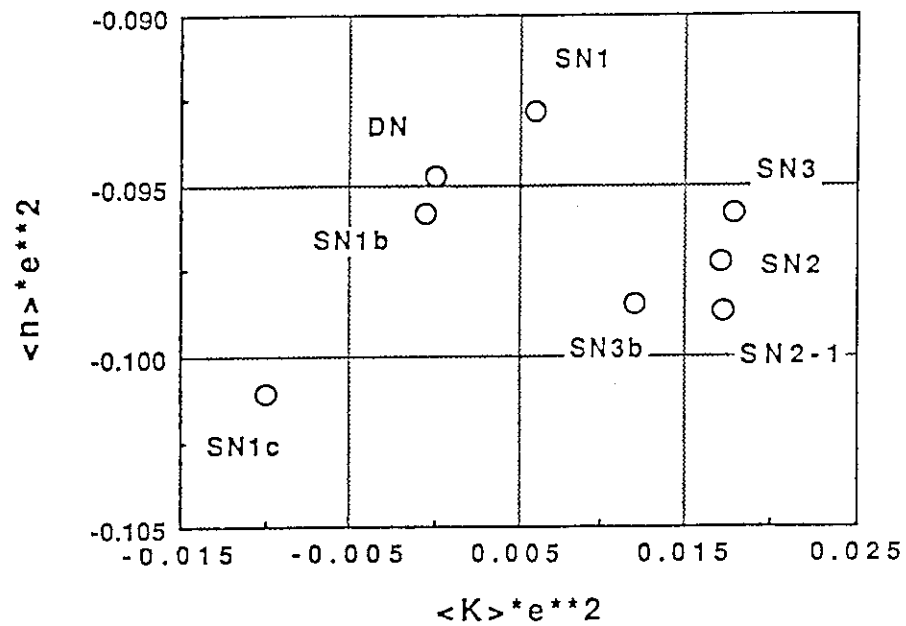
Fig. 2.5-8 Mapping of DN and SN plasmas in the space spanned by
decay index, <n>, and skew index, <K>. Both indices
are averaged by plasma current profile.

Fig. 2.6-2 Tracing of the magnetic lines of force near the separatrix for the DN plasma.

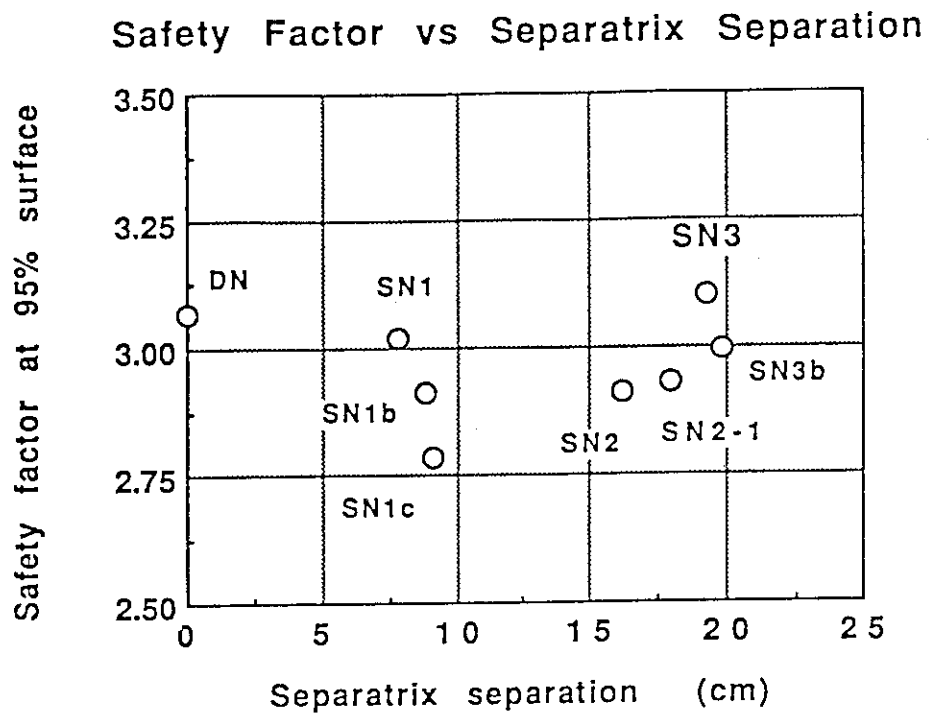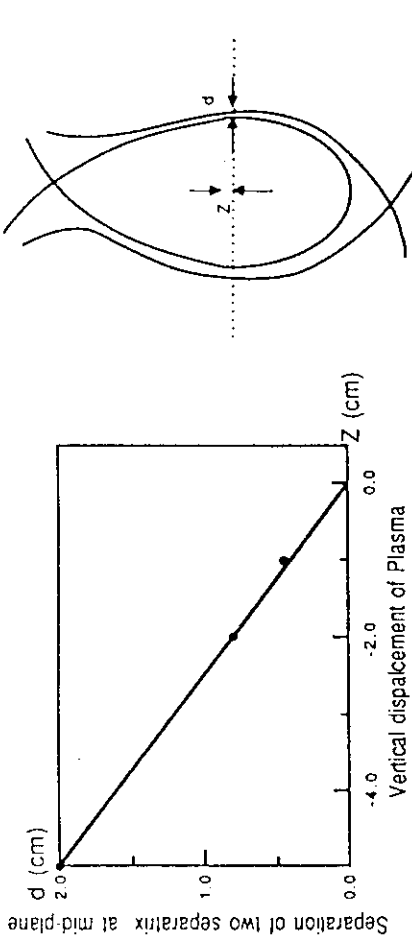Fig. 2.5-9 Separatrix separation vs vertical displacement obtained by the equilibrium code. Boundary flux value is kept constant as the plasma is shifted vertically.
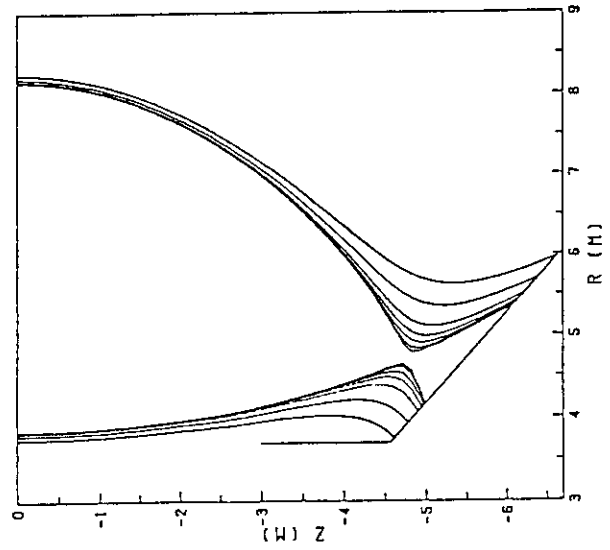
Fig. 2.6-1 Tracing of the magnetic lines of force near the separatrix for the DN plasma.
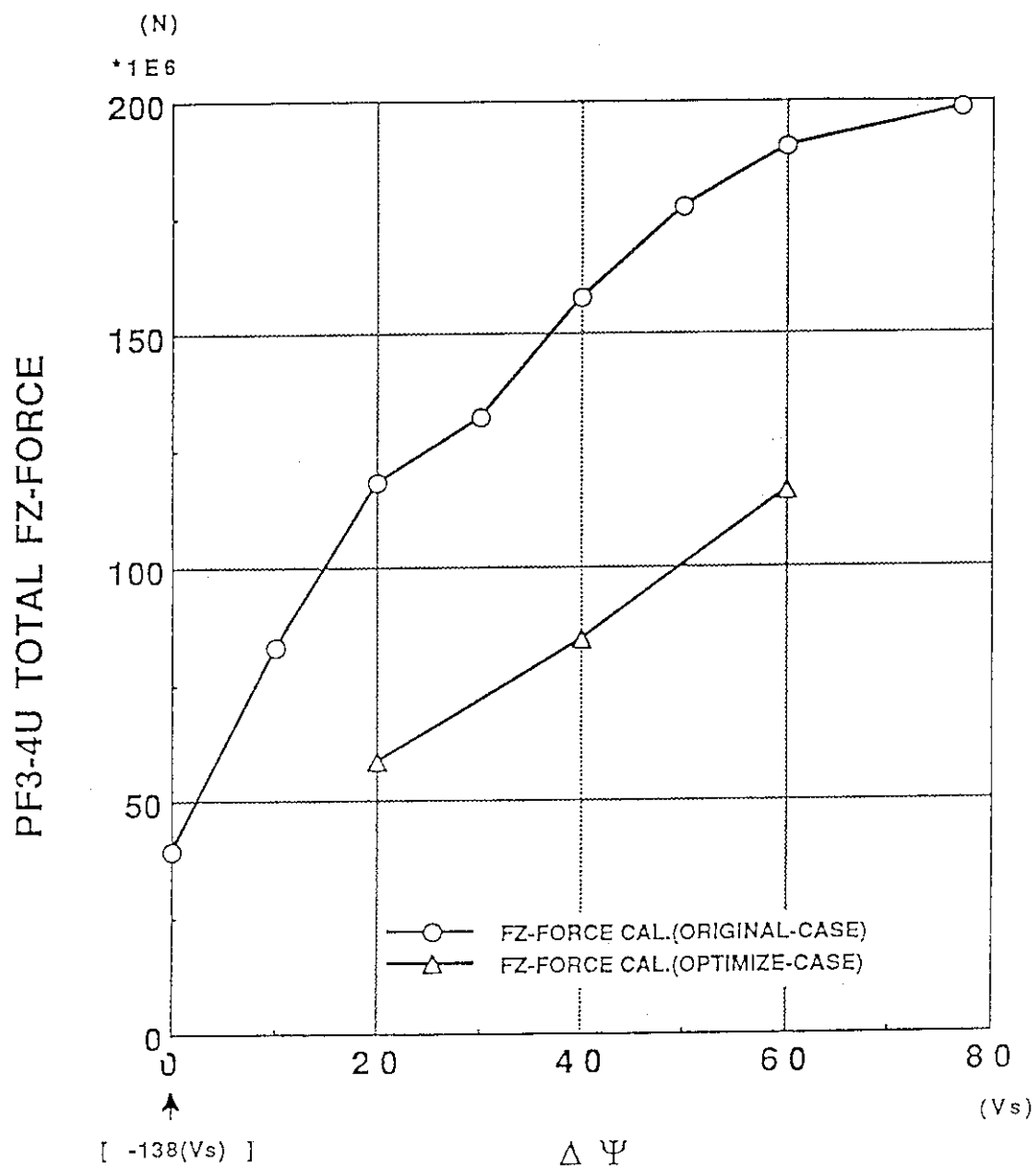
Fig. 2.7-1 Total repulsive force on the solenoid coil at SOFT
including the contribution from all of the PF coils.
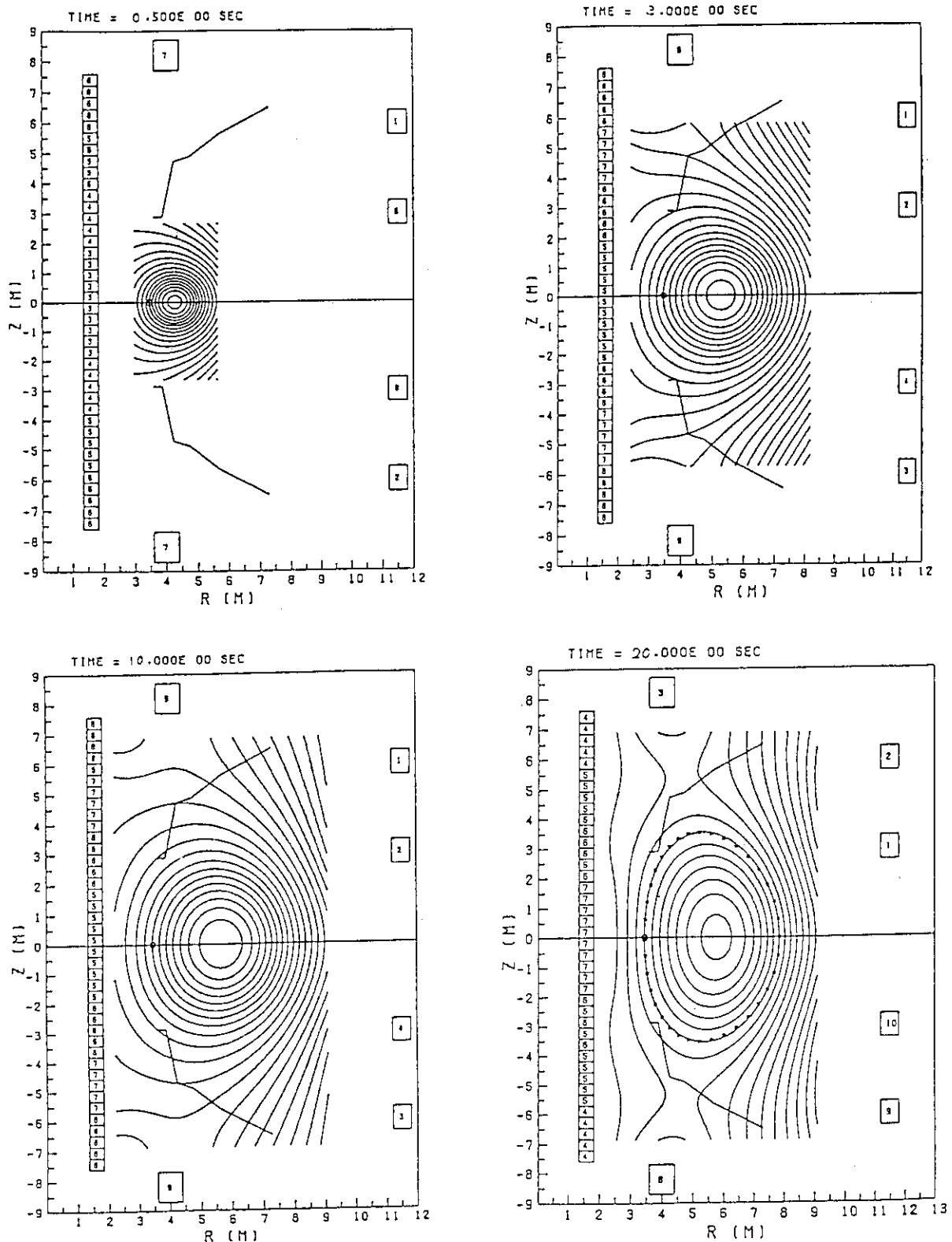
Fig. 2.8-1   Evolution of the plasma during startup. Minor radius of
             the plasma is gradually expanded along with the increase
             of the plasma current. Elongation and triangularity are
             also increased in order to avoid interaction with divertor
             plate and first wall during early stage of the startup.
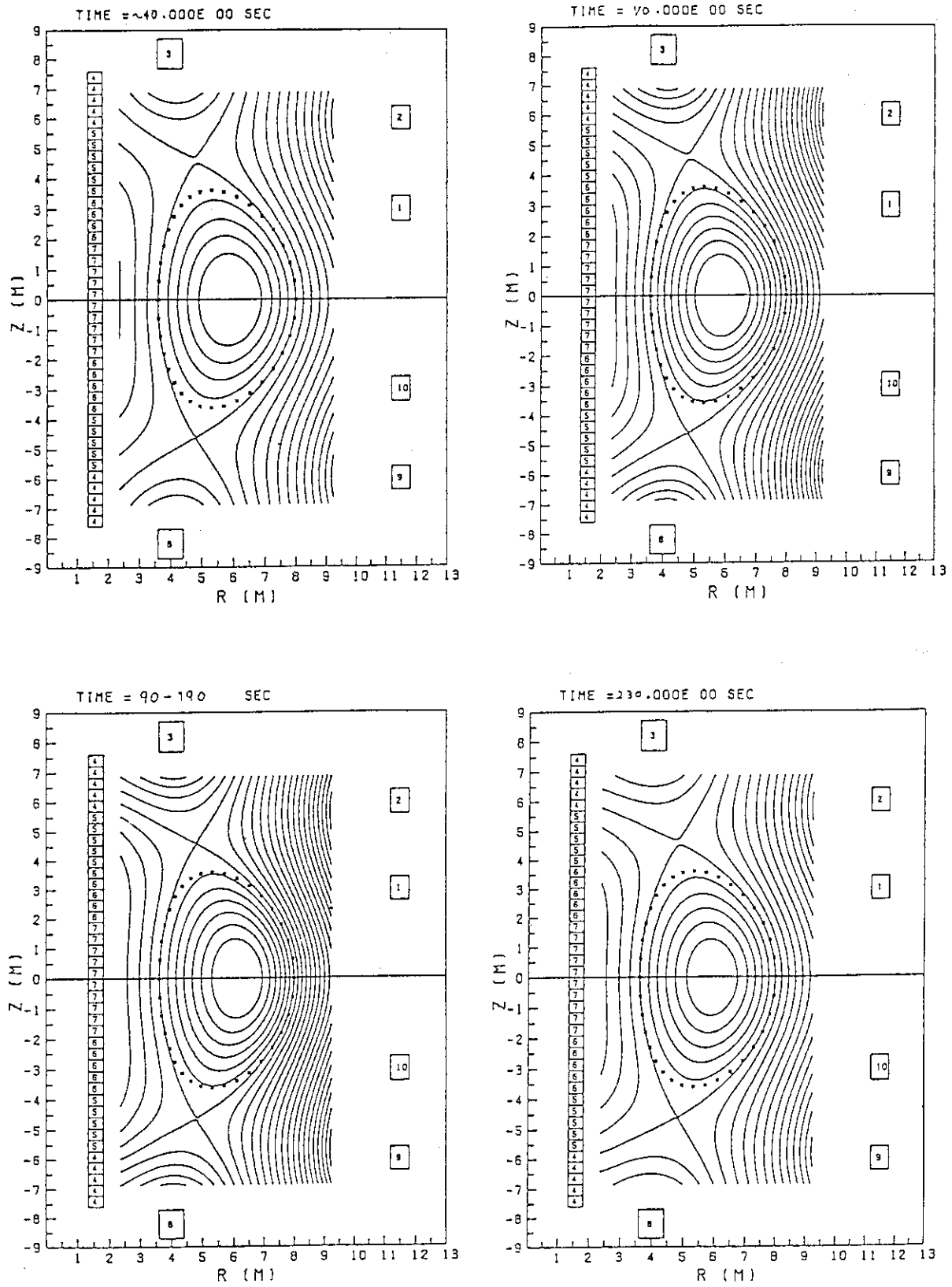
Fig. 2.8-1 (Continued)

3. Vertical position control

3.1 General criteria of plasma vertical stability

The active vertical position control of the highly elongated plasma was simulated to identify the general criteria of the plasma vertical stability considering the stabilizing and shielding effects of the passive shell structures based on the eddy current analysis. Calculating conditions are as follows.

(1) Initial perturbation

Plasma moves in the form of $\exp(\gamma t)$ based on the spontaneous growth model.

(2) Control

Control starts just after the detected value of the displacement exceeds 1 cm and tries to make the maximum displacement within 2.5 cm.

(3) Time lag of response

Two msec first order time-lag for detecting system and 2 msec dead time for power supply system.

From this simulation study, the relation between γ and the required installed capacity of the power supply was obtained as shown in Fig. 3.1-1. When the growth rate becomes 100/s, the required capacity of the power supply approaches to several tens MVA, and it increases drastically as the growth rate exceeds 100/s. Hence, the passive control system should fulfil the following requirements,

$$\gamma \leq 100 \text{ sec}^{-1} . \qquad (3.1.1)$$

The dashed curves in Fig. 3.1-1 represent the required capacity of the power supply in the case that the time lag of the detection was varied by ± 1 ms from the reference value of 2 msec. The effect of the time lag of the detection is small in the low γ region, though it becomes large in high γ region. However, the criterion for γ derived above will not be modified so much by the uncertainty of the expected time lag of the detecting and control system.

Another criterion derived at the specialist meeting in ITER (PF

System and Operation Scenario, May, 1988) [3], is the requirements for the stability margin m_S of the passive structures. The stability margin m_S is defined as

$$m_s = \frac{F_{stab.} - F_{destab.}}{F_{destab.}}$$ (3.1.2)

where :

$F_{destab.}$ is the destabilizing vertical force acting on the plasma due to the curvature of the external equilibrium magnetic field.

$F_{stab.}$ is the stabilizing vertical force acting on the plasma due to the flux-conserving eddy currents flowing in the passive structure (i.e., as if it were ideally conducting).

The stability margin can be rewritten as

$$m_s = \frac{n + N(\infty)}{n}$$ (3.1.3)

where n is the decay index of the equilibrium field and N(s) is N-function of passive structures (s;Laplace's s). Physical interpretation of the stability margin is the remoteness from the MHD unstable region (Alfven time scale instability), which represent the toughness of growth rate for the unknown perturbation or modification of plasma profile, position and so on. Fig. 3.1-2 shows the simplified example. For small stability margin, the increase of growth rate becomes fairly large with small variation of the N-function N(s). In this calculation, the initial growth rate γ_0 is same both for $m_S = 0.5$ and 1.0.

The criterion for m_S was determined as, $m_S \geq 0.5$. These requirements should be satisfied throughout the whole plasma operational and also in case of accidental inward radial movement of the plasma.

3.2 Study of the passive stabilizing effect of the saddle loop type stabilizing shell [4]

A parametric study of the passive stabilizing effect of the saddle loop type stabilizing shell and vacuum vessel is performed to determine the structural requirements for the passive stabilization. In this study, the dependences of growth time and stability margin on the detailed structure of the stabilizing shells (all of them are saddle loop type), gap width between the shells are presented and some structural requirements for the passive stabilization are examined.

Plasma parameters analyzed here are the plasma current I_p = 20MA, major radius R_p = 5.8m, minor radius a_p = 2.0m and elongation κ = 2.0. The equilibrium configuration is shown in Fig.3.2-1. The cases of high-ß (ß$_p$=1.0) and low-ß (ß$_p$=0.1) are studied. The decay index n and average vertical field B_V are -0.71 and 0.83T in the high-ß case and -0.90 and 0.61T in the low-ß case, respectively. To simulate horizontally displaced plasma due to sudden change of beta or current profile, the couplings between the plasma and passive structures are calculated by shifting horizontally the plasma current distribution.

The stabilizing shell and vacuum vessel are modeled by thin conductors with effective conductivity. The vacuum vessel is modeled by stainless steel (ρ=75$\mu\Omega$cm) of uniform thickness of 0.1 m. High resistant parts are inserted at 16 locations in the toroidal direction, and total one-turn resistance in the toroidal direction is 40 $\mu\Omega$ including the resistance 7.8 $\mu\Omega$ of thick sectors.

The location and shape of the stabilizing shell are shown in Fig. 3.2-1 (poloidal cross section) and Fig. 3.2-2 (toroidal cross section). The front face of the shell is along the flux line, which is 14.5 cm apart from plasma separatrix surface at the mid-plane. The width of front plate is 1.86m. The thickness of the side plate is 2 cm. The gap between shell sectors is defined by the distance between center lines of the plates. So, for the plate of 2 cm thickness, the gap of 2 cm means no space between surfaces of the plates.

The number of toroidal sectors of the stabilizing shell is 48. The following four types of structure for the stabilizing shell are studied.

(1) Type-A (Fig. 3.2-3(a))

The width of side plates is 0.5m. The shell sectors are isolated mutually and from the vacuum vessel.

(2) Type-B (Fig. 3.2-3(b))

The width of side plates is about 1.5m and the rear side of the shell is 10 cm apart from the vacuum vessel. The inductance and resistance of the current flowing vertically at the side plate are reduced and the stabilizing effect is expected to become higher than in Type-A.

(3) Type-C (Fig. 3.2-3(c))

Three shell sectors of the Type-B are electrically connected at the rear side. The eddy current can circulate in the three sectors and the flow pattern resembles the one in case of 16 sectors.

(4) Type-D (Fig. 3.2-3(d))

The rear side of the Type-C shell are connected to the vacuum vessel. The shell structures are conductible in the full toroidal direction through the high resistant part of the vacuum vessel. In this type, the one-turn resistance of the high resistant parts is set to be $40\mu\Omega$ only by themselves, because the one-turn current flows into the shell sectors and the resistance of the thick sectors of the vacuum vessel is expected to be neglected.

Figure 3.2-4 shows a typical mesh division of a structural model (Type-D) for the eddy current calculation.

The stabilizing effect of the passive structures are well characterized by N-functions. Figure 3.2-5 shows N-functions of vacuum vessel only, Types A, B and C. The material of the stabilizing shell is aluminium ($\rho=6\mu\Omega$cm), gap width is 4 cm and the thickness of the front plates are 2 cm in Type-A and 1 cm in Type-B and C. The effect of the thickness of the front plate is small because the path length of the plates is relatively shorter than that of the side plates. It is seen that the vacuum vessel has considerable stabilization effect, though it is not enough to stabilize the position only by the vacuum vessel. The stabilization effect becomes higher for Types A, B and C in order as expected.

Figure 3.2-6 shows N-functions of Type-C and D made of aluminium with 1 cm thickness of front plates and Type-D made of stainless steel with 2 cm thickness of front plates. The gap width is 8 cm. The effect of the electric connection between the shell structures

and vacuum vessel is small, especially at low s. The N-function of Type-D is a little lower than that of Type-C at low s resulted by higher resistance of the resistant parts. $N(\infty)$ and also stability margin of Type-D is a little higher than those of Type C. When aluminium is replaced by stainless steel, the N-function shifts to higher s and growth rate becomes higher. However, because the stabilization by the vacuum vessel is fairly high, the growth rate is not proportional to the resistivity of the shell. It is seen that $N(\infty)$ and stability margin does not depend on the conductivity of the shell.

Figure 3.2-7 and 3.2-8 show growth rates and stability margin, respectively, of the 4 types of structures in case of (a) high-ß, $\Delta R_p = 0$, (b) high-ß, $\Delta R_p = -20$ cm, (c) low-ß, $\Delta R_p = 0$ and (d) low-ß, $\Delta R_p = -20$ cm, where ΔR_p is the horizontal displacement of plasma. As it is expected, the high-ß plasma at the reference position is most stable and the low-ß at the displaced position ($\Delta R_p = -20$ cm) is least stable. The growth rate is smaller than 100/sec except the case of the stainless steel shell. In the least stable case, the stability margin of Type-A is less than 0.5 and the gap width is necessary to be less than about 3 cm in Type-B and about 6 cm in Type-C for the stability margin to be higher than 0.5.

From this study, followings are concluded for the design of the saddle-loop type stabilizing shell in ITER.

(1) The growth time of the blanket made of stainless steel without aluminium or copper shells is lower than 10 msec . Aluminium shell of 2 cm thickness is enough to increase the growth time higher than 10 msec.

(2) The width of side plates of shell is important, and width of 0.5m is not enough.

(3) The gap width must be as small as possible. The gap width must be less than about 3 cm (the space between plate surfaces about 1 cm) when 48 sectors are separated, and about 6 cm (about 4 cm) when 3 sectors are electrically connected at the rear side, to attain the requirement of stability margin higher than 0.5.

(4) The merit of the connection between the shell sectors and vacuum vessel is small.

3.3 Study of passive stabilizing effect of the twin loop type stabilizing shell

Effects of a variety of plasma conditions as well as the twin loop geometries on the stabilizing characteristics (growth rate and stability margin) of twin loop stabilizer in ITER are examined . Major effects examined are 1) effect of gaps between blankets, 2) effect of gaps between blanket end wall and vacuum vessel, 3) effect of vertical height of horizontal port, 4) effect of plasma beta and current profile. Figure 3.3-1 shows the location and dimension of the twin loops and the vacuum vessel in the poloidal cross section of the torus. Two values of vertical half height D of the horizontal port are examined, since they may be decreased down to 1700 mm from the reference value of 2700 mm due to the installation of ICRF antenna. Figure 3.3-2 shows the details of the material and thickness of the center and side blanket modules. Figure 3.3-3 shows the details of the material and thickness of the various region of the vacuum vessel. Electrical resistivity for stainless steel and copper are assumed 8.2×10^{-7} Ωm and 1.72×10^{-8} Ωm, respectively. Vacuum vessel consists of thick part with thickness of 200 mm and the bellows region with thickness of 50 mm and width of 10 cm, resistivity of which is assumed 1.8×10^{-6} Ωm. Figure 3.3-4 shows the details of mesh for the eddy current calculation by finite element method. In the present study, the following cases and parameter ranges are examined;

-effect of gap between blanket modules d_1; 10 and 30 mm
-effect of gap between vacuum vessel
  and blanket end wall d_2; 10 - 50 mm
-effect of vertical half height of horizontal
  port D, 1.7 and 2.7 m
-effect of space between plasma surface
  and passive shell (twin loops) d_3; 15 and 25 cm
-effect of plasma condition
  beta poloidal β_p; 0.01 - 0.6
  internal inductivity l_i; 0.65 - 0.9

Several of the possible combinations of the above parameters are examined, and these cases are summarized in Table 3.3-I. In the

table, stability margin and growth rate are summarized in upper and lower column, respectively for the examined cases. In the following figures, the frequency response of the shell effect for the shell condition of ST1 (Fig. 3.3-5), ST4 (Fig. 3.3-6) with various plasma conditions. In Figs 3.3-7 - 3.3-10 are summarized the change of stability margin as the gap width is changed for various plasma and other shell geometries conditions.

3.4 Study of active control of vertical plasma position

In this section, at first, the positioning of the active control coil system is investigated to examine the field penetration. There are two factors, which determine the field penetration; one is the efficiency to produce the required field with given coil current and the other is the shielding effect of the shell, blanket and vacuum vessel. Comparison of three different coil positioning cases; just behind the first wall, between blanket and vacuum vessel, and outside vacuum vessel is carried out concerning both the horizontal (for vertical position control) and vertical (for horizontal position control) fields penetration. The results are shown in Fig. 3.4-1, where horizontal and vertical magnetic field at plasma center are plotted as a function of time when 100 kA is imposed stepwise for three different positioning cases. The shell type used in the calculation is twin loop type. Although the positioning of just behind the first wall has best penetration characteristics as shown in the figure, it will not be acceptable from view point of maintenability.

The characteristics of the active feedback control are investigated with consideration of the induced eddy current effect on the shell, vacuum vessel and the blanket structure as well as the field penetration properties of the active control coil. The equation of the plasma motion is given as follow.

$$M_p \frac{\partial^2 Z_p}{\partial t^2} = -2R_p I_p \left(\frac{n B_{Z0}}{R_p} Z_p + v_c I_c + \sum_i v_i I_i + B_d \right) \qquad (3.4\text{-}1)$$

Here, M_p and R_p are the plasma mass and the major radius of the plasma column, respectively. I_c, I_i and B_d are the active control coil

current, the eddy current of the i-th eigen mode and the disturbance radial field (here 10 Gauss is assumed), respectively. v_c and v_i are the radial fields produced by the unit current of the active control coil and by the i-th eddy current mode, respectively. The required voltage for the control coil was calculated in accordance with PID control system. The dependences of the required voltages on the gain G are shown in Fig. 3.4-2. Control coil position is behind the blanket and the detected plasma displacement is 1 cm. As the gain increases, the voltage increases while the coil current is almost unchanged. Figure 3.4-3 shows the dependences on the control coil position for the gain value of 3×10^4 V/m and the detected plasma displacement of 1 cm. As expected, the required coil current is smallest in the coil position of the first wall due to the best efficiency of producing horizontal field and the least shielding effect of vacuum vessel and shell. Figure 3.4-4 shows the dependences on the detected point of the plasma displacement for the gain value of 3×10^4 V/m and the coil position of behind the blanket. Figure 3.4-5 shows the dependence on the plasma conditions, i.e., the reference plasma with $R_p=6m$, $\beta_p=0.6$ and $l_i=0.65$ and the degraded plasma with $R_p=5.9m$, $\beta_p=0.01$ and $l_i=0.9$, for the gain value of 3×10^4 V/m, the coil position of behind the blanket and the detected point of the plasma displacement of 1 cm. Note that, though the growth rate is much larger in the degraded case than that in the reference case, while the absolute value of the destabilizing force is rather smaller due to the reduction of vertical field. Consequently, the required current to control the plasma position is rather smaller in the degraded case. However, when the time delay of the detecting and control systems are actually considered, required voltage and current should be larger in the degraded case.

Table 3.3-I Cases of shell type and plasma conditions for the evaluation of stability margin and growth rate. Upper and lower figures represent the stability margin and growth rate, respectively.

d1 : Gap between blanket modules	10 mm			30 mm		
d2 : Gap between vacuum vessel and blanket end wall	10 mm		50 mm	30 mm		50 mm
D : Vertacal width of horizontal port	1.7 m (ST1)	2.7 m (ST2)	1.7m (ST3)	1.7 m (ST4)	2.7 m (ST5)	1.7 m (ST6)
d3=15cm β_P=0.6 l_i=0.65 (PL1)	1.31 / 15.2	1.01 / 20	1.21 / 16	1.19 / 16.8	0.88 / 26.5	1.15 / 17.3
R_P=6.0m β_P=0.1 l_i=0.75 (PL2)	0.85 / 24	♪	♪	0.77 / 26.8	♪	♪
β_P=0.01 l_i=0.9 (PL3)	0.66 / 32.8	0.54 / 44.3	0.59 / 35	0.57 / 38.8	0.44 / 62	0.55 / 40.8
d3=25cm β_P=0.6 l_i=0.65 (PL4)	1.23 / 16	♪	♪	1.13 / 17.5	♪	♪
R_P=5.9m β_P=0.01 l_i=0.9 (PL5)	0.59 / 36.2	♪	♪	0.53 / 43	♪	♪

1.23	→ Stability margin
78.9	→ Growth rate (1/sec)

Fig. 3.1-2 Increase of growth rate γ from the original value γ0 as a function of the fractional variation of N(s) for different value of stability margin ms=0.5 and 1.0.

Fig. 3.1-1 Relation between γ and required installed capacity of the power supply.
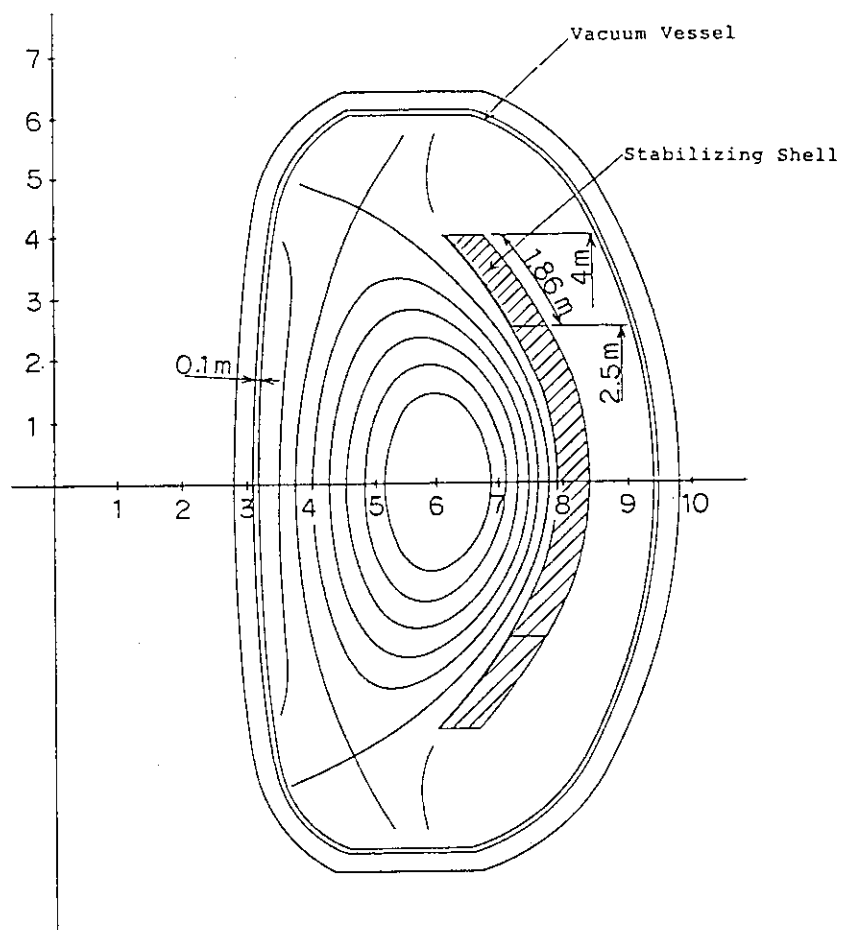
Fig. 3.2-1 Poloidal cross section of plasma, stabilizing shell and
vacuum vessel.
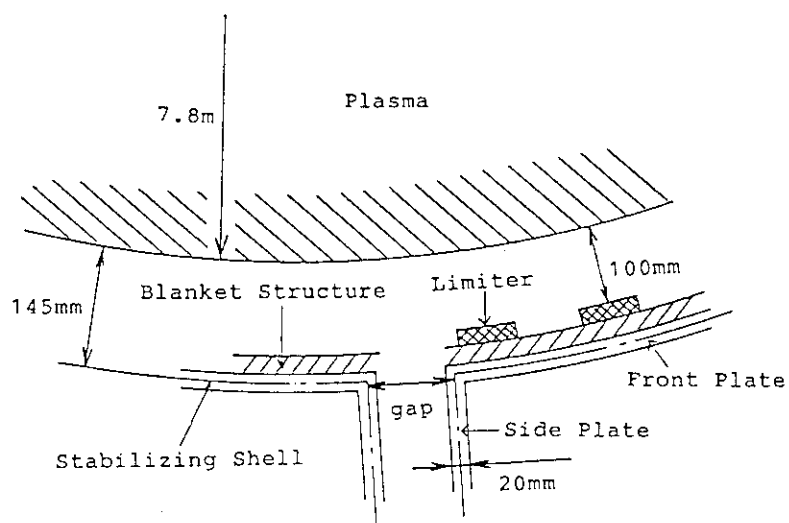
Fig. 3.2-2 Toroidal cross section at the mid-plane.

(a) Type-A

(b) Type-B

(c) Type-C
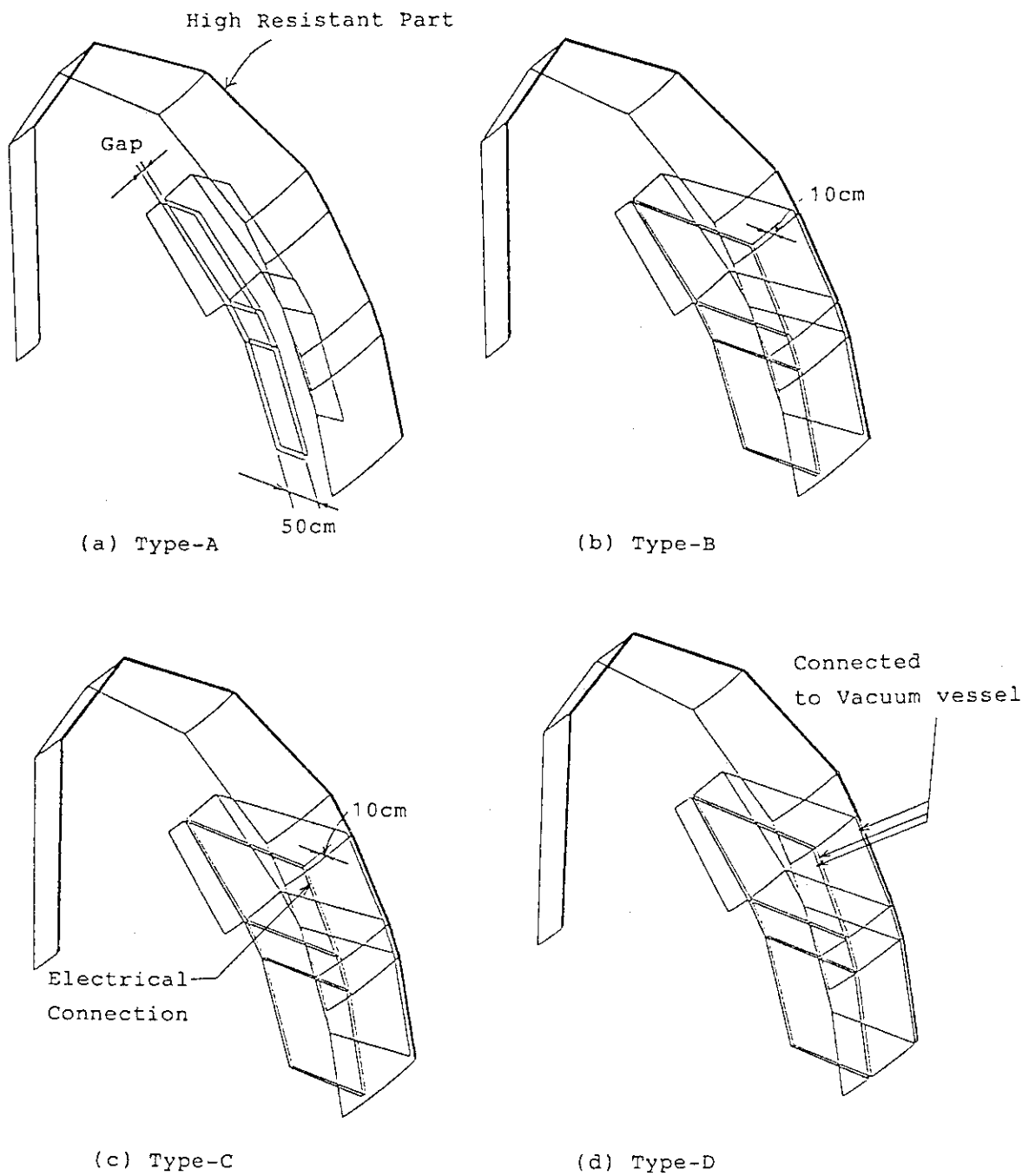
(d) Type-D

Fig. 3.2-3 Types of stabilizing shells.
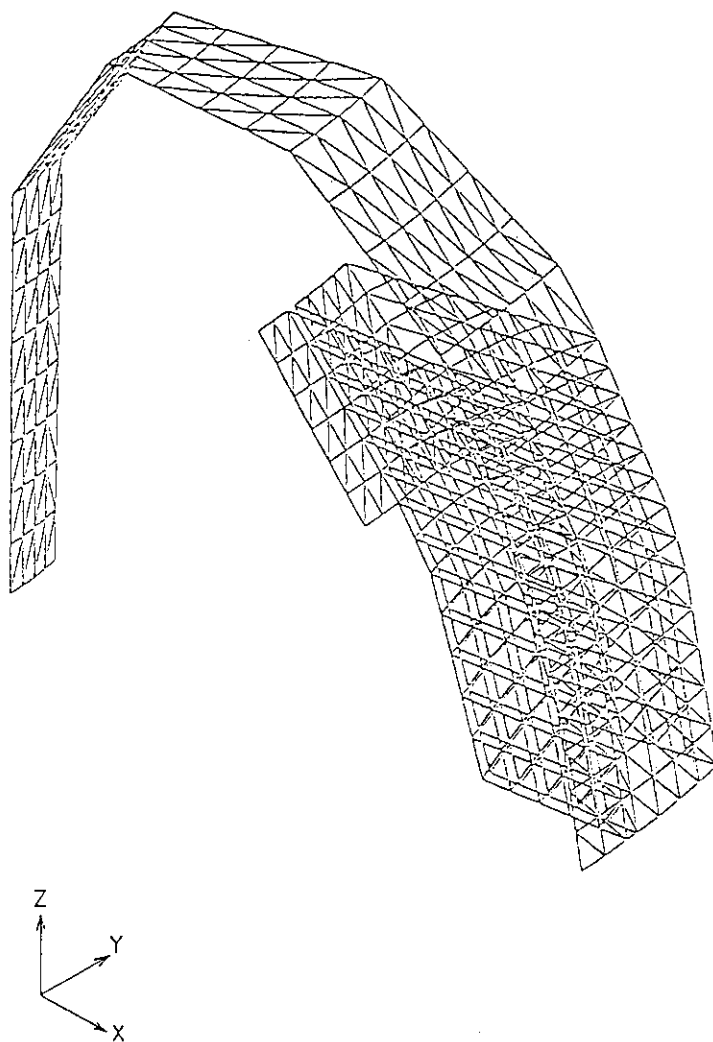
Fig. 3.2-4 Mesh division of model (Type D).
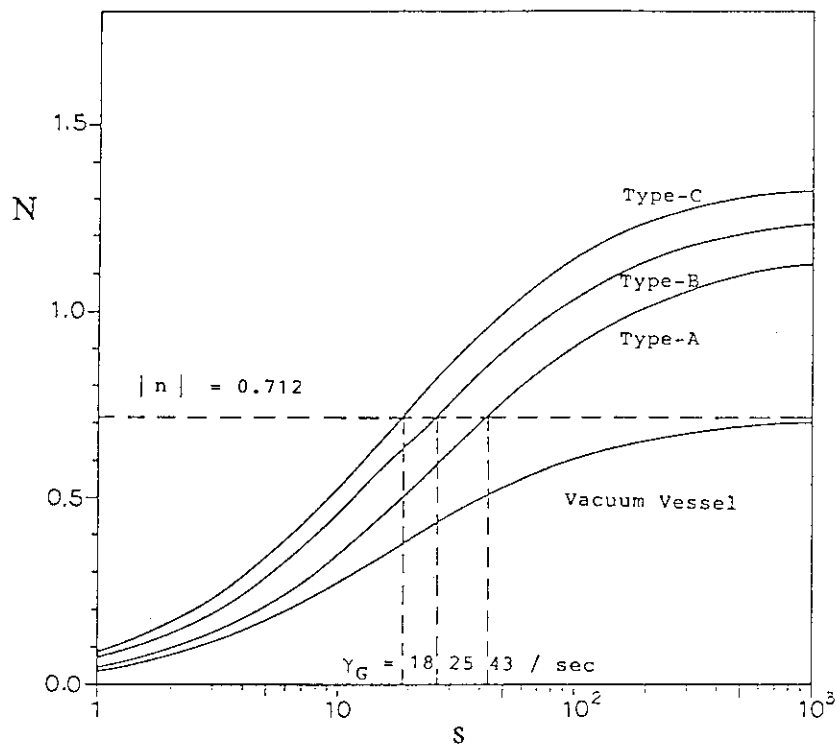
Fig. 3.2-5 N-functions of vacuum vessel, Type A, B and C in case of high-β (ΔRp=0.0). Thickness of front plate is 2 cm, 1 cm and 1 cm in Type A, B and C, respectively. Gap width is 4 cm.
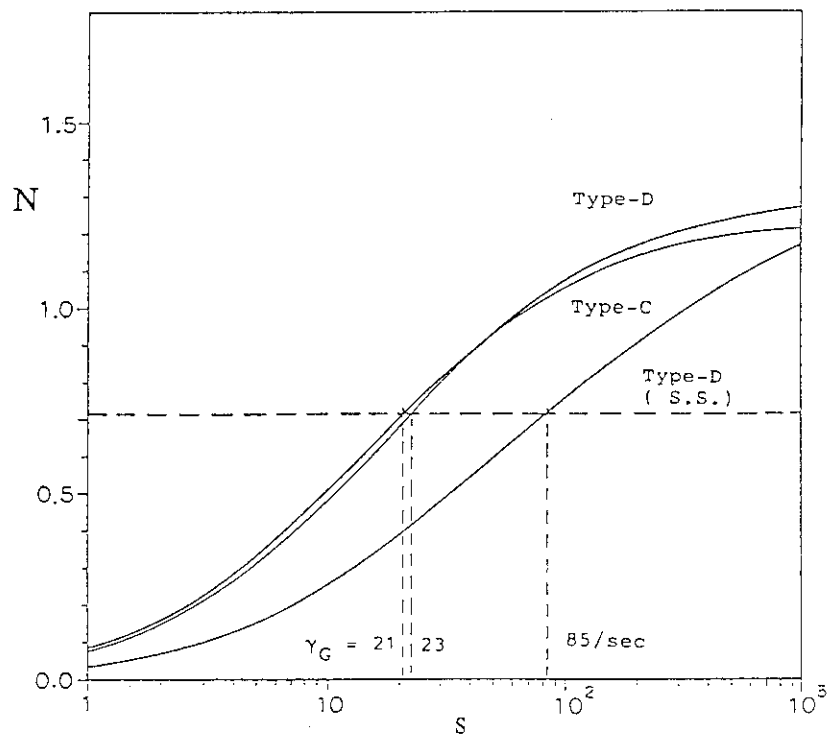
Fig. 3.2-6 N-functions of Types C and D in the case of high-β (ΔRp=0.0). Gap width is 8 cm.
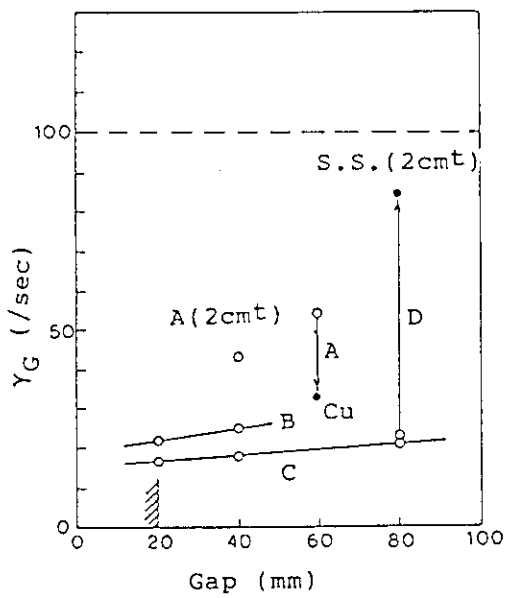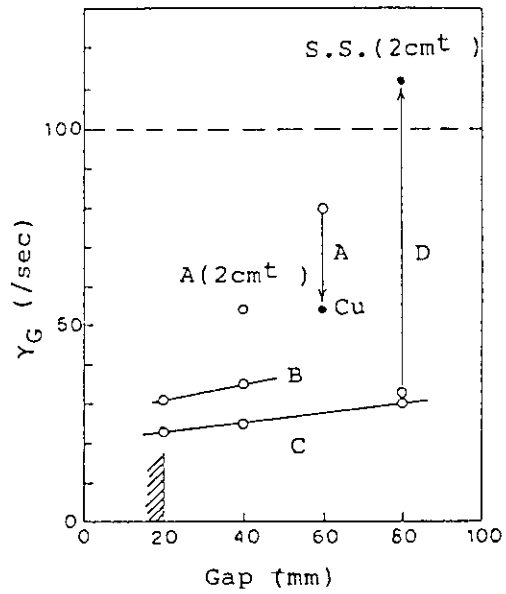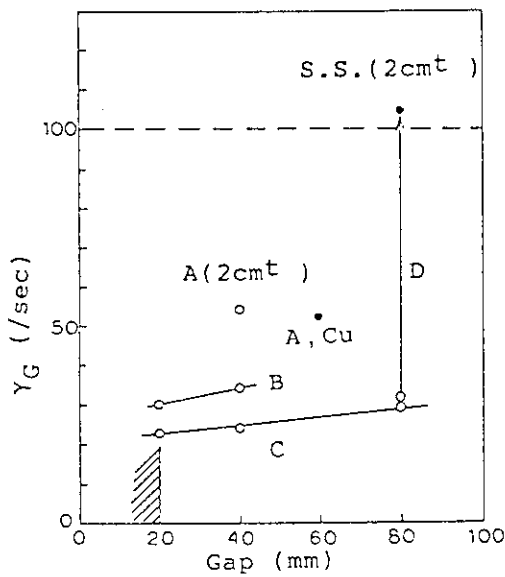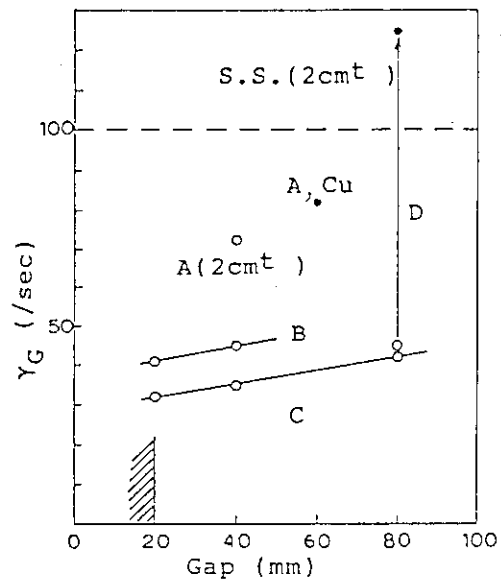
Fig. 3.2-7   Growth rates as a function of gap size.   The open circle
shows aluminium shells and the closed circle shows other
types of shell.   Thickness shown in that of one of the
front plates.   Thickness not shown is 1 cm.
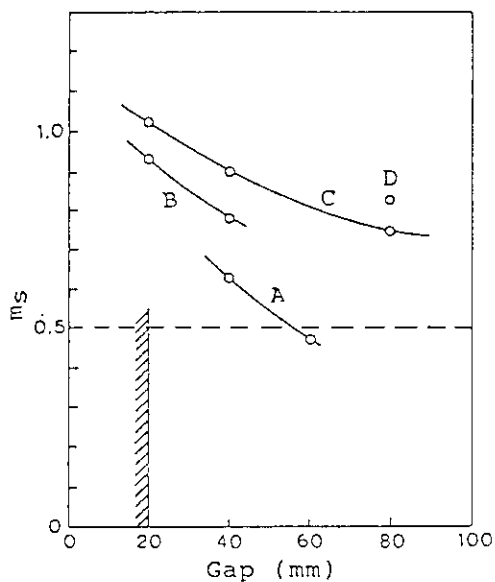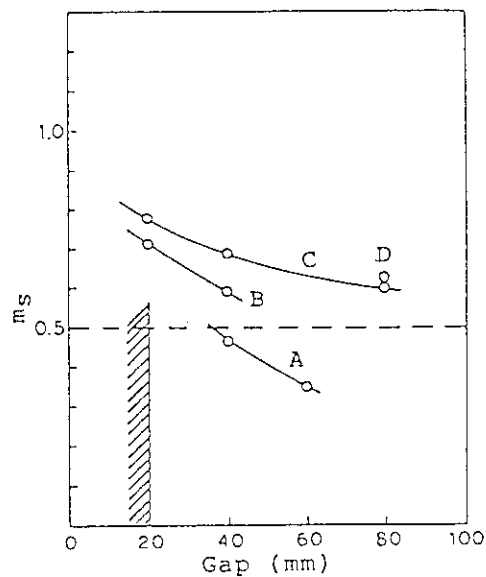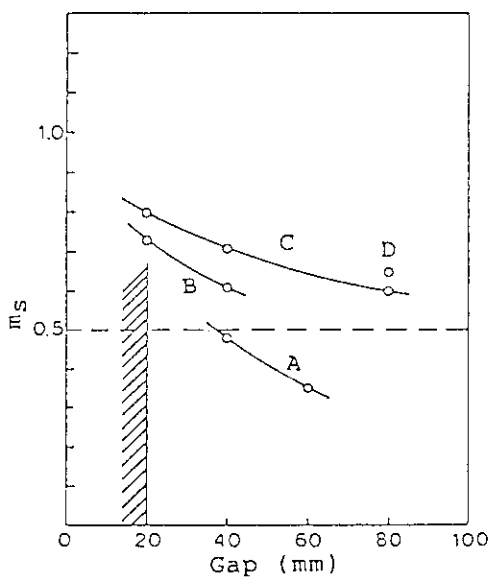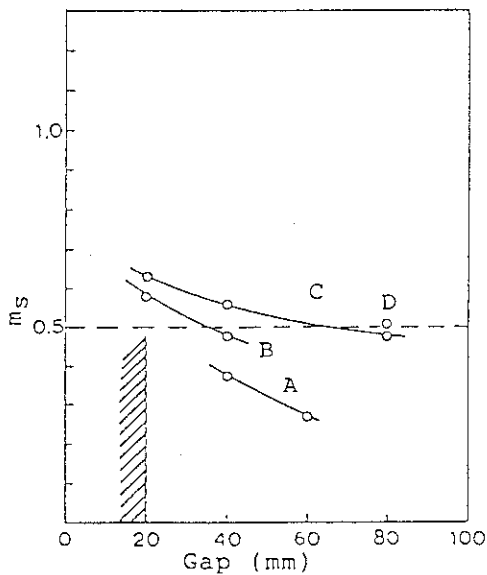
Fig. 3.2-8   Stability margin as a function of gap size.   The open circle shows aluminium shells and the closed circle shows other types of shell.   Thickness shown is that of one of the front plates.   Thickness not shown is 1 cm.
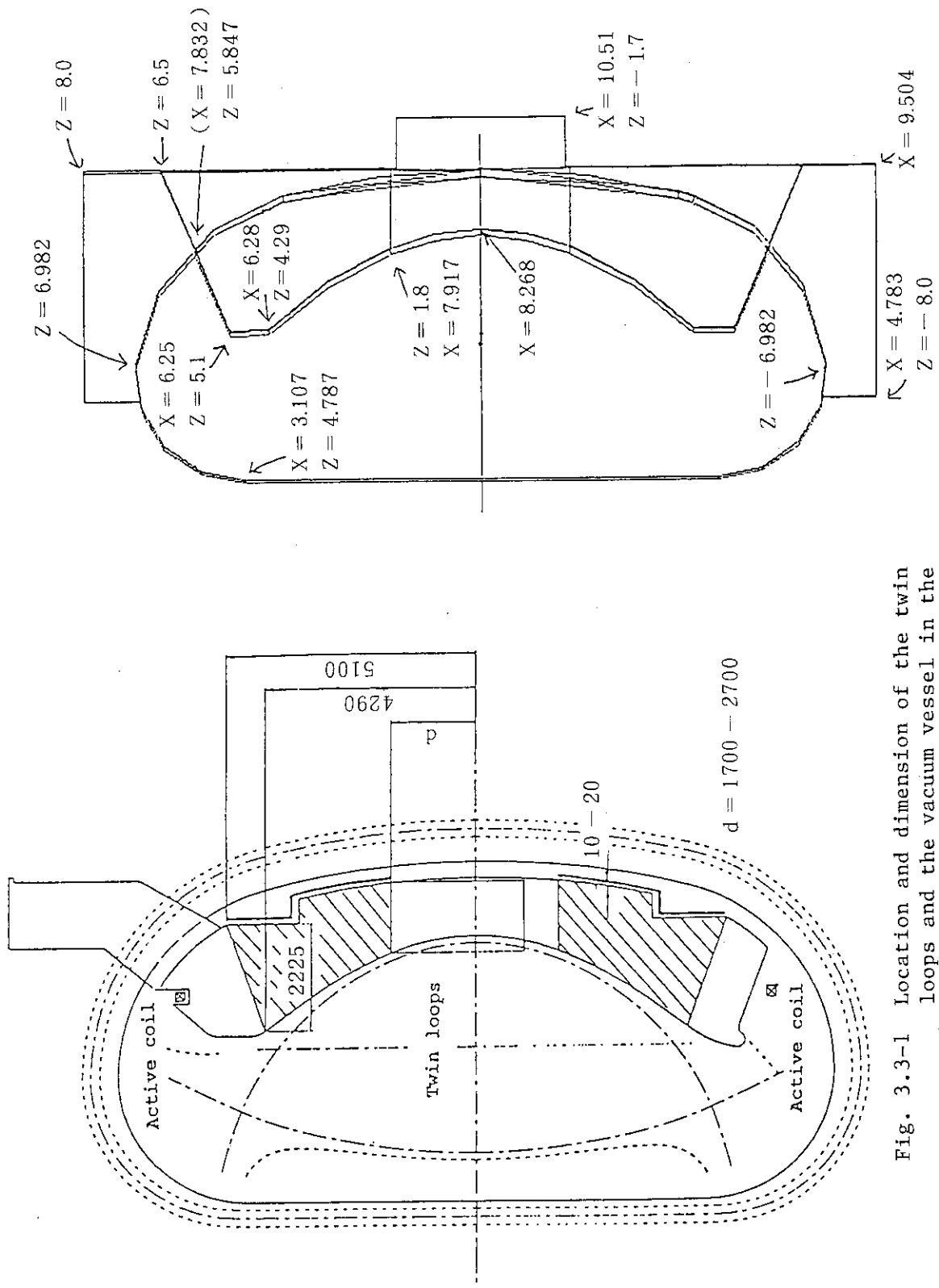
Fig. 3.3-1 Location and dimension of the twin loops and the vacuum vessel in the poloidal cross section of the torus.
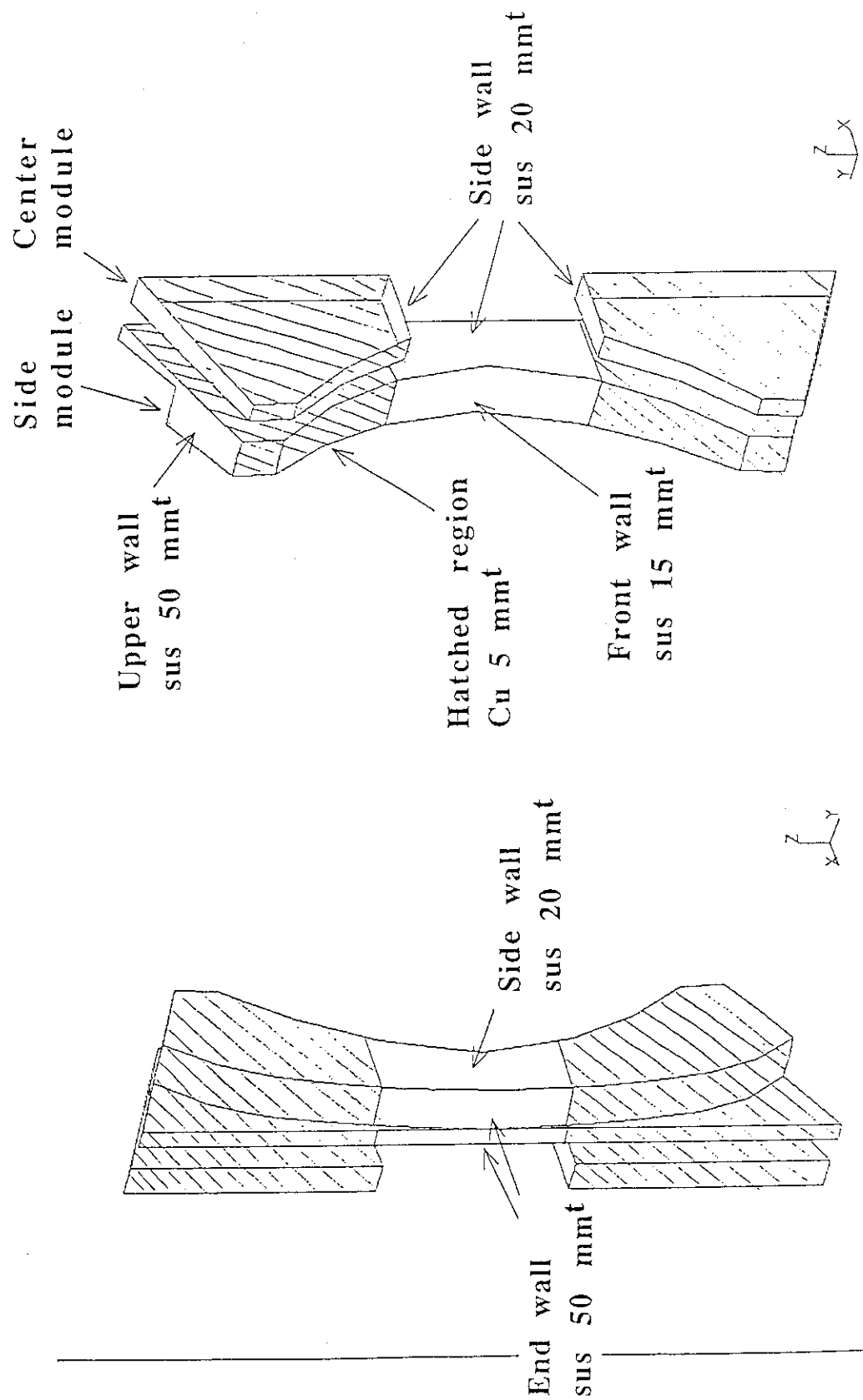
Fig. 3.3-2 Details of the material and thickness of the center and side blanket modules.

Electrical resistivity
sus : 8.2×10^{-7} Ω m
Cu : 1.72×10^{-8} Ω m

Vertical port
sus 50 mm^t

Horizontal port
sus 50 mm^t

Vacuum vessel
sus 200 mm^t

Bellows region
50 mm^t, 10 cm^w
1.8×10^{-6} Ω m

Hatched region
Cu 5 mm^t
(except for bellows)
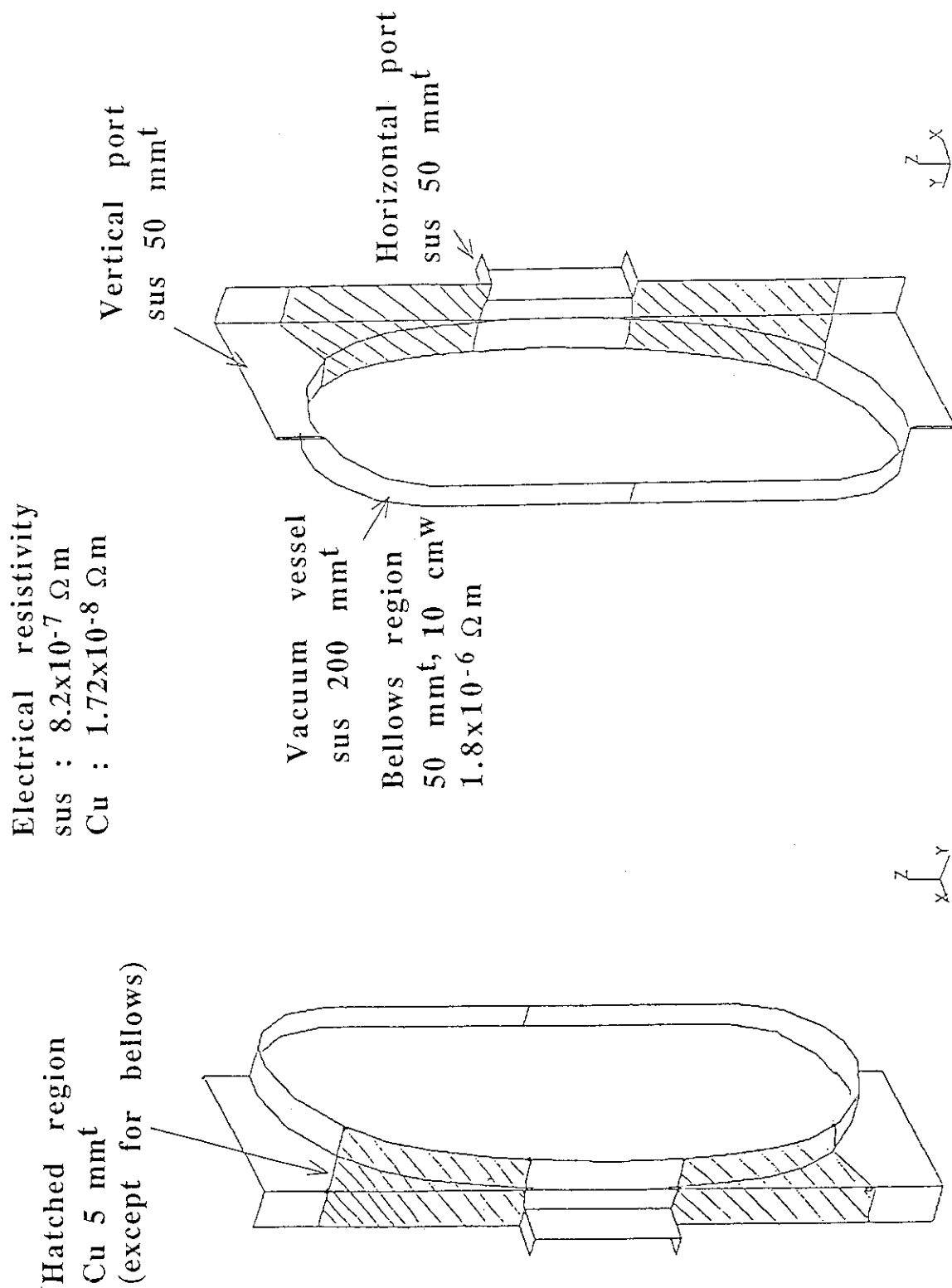
Fig. 3.3-3 Details of the material and thickness of the various region of the vacuum vessel.
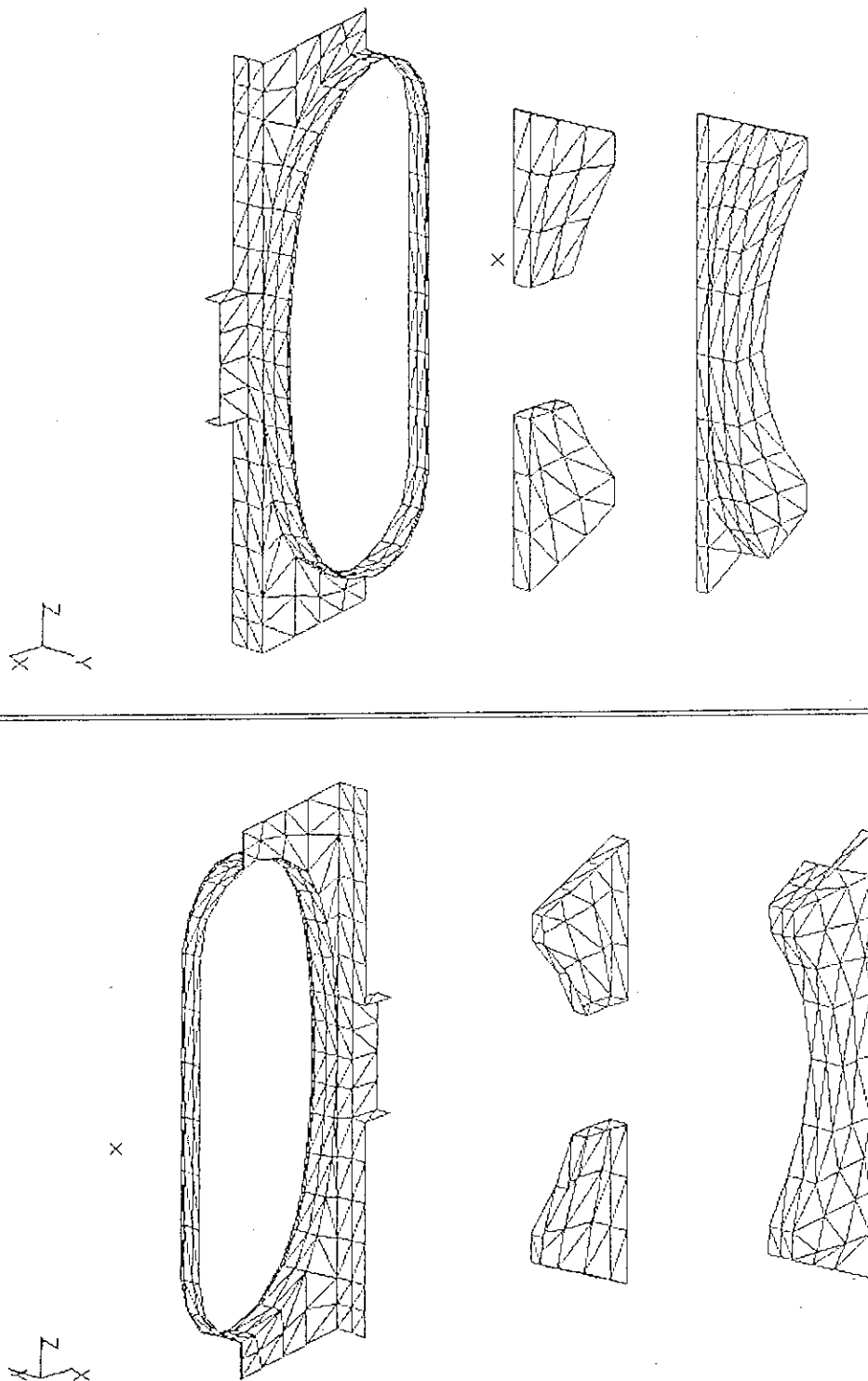
Fig. 3.3-4 Details of mesh for the eddy current calculation by
finite element method.
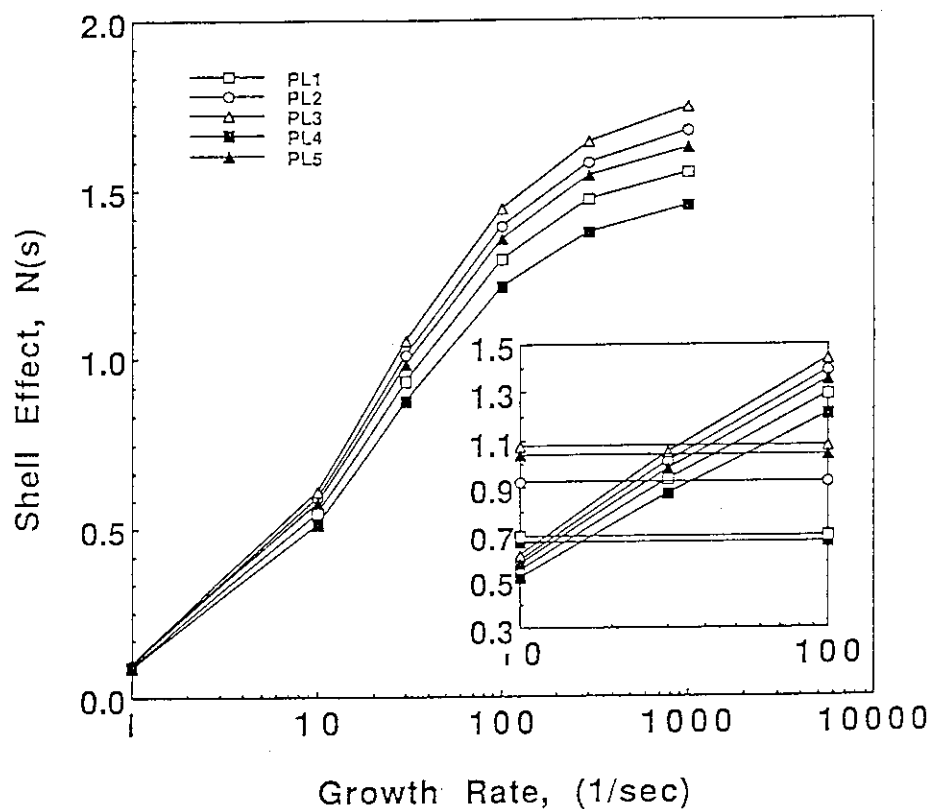
Fig. 3.3-5 N-function of the type 1 shell (ST1) for various plasma conditions (PL1-PL5).
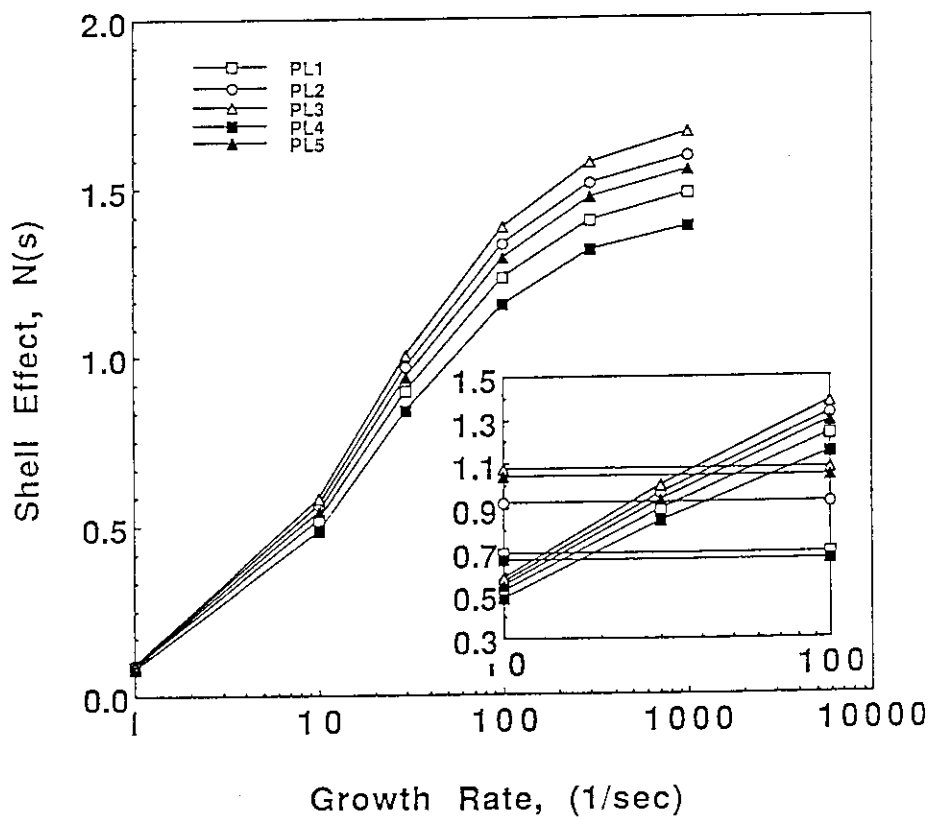
Fig. 3.3-6 N-function of the type 1 shell (ST4) for various plasma conditions (PL1-PL5).
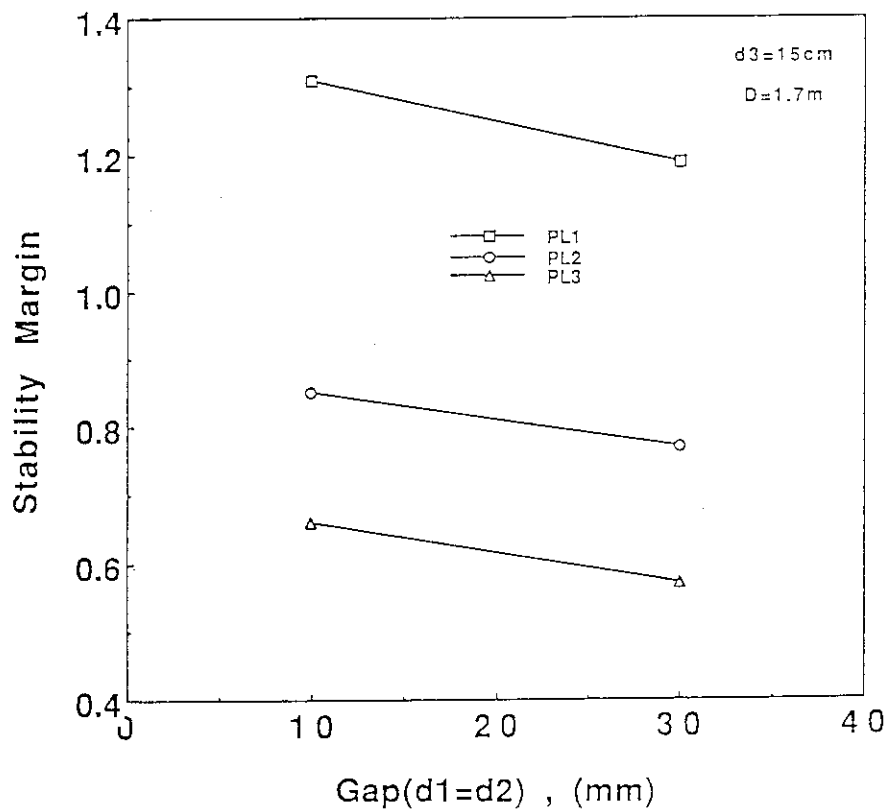
Fig. 3.3-7   Stability margin vs gap width (d1 and d2) of the
shell with d3=15 cm and D=1.7 m for various plasma
conditions (PL1-PL3).
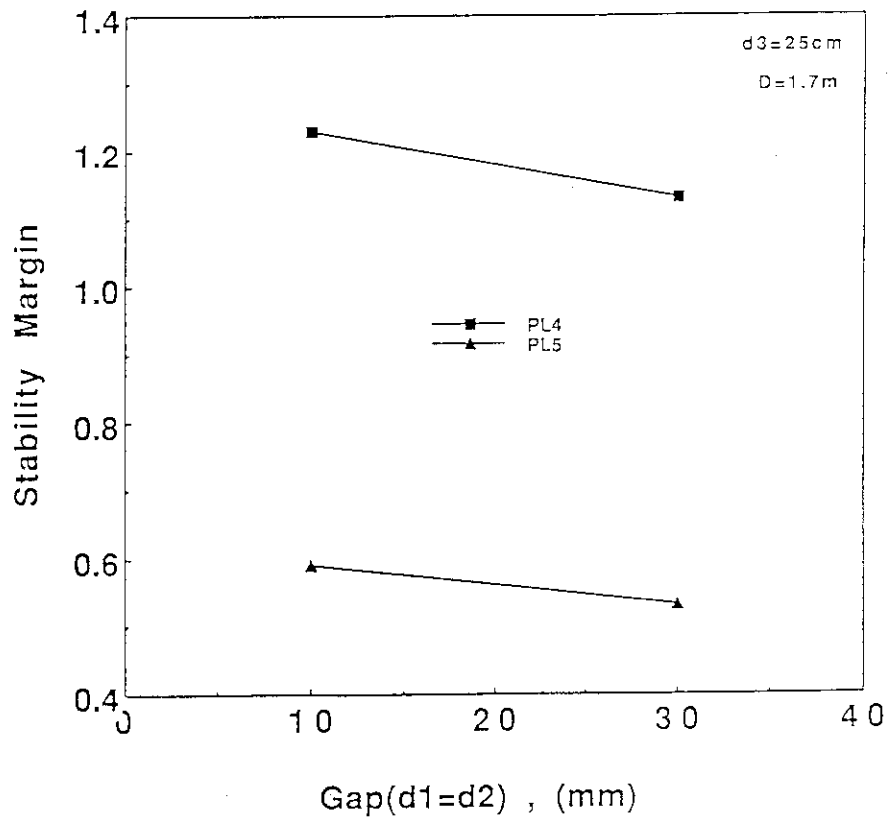
Fig. 3.3-8   Stability margin vs gap width (d1 and d2) of the
shell with d3=25 cm and D=1.7 m for various plasma
conditions (PL4 and PL5).
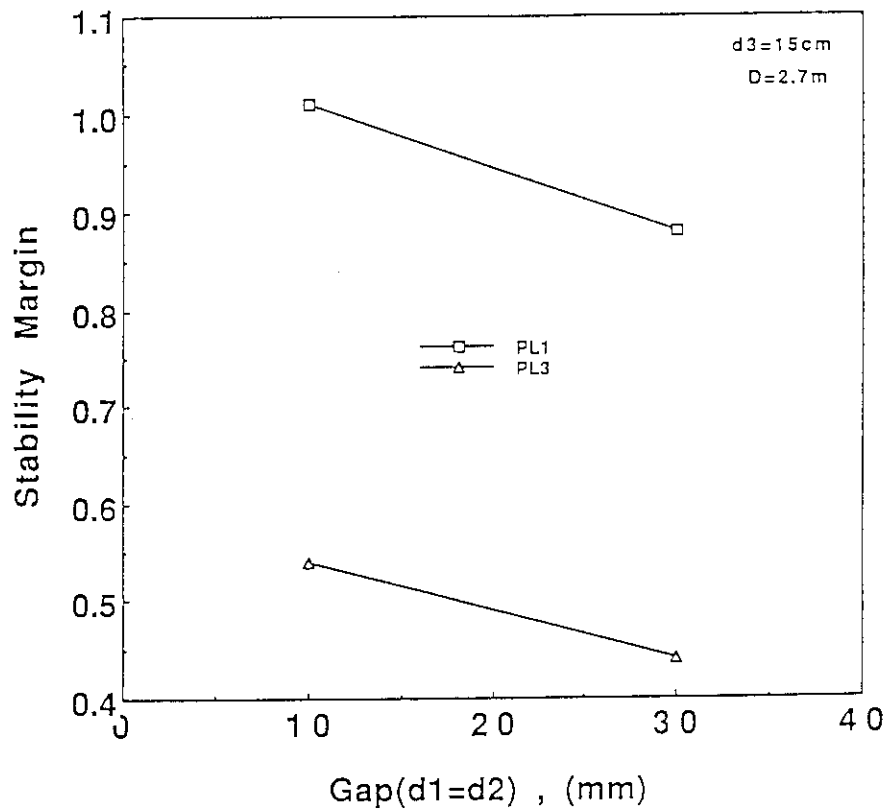
Fig. 3.3-9 Stability margin vs gap width (d1 and d2) of the shell with d3=15 cm and D=2.7 m for various plasma conditions (PL1 and PL3).
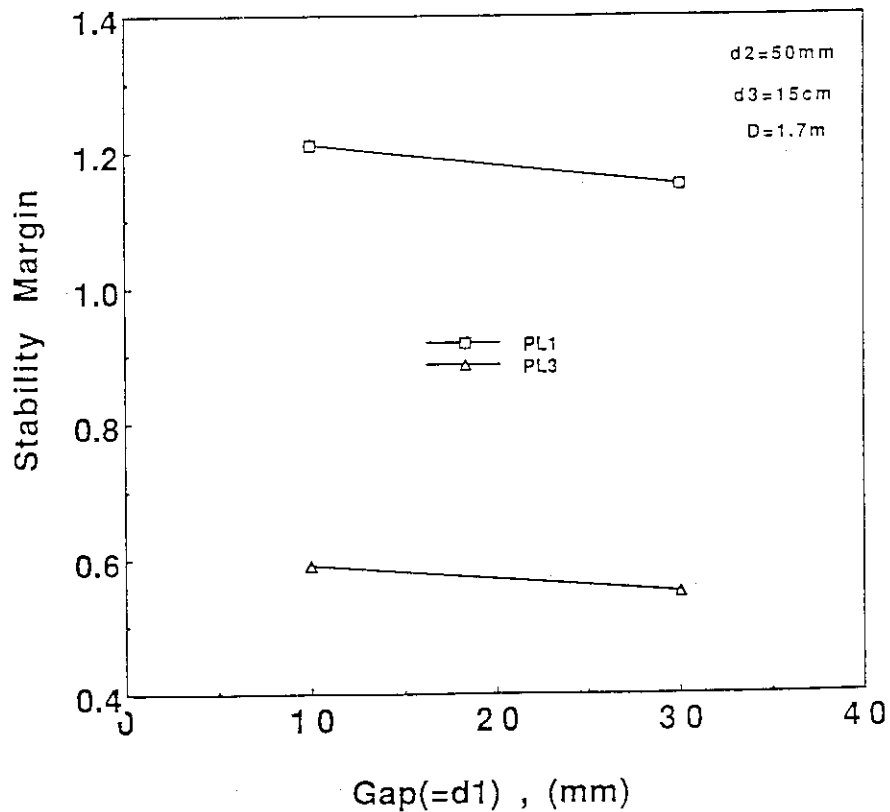
Fig. 3.3-10 Stability margin vs gap width (d1) of the shell with d2=5 cm, d3=15 cm and D=1.7 m for various plasma conditions (PL1 and PL3).
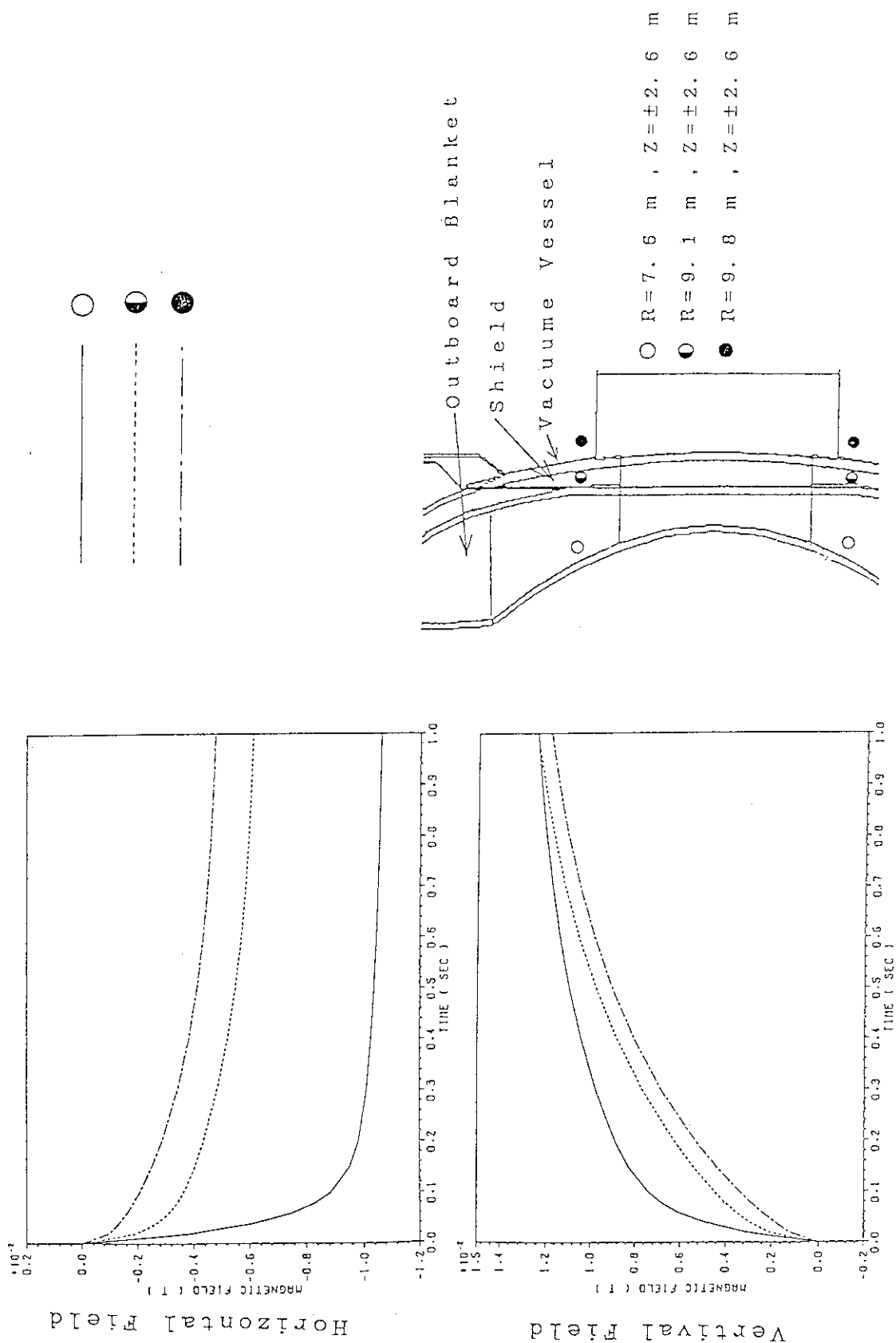
Fig. 3.4-1 Horizontal and vertical magnetic field at plasma center plotted as a funtion of time when 100 kA is imposed stepwise for three different active coil positioning cases. The shell type is twin loop type.

G=3.0x10⁴ V/m

G=1.0x10⁴ V/m

------ CURRENT

——— VOLTAGE

——— Z-SHIFT

G=9.0x10⁴ V/m
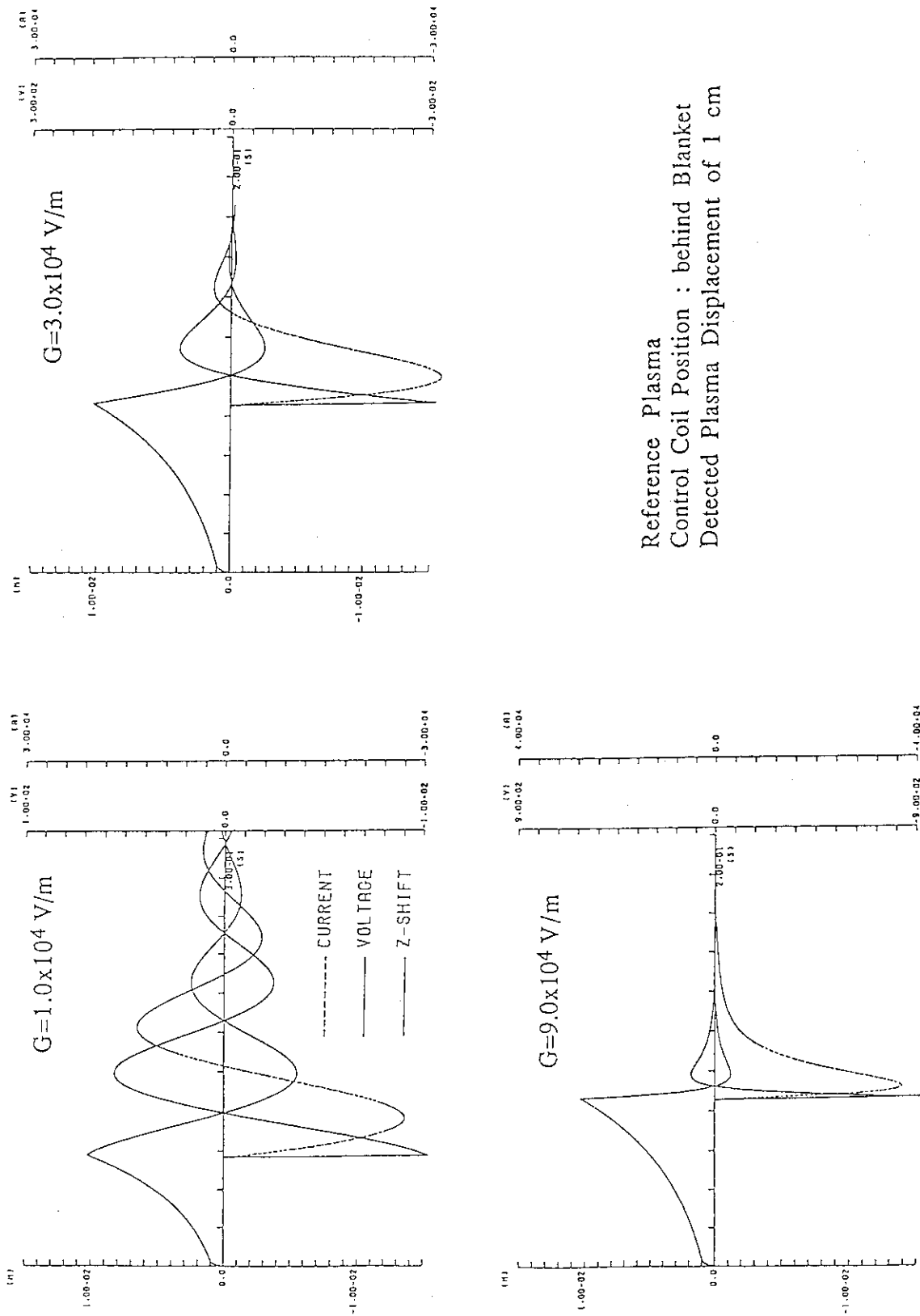
Reference Plasma
Control Coil Position : behind Blanket
Detected Plasma Displacement of 1 cm

Fig. 3.4-2   Dependences of the required current and voltage on the gain G of PID controller.
Control coil position is behind the blanket and the detected plasma displace-
ment is 1 cm.

Reference Plasma
Gain Value of 3.0x10⁴ V/m
Detected Plasma Displacement of 1 cm

Fig. 3.4-3 Dependences of the required coil current and voltage on the control coil position for the gain value of 3×10^4 V/m and the detected plasma displacement of 1 cm.
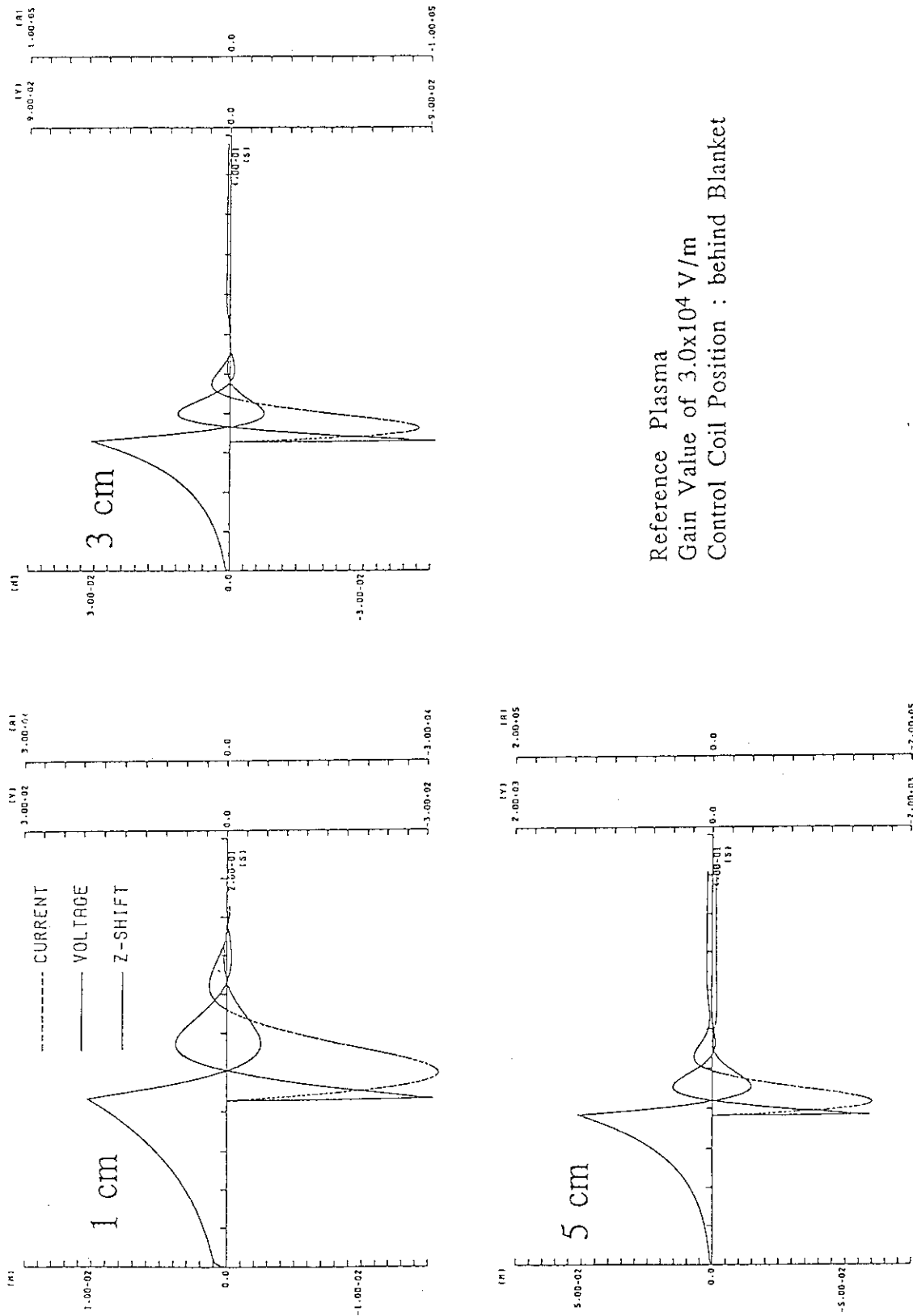
Fig. 3.4-4 Dependences of the required coil current and voltage on the detected point of the plasma displacement for the gain value of 3×10⁴ V/m and the coil position of behind the blanket.

Reference Plasma
Gain Value of 3.0x10⁴ V/m
Control Coil Position : behind Blanket

Gain Value of 3.0×10^4 V/m
Control Coil Position : behind Blanket
Detected Plasma Displacement of 1 cm
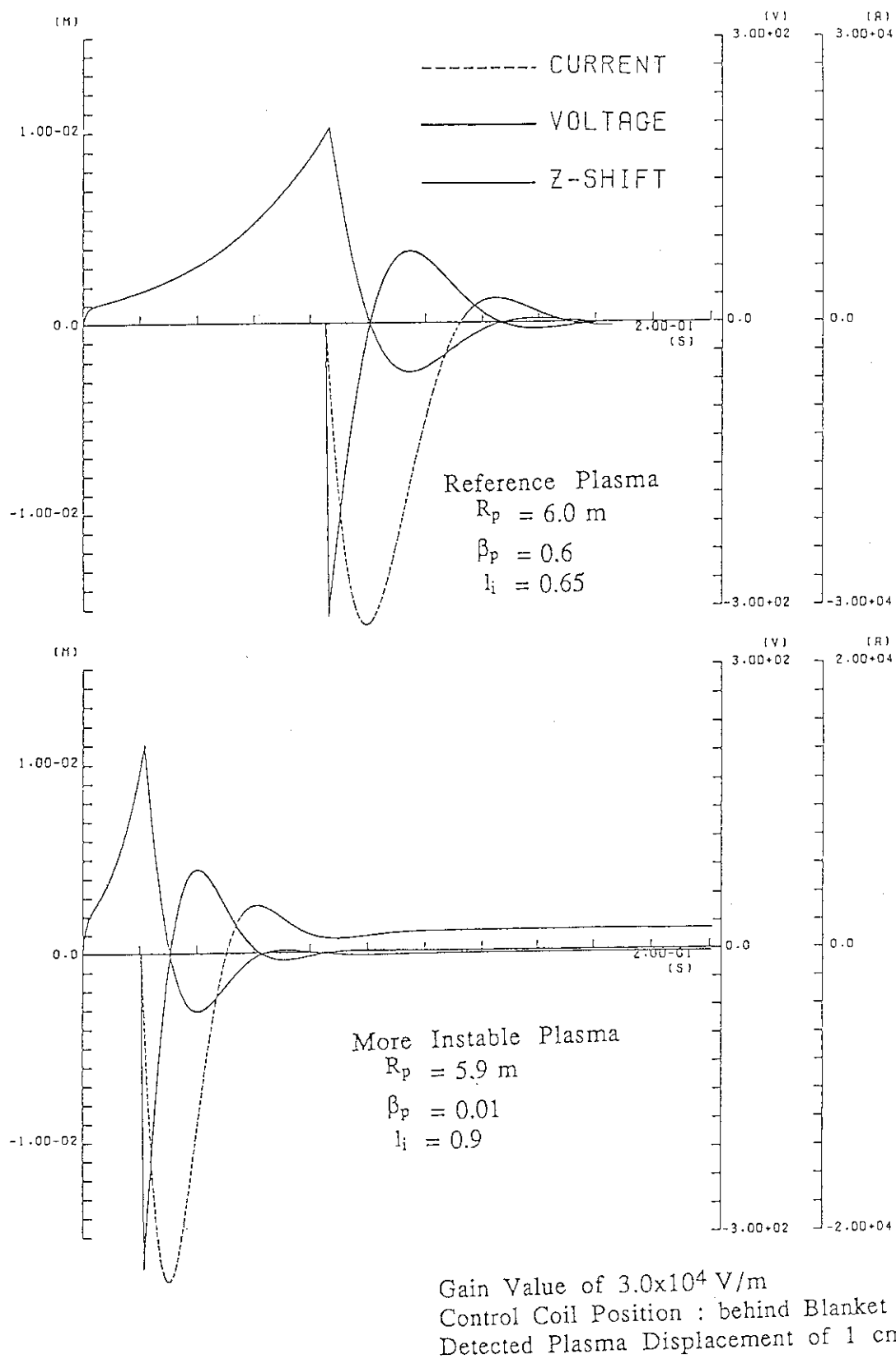
Fig. 3.4-5   Dependences of the required coil current and voltage on the plasma conditions, i.e., the reference plasma with R_p=6 m, β_p=0.6 and 1_i=0.65 and the degraded plasma with R_p=5.9 m, β_p= 0.01 and 1_i=0.9, for the gain value of 3×10^4 V/m, the coil position of behind the blanket and the detected point of the plasma displacement of 1 cm.

4. Plasma control and breakdown/start-up

4.1 Identification of plasma shape and position for the control of ITER

In this section, the identification of plasma shape and position for the control of ITER plasma by using the TOLFEX method is presented as an example of ITER shape and position identification method. the TOLFEX method has been developed for JT-60U to identify the outer-most flux surface and plasma center by using the Legendre-Fourier expansion of the vacuum poloidal flux function in the toroidal coordinates. The features of the TOLFEX method in the application to JT-60U have been concluded as follows;

(1) The TOLFEX method can identify the shape of not only a small circle plasma during the current build-up phase, but also of a up-down asymmetric divertor plasma. A Legendre function of the first kind P has a singular point of (R_0, Z_0), while this point is also identified.

(2) The TOLFEX method can be used by using flux loop only without any magnetic probes. Though a discrete-point boundary condition and a finite series of flux eigenfunctions are adopted, the plasma shape can be well reproduced.

(3) The TOLFEX method can take eddy current into consideration. The uniform field produced by eddy currents is contained in the eigenfunctions of the Legendre function of the second kind Q. If the flux pattern produced by axisymmetric eddy currents is recognized in a certain way, such flux can be added as the additional members of the eigenfunctions.

(4) The TOLFEX method can be performed in real-time, where the table-look-up procedure is applied for the calculation. This makes it possible to apply the TOLFEX method to the feedback control and real-time visualization.

(5) Since (R_0, Z_0) is identified just near the magnetic axis, Z_0 can be used as the vertical plasma position. Feedback control for the vertical plasma position can be started at the step that (R_0, Z_0) has been determined. This leads to the feature that a control cycle can be shortened for suppressing the vertical instability.

Details of the TOLFEX method are presented in Ref.[5,6]. In the

following, the method is applied to ITER plasma. Details of the examined cases are summarized as follows.

(1) Two sets of the flux loops are prepared to examine the sensitivity of the distance between the plasma and the flux loops.

(2) Following several types of ITER plasmas are examined;

   (a) low β divertor plasma with I_p = 22 MA,

   (b) high β divertor plasma with I_p = 22 MA,

   (c) circular limiter plasma with I_p = 4 MA,

   (d) elongated limiter plasma with I_p = 10 MA.

(3) Employed eigenfunctions are as follows;

   (1) Pcos: m=0   : flux produced by a ring-filament current flowing through (R_0, Z_0)

   (2) Pcos: m=2   : flux produced by quadru-pole currents

   (3) Qcos: m=2   : magnetic field for changing ellipticity

   (4) Qcos: m=3   : magnetic field for changing triangularity

   (5) Qsin: m=1   : horizontal magnetic field

Among the indispensable eigenfunctions, [Qcos:m=0 (0-order of vertical magnetic field)] and [Qcos:m=1 (the first order of vertical magnetic field)] are excluded, because they seem to compete with the fluxes produced by ITER PF coils.

(4) Two η (η is an adjusting parameter for over-estimation of the coefficient of Pcos) values are adopted. One is for the calculation of the major radius, vertical position and X-point. The other is for the calculation of the outer-most surface to control the clearance between the plasma and the RF launcher. These cases are summarized in Table 4.1-I.

   Results identified by the TOLFEX method and their comparisons with the results obtained by the equilibrium calculations are shown in Fig. 4.1-1 and summarized in Table 4.1-II.

4.2 Control of the Horizontal Plasma Position during Breakdown

   In ITER, plasma current is planned to be raised with dI_p/dt=1MA/s just after the break down as presented in Fig.4.2-1. During this phase, plasma touches the inboard side of the first wall in the reference scenario. For getting the stable current ramp-up, plasma horizontal position should be kept to be almost the same

value to maintain the power density of the joule heating. Then the reasonable control of the plasma horizontal position is required.

Voltage of PF coils during the early ramp-up phase, just after the plasma initiation, should be controlled as,

$$E = MA_p(d\Phi/dt) + MA_v(dB_z/dt) + M_p(dI_p/dt) \qquad (4.2.1)$$

First term of Eq.(4.2.1) is the supply of the magnetic flux to raise the plasma current. A_p is a coil current vector to produce 1 voltsecond at R=4.5m. $d\Phi/dt=-15.6V$ is required in ITER. The second term is the build-up of the vertical magnetic field. A_v is a coil current vector to produce 1 Gauss at R=4.5m and Z=0.0m. Shafranov magnetic field of -300Gauss is required at t=0.5s to obtain a horizontal equilibrium for the plasma current of 0.5MA with $R_p=4.5m$, $a_p=0.8m$, $Z_p=0m$, $\beta_p=0.01$, $l_i=0.79$. Then $dB_z/dt=-600Gauss/s$ is required. Current vector A_p and A_v are evaluated by the equilibrium calculations as follows.

$$A_p = \begin{matrix} \delta I_{PF1} \\ \delta I_{PF2} \\ \delta I_{PF3} \\ \delta I_{PF4} \\ \delta I_{PF5} \\ \delta I_{PF6} \\ \delta I_{PF7} \end{matrix} = \begin{matrix} 288.5 \\ 288.5 \\ 288.5 \\ 288.5 \\ 282.5 \\ 5.7 \\ 9.75 \end{matrix} \qquad A_v = \begin{matrix} \delta I_{PF1} \\ \delta I_{PF2} \\ \delta I_{PF3} \\ \delta I_{PF4} \\ \delta I_{PF5} \\ \delta I_{PF6} \\ \delta I_{PF7} \end{matrix} = \begin{matrix} 0.65 \\ -0.73 \\ 5.447 \\ 5.758 \\ 0.279 \\ 0.496 \\ 2.443 \end{matrix}$$

The third term comes from the coupling with a plasma current. The resistivity drop of the PF coil is small and is neglected in Eq.(4.2.1). Table 4.2-I presents the comparison of the coil voltages obtained from the above estimation with the reference ones. Good agreement is obtained between them. However, the effects of eddy current are not included in this estimation, that are a)the production of the vertical magnetic field with the raise of the one-turn voltage and b)the shielding effect to the penetration of the vertical magnetic field.

a) Production of the vertical magnetic field

When the one-turn voltage is raised, the error field of B_z is produced by the eddy current that flows in the vacuum vessel and the cryostat. 235Gauss (at 4.5m) is produced at t=0.5 s with the one-turn voltage of 15.6V. Then the required dB_z/dt becomes {-300 (Shafranov) - 235 (Component) } / 0.5s = -1070 Gauss/s.

b) Shielding effect

The shielding effect of eddy current to the penetration of the vertical magnetic field generated by PF coils and in-vessel coils are investigated by a simulation code with the linear ramp-up of PF coil current and in-vessel coils as presented in Fig.4.2-2(a)(b). Time evolution of the penetration rate of B_z inside the vacuum vessel is presented in Fig.4.2-2(c). Only about 30% penetration is obtained at t=0.1s. On the other hand, the maximum ramp-up rate of B_z is limited to be 2000 Gauss/s due to the available coil voltage of 20kV from the design constraints of PF coils (especially PF6) as presented in Table 4.2-II. Then dB_z/dt in the vacuum vessel (R=4.5m) is reduced by the shielding effect of eddy current as follows,

	% of penetration	dB_z/dt
t=0.1s	31%	-620Gauss/s
t=0.2s	41%	-820Gauss/s
t=0.3s	47%	-940Gauss/s
t=0.4s	51%	-1040Gauss/s
t=0.5s	55%	-1100Gauss/s

Thus the required B_z of -1070Gauss/s is only obtained at t=0.5s. With this penetration rate, a plasma shifts to the outside by ~1.0m just after the plasma initiation at t=0.1~0.2s, owing to the insufficient B_z as presented in Fig.4.2-3. Then it should be necessary to increase the ramp-up rate of B_z. Several possible solutions are presented as follows;

1)De-block of PF6 coil into two coils

1.3x-2000Gauss/s can be generated by this de-blocking of PF6. Limit of the improvement factor 1.3 is attributed to the fact that the coil voltages of PF4 and PF7 are already 15kV and can only be

increased from 15kV to 20kV (20kv/15kV=~1.3). Then -800Gauss/s can be added at R=4.5m, t=0.1s, and the outward plasma shift can be decreased to 0.3~0.6m.

2)Installation of the in-vessel coils

In-vessel coils installed at R=9.1m and Z=±2.6m can produce the vertical field of 45Gauss at R=4.5m with 30kAT, n_{index} of which is nearly zero as presented in Fig.4.2-4. With 1kV power supply, control speed of -3600Gauss/s can be obtained at t=0.1s. Thus coil current of 100kAT increases the controllability of B_z with the maximum available field of 150Gauss.

3)Decrease in the ramp-up rate of plasma current

If the ramp-up rate of plasma current could be lowered as <1.0MA/s, the one-turn voltage and the associated ramp-up rate of B_z could also be decreased proportionally. In this case, the requirement on the maximum coil voltage of PF coils can naturally be relaxed. However, there are some concerns, in which the radiation barrier could really be overcome by such small ramp-up rate even with additional heating of ECH. Further information from physics data base is necessary for this ramp-up scheme to be employed for the reference operation scenario.

4.3 Slow control algorithm of the plasma shape

4.3.1 Control Variables

In ITER, two control loops are designed for the plasma shape control. Slow control loop will be performed by superconductor PF (Poloidal magnetic Field) coils with the characteristic frequency of ≤ ~0.3Hz to control the plasma current and the plasma shape. Fast control loop will be performed by normal conductor in-vessel coils with the characteristic frequency of 5~10Hz to control the vertical plasma position to stabilize the positional instability due to the highly elongated plasma of k~2.0.

In the slow control loop, I_p, R_{out}, R_{in}, Z_p, R_n and Z_n are selected as the control variables. Definitions of them are presented in

Fig.4.3-1. Plasma current I_p must be controlled to be the required value according to the operational scenario. R_{out} and R_{in} are the horizontal locations of the outside and inside outermost plasma (separatrix) surface at the same vertical height with the plasma current axis. Each of R_{out} and R_{in} determines the clearance between the plasma outermost surface and the first wall, which should be kept at reasonable value to guide most of the power and particles to the divertor and to decrease the erosion of the first wall caused by the charge exchange. Furthermore, R_{out} should be controlled to get the good coupling between a plasma and a launcher of LHW. R_{in} should be controlled to get a clearance of $> \sim 10$cm in order to avoid the touch of a plasma to the first wall under the inward horizontal shift caused by a minor disruption. Control of Z_p is necessary to equalize the heat load onto two divertor plates, that are installed at the top and bottom of the first wall. Low frequency component of the in-vessel coil current I_{in}, which is to be used for the fast control of Z_p, should be decreased to maintain the control margin of Z_p. Thus the minimization of D.C. current component in I_{in} is also the important control objective of the slow control loop of Z_p. R_n and Z_n are the horizontal and vertical location of a null point, that should be controlled to guide the separatrix lines onto the divertor plate. ITER has a double null divertor configuration. Thus locations of two null points should be controlled. Swing of the separatrix lines on the divertor plate is also required to decrease the heat flux effectively. These requirements on the slow control loop are summarized in Table 4.3-I.

4.3.2 Non-interacting Control Method

6(+2) control variables should be controlled by ITER hybrid poloidal coil system, which consists of 14 coils. Then the control system inevitably becomes a multi-variable one. In JT-60, the application of the non-interacting control method was investigated to swing the separatrix line on the divertor plate with keeping the configuration of a bulk plasma [7], and was found out to be the powerful control method. Thus this control algorithm is re-examined for the control of the plasma current and the plasma shape in ITER.

When the proportional control with the compensation of the resistivity drop is adopted, the voltage vector E becomes,

$$E = RI + RG_x I_p(x^{ref} - x) + RG_p(I_p^{ref} - I_p) \qquad (4.3.1)$$

Usually, the resistivity drop of RI is negligibly small. Here x is the vector of control variables (R_{out}, R_{in}, Z_p, R_n and Z_n), and x^{ref} is the reference values of them. I_p^{ref} is the reference value of the plasma current. G_x is a matrix gain of the plasma shape, and G_p is a diagonal matrix gain of the plasma current. These gains multiplied by a diagonal matrix of resistivity R can be estimated from the circuit equations of a plasma current I_p and PF coil currents I, and the relation between the displacements of control variables dx from the equilibrium state and that of PF coil currents δI ($\delta I = A I_p \delta x$) as follows [8].

$$RG_x = (MA_x + \partial M_{pc}/\partial x)2\pi f_x \qquad (4.3.2)$$

$$RG_p = (MA_p + M_{pc})2\pi f_p \qquad (4.3.3)$$

Here the control frequencies of a plasma current and plasma shape are denoted by f_p and f_x. The diagonal matrix f_x is selected in the non-interacting control algorithm. M is a mutual inductance matrix of PF coils. M_{pc} is a vector of the mutual inductance between a plasma current and PF coil currents. A_p is investigated from the difference in the influx of voltsecond $d\Phi$ supplied by two sets of PF coil currents, that makes the same plasma shape with the difference in the plasma current δI_p.

$$dI = (L_p/d\Phi)(I_1 - I_2)dI_p = A_p \delta I_p \qquad (4.3.4)$$

A_x can be obtained by the usage of the code to analyze the equilibrium plasma configuration. Each control variable is displaced with keeping the other ones fixed, the plasma current and the influx of voltsecond. To get the unique solution of A_x, some restrictions on the coil currents is required, because the number of control variables is smaller than that of coils. When Δx is displacement of one control variable, and ΔI_x is the displacement of coil currents associated with

this displacement Δx, the required δI_x for $I_p \delta x$ is,

$$\delta I = (\Delta I_x /(I_p \Delta x)) I_p \delta x \qquad (4.3.5)$$

This relation can be obtained for each control variables. Then A_x can be estimated as,

$$A_x = \Delta I_x /(I_p \Delta x) \qquad (4.3.6)$$

Matrix $A = (A_x, A_p)$ used in the SOFT phase is presented in Table 4.3-II. Each magnetic field pattern produced by PF coil currents for each control variable, that is same with each vector of matrix A of Table 4.3-II, are presented in Fig.4.3-2. Characteristic feature of the field pattern can be seen for each case, e.g., strong vertical field is generated near the outer most plasma surface on the midplane, while fairly small near the inner-most surface to produce the displacement of only R_{out}, R_{in}. Matrix A is to be changed with the plasma configuration. Thus, Matrix A must be determined for each configuration in the operation scenario, which is presented in Table 4.3-III. A set of Matrix A is presented in Table 4.3-IV for each of the phase of operation scenario. RG is easily calculated from matrix $A = (A_x, A_p)$ using Eqs.(4.3.1)~(4.3.3). Following these procedure, quantitative estimation on the required voltage of the coil power supply can be done by specifying the control frequencies and the results are presented in Table 4.3-V for the EOB phase plasma.

The effect of eddy current, which flows in the machine components (e.g. vacuum vessel, cryostat), is not included explicitly in the investigation of a matrix gain presented above, because, in this slow control, the feedback control frequency is usually selected to be lower than the characteristic frequency of eddy current. If it is selected to be too high, the system will become unstable owing to the time delay caused by the shielding effect of eddy current. Thus the optimum control frequency should be investigated by a simulation code, which includes the effect of eddy current.

Table 4.1-I Examined cases by TOLFEX method for ITER plasmas.

ITEMS		Divertor(22MA)		Limiter		Note
		βp=0.1	βp=1.0	4MA Circle	11MA Elongated	
plasma-sensor distance	Type A	η=1.0 / η=0.7 Fig. 4.1.1(a)	η=1.0 / η=0.7 Fig. 4.1.1(b)	———	———	short
	Type B	η=1.0 / η=0.7 Fig. 4.1.1(c)	η=1.0 / η=0.7 Fig. 4.1.1(d)	η=1.0 Fig. 4.1.1(e)	η=1.0 Fig. 4.1.1(f)	long

Table 4.1-II Identified ITER plasma parameters by TOLFEX method and comparisons of them with the results of equilibrium code.

ITEMS			Divertor(22MA)		Limiter		Note
			βp=0.1	βp=1.0	4MA Circle	11MA Elongated	
Rp	Equilibrium		5.999 m	6.000 m	5.700 m	5.854 m	
	A	TOLFEX	5.984 m	5.972 m	———	———	η=1.0, short
	B	TOLFEX	5.967 m	5.950 m	5.640 m	5.843 m	η=1.0, long
Zp	Equilibrium		1.96E-5 m	1.06E-4 m	0 m	0 m	
	A	TOLFEX	1.45E-3 m	1.33E-3 m	———	———	η=1.0, short
	B	TOLFEX	6.55E-4 m	1.01E-3 m	1.65E-4 m	-1.48E-3 m	η=1.0, long
Rx	Equilibrium		4.709 m	4.709 m	———	———	
	A	TOLFEX	4.730 m	4.720 m	———	———	η=1.0, short
	B	TOLFEX	4.680 m	4.680 m	———	———	η=1.0, long
Zx	Equilibrium		-4.780 m	-4.780 m	———	———	
	A	TOLFEX	-4.606 m	-4.747 m	———	———	η=1.0, short
	B	TOLFEX	-4.852 m	-4.808 m	———	———	η=1.0, long
Rout	Equilibrium		8.149 m	8.151 m	———	———	
	A	TOLFEX	8.123 m	8.148 m	———	———	η=0.7, short
	B	TOLFEX	8.135 m	8.108 m	———	———	η=0.7, long

Table 4.2-I Voltages of PF coils (kV). Comparison of the PF coil
voltages estimated from Eq.(4.2.1) and the reference
ones in the early rampup phase.

	MA_p	MA_v	Mp		Reference
	$(d\Phi/dt)$	(dB_z^{eq}/dt)	(dI_p/dt)	TOTAL	Voltages at $t=0.1-0.6s$[kV]
PF1	-5.691	-0.033	0.705	-5.019	-5.015
PF2	-5.682	-0.917	0.437	-6.162	-6.132
PF3	-5.613	-3.851	0.232	-9.233	-9.481
PF4	-4.993	-4.063	0.126	-8.930	-9.114
PF5	-7.673	-1.803	0.203	-9.273	-8.964
PF6	-3.905	-5.803	0.772	-8.941	-9.849
PF7	-2.373	-4.956	0.655	-6.674	-6.250

Table 4.2-II Voltages of PF coils (kV) for $dB_z/dt=-2000$Gauss/s.
Voltage of PF6 is close to the limit of -20kV.

	MA_p	MA_v	Mp		
	$(d\Phi/dt)$	(dB_z/dt)	(dI_p/dt)	TOTAL	
PF1	-1.262	-0.109	0.437	-0.666	
PF2	-1.260	-3.057	0.232	-3.880	
PF3	-1.244	-12.84	0.232	-13.85	
PF4	-1.107	-13.54	0.126	-14.52	
PF5	-1.701	-6.009	0.203	-7.507	
PF6	-0.865	-19.36	0.772	-19.45	<- near -20kV
PF7	-0.526	-16.52	0.655	-16.39	

Table 4.3-I Requirements on control variables in the slow control loop.

Control Variables	Required Range	Control Issue	Ref.	Time Issue
R_{out}	±2cm	CX erosion RF coupling	1) 2)	~1s
R_{in}	±2cm	CX erosion disruption survivability	1) 3)	~1s
Z_p	±(0.5-1)cm	divertor heat load(~20%)	4)	~1s
$(R_x, Z_x)^U$ $(R_x, Z_x)^L$	±2cm	divertor heat load location	5)	~1s
I_p	±0.1MA	plasma performance	6)	~1s

1)Large clearance of ~15cm between the separatrix and the first wall is required to decrease the CX erosion.
2) n_e of $0.5~4.5 \times 10^{18}$/m^3 is necessary for the coupling of LHW(5~6GHz)
3)>~10cm is necessary to avoid the contact of plasma to the inner side of vacuum wall at a disruption.
4)In the double null condition, the allowable Z_p displacement depends on the profile of the radial power flow outside the separatrix line. Short decay length of 0.5cm is expected. Thus power fluctuation of 20~30% on the divertor plate may be produced by ~3mm separation of separatrix at the midplane. This requires the very precise control of Z_p with ~3mm.
5)To keep the separatrix line on the divertor plate (±2cm displacement of null point moves the striking point at most ±8cm on the divertor plate)..
6)Soft-landing at the emergency shut-down is ~-400kA/s

Table 4.3-Ⅱ Matrix A (kAT). Controlled plasma is in the SOFT phase
$[I_p=22MA$, $R_p/a_p=6.0/2.15m$, $\beta_p/1_i=0.6/0.65]$. Unit of
R_{out}, Z_p, R_n, Z_n is [cm], and that of I_p and I_{in} is [KA].

	Rout	Rin	Rn	Zn	Z_p+cI_{in}	Ip
1U	-7.159E+01	2.475E+01	2.800E+01	-4.590E+00	-2.300E+01	1.453E+00
2U	-7.159E+01	2.475E+01	2.800E+01	-4.590E+00	-2.300E+01	1.453E+00
3U	3.477E+02	-4.604E+01	-2.010E+02	-1.530E+00	-5.530E+01	1.533E+00
4U	5.193E+01	2.178E+01	-9.200E+00	-7.776E+01	-6.220E+01	1.559E+00
5U	-1.287E+02	5.673E+01	1.412E+02	-1.485E+02	-1.190E+01	7.860E-01
6U	1.664E+02	-1.266E+02	4.400E+00	1.451E+02	-3.360E+01	6.480E-02
7U	-1.039E+02	9.119E+01	-1.040E+01	-7.929E+01	3.360E+01	5.700E-03
1L					2.300E+01	
2L					2.300E+01	same
3L		same with above			5.530E+01	with
4L					6.220E+01	above
5L					1.190E+01	
6L					3.360E+01	
7L					-3.360E+01	

Table 4.3-Ⅲ Operational scenario during the divertor configuration.

case No.	DN E002	DN F002	SOFT SOFT003	SOB SOB003	EOB EOB003	EOC EOC003	DN H002	DN I002
Time(sec)	28.00	44.00	70.00	90.00	290.00	310.00	330.00	350.00
Plasma(MA)	10.00	15.00	22.00	22.00	22.00	20.00	15.00	10.00
PF1(MA)	4.72	-4.11	-17.43	-17.74	-22.65	-23.16	-23.90	-18.90
PF2(MA)	4.72	-4.11	-17.43	-17.74	-22.65	-23.16	-23.90	-18.90
PF3(MA)	14.10	10.73	1.97	-2.22	-10.16	-10.32	-8.55	-9.24
PF4(MA)	14.10	5.93	0.00	0.00	0.00	0.00	-16.58	-16.52
PF5(MA)	13.40	15.03	13.97	11.74	6.78	5.44	5.15	1.62
PF6(MA)	-4.14	-6.95	-9.69	-7.70	-6.99	-7.94	-7.77	-5.35
PF7(MA)	-0.81	-1.15	-2.30	-4.50	-5.02	-2.76	-1.24	-0.83
Rp(m)	6.00	6.00	6.00	6.00	6.00	6.00	6.00	6.00
ap(m)	2.15	2.15	2.15	2.15	2.15	2.15	2.15	2.15
b/a	2.00	2.00	2.00	2.00	2.00	2.00	2.00	2.00
c/a	0.40	0.40	0.40	0.40	0.40	0.40	0.40	0.40
βP	0.09	0.10	0.10	0.61	0.61	0.11	0.10	0.09
li	0.64	0.64	0.65	0.65	0.65	0.64	0.64	0.64
q								
PSI	16.81	-44.80	-138.00	-160.00	-192.00	-173.47	-163.70	-130.92
DPSI(res)								
DPSI(ind)								
DPSI(tot)	116.69	178.30	271.50	293.50	325.50	306.97	294.20	264.42
Lp	8.79	8.81	8.84	9.26	9.27	8.81	8.81	8.80

Table 4.3-IV Matrix A = (A_x,A_p) [kAT/cm or kAT/kA].

E002

	Rout	Rin	Rn	Zn	Zp	Ip
PF1U	-2.754E+01	6.910E+00	1.077E+01	-1.250E+00	-4.066E+01	1.453E+00
PF2U	-2.754E+01	6.910E+00	1.077E+01	-1.250E+00	2.743E+01	1.453E+00
PF3U	1.151E+02	-1.093E+01	-6.570E+01	-7.300E+00	-6.442E+01	1.533E+00
PF4U	1.151E+02	-1.093E+01	-6.570E+01	-7.300E+00	2.413E+01	1.559E+00
PF5U	-8.958E+01	2.922E+01	8.050E+01	-8.350E+01	-2.716E+01	7.860E-01
PF6U	8.429E+01	-5.397E+01	4.800E-01	6.898E+01	3.910E+00	6.480E-02
PF7U	-5.229E+01	3.857E+01	-4.280E+00	-3.743E+01	7.350E+00	5.700E-03
PF1L	-2.754E+01	6.910E+00	1.077E+01	-1.250E+00	2.858E+00	1.453E+00
PF2L	-2.754E+01	6.910E+00	1.077E+01	-1.250E+00	1.879E+00	1.453E+00
PF3L	1.151E+02	-1.093E+01	-6.570E+01	-7.300E+00	1.680E+01	1.533E+00
PF4L	1.151E+02	-1.093E+01	-6.570E+01	-7.300E+00	-2.778E+01	1.559E+00
PF5L	-8.958E+01	2.922E+01	8.050E+01	-8.350E+01	1.252E+01	7.860E-01
PF6L	8.429E+01	-5.397E+01	4.800E-01	6.898E+01	-3.222E+00	6.480E-02
PF7L	-5.229E+01	3.857E+01	-4.280E+00	-3.743E+01	1.107E+00	5.700E-03

F002

	Rout	Rin	Rn	Zn	Zp	Ip
PF1U	-5.367E+01	1.692E+01	2.391E+01	-2.810E+00	-6.257E+01	1.453E+00
PF2U	-5.367E+01	1.692E+01	2.391E+01	-2.810E+00	6.645E+01	1.453E+00
PF3U	3.724E+02	-1.134E+02	-2.144E+02	0.0	-2.158E+02	1.533E+00
PF4U	-2.811E+02	1.899E+02	-1.492E+02	-3.785E+01	2.540E+02	1.559E+00
PF5U	3.909E+01	-3.228E+01	3.220E+01	-1.132E+02	-1.148E+02	7.860E-01
PF6U	5.466E+01	-5.274E+01	3.306E+01	9.546E+01	2.068E+01	6.480E-02
PF7U	-4.025E+01	4.336E+01	-2.319E+01	-5.142E+01	-2.410E+00	5.700E-03
PF1L	-5.367E+01	1.692E+01	2.391E+01	-2.810E+00	4.534E+00	1.453E+00
PF2L	-5.367E+01	1.692E+01	2.391E+01	-2.810E+00	7.970E-01	1.453E+00
PF3L	3.724E+02	-1.134E+02	-2.144E+02	0.0	1.316E+01	1.533E+00
PF4L	-2.811E+02	1.899E+02	-1.492E+02	-3.785E+01	-1.758E+01	1.559E+00
PF5L	3.909E+01	-3.228E+01	3.220E+01	-1.132E+02	1.007E+01	7.860E-01
PF6L	5.466E+01	-5.274E+01	3.306E+01	9.546E+01	-1.687E+00	6.480E-02
PF7L	-4.025E+01	4.336E+01	-2.319E+01	-5.142E+01	1.300E-02	5.700E-03

Table 4.3-IV (Continued)

SOB003

	Rout	Rin	Rn	Zn	Zp	Ip
PF1U	-7.107E+01	2.832E+01	2.930E+01	-4.150E+00	-7.216E+01	1.453E+00
PF2U	-7.107E+01	2.832E+01	2.930E+01	-4.150E+00	1.741E+02	1.453E+00
PF3U	3.519E+02	-4.016E+01	-2.068E+02	-3.422E+01	-2.280E+02	1.533E+00
PF4U	0.0	0.0	0.0	0.0	0.0	1.559E+00
PF5U	-1.132E+02	7.089E+01	1.369E+02	-1.792E+02	7.290E+00	7.860E-01
PF6U	1.537E+02	-1.335E+02	7.890E+00	1.482E+02	-5.546E+01	6.480E-02
PF7U	-9.580E+01	7.469E+01	-1.248E+01	-7.956E+01	4.293E+01	5.700E-03
PF1L	-7.107E+01	2.832E+01	2.930E+01	-4.150E+00	-1.092E+01	1.453E+00
PF2L	-7.107E+01	2.832E+01	2.930E+01	-4.150E+00	2.893E+01	1.453E+00
PF3L	3.519E+02	-4.016E+01	-2.068E+02	-3.422E+01	-1.310E+01	1.533E+00
PF4L	0.0	0.0	0.0	0.0	0.0	1.559E+00
PF5L	-1.132E+02	7.089E+01	1.369E+02	-1.792E+02	1.332E+01	7.860E-01
PF6L	1.537E+02	-1.335E+02	7.890E+00	1.482E+02	-4.193E+00	6.480E-02
PF7L	-9.580E+01	7.469E+01	-1.248E+01	-7.956E+01	8.670E-01	5.700E-03

EOB003

	Rout	Rin	Rn	Zn	Zp	Ip
PF1U	-7.077E+01	2.554E+01	2.935E+01	-1.770E+00	-1.397E+02	1.453E+00
PF2U	-7.077E+01	2.554E+01	2.935E+01	-1.770E+00	3.393E+02	1.453E+00
PF3U	3.527E+02	-4.074E+01	-2.088E+02	-4.899E+01	-3.670E+02	1.533E+00
PF4U	0.0	0.0	0.0	0.0	0.0	1.559E+00
PF5U	-1.130E+02	7.126E+01	1.506E+02	-1.741E+02	5.757E+01	7.860E-01
PF6U	1.536E+02	-1.345E+02	-2.380E+00	1.506E+02	-8.695E+01	6.480E-02
PF7U	-9.582E+01	9.549E+01	-6.780E+00	-8.133E+01	5.797E+01	5.700E-03
PF1L	-7.077E+01	2.554E+01	2.935E+01	-1.770E+00	-1.793E+01	1.453E+00
PF2L	-7.077E+01	2.554E+01	2.935E+01	-1.770E+00	4.470E+01	1.453E+00
PF3L	3.527E+02	-4.074E+01	-2.088E+02	-4.899E+01	-2.518E+01	1.533E+00
PF4L	0.0	0.0	0.0	0.0	0.0	1.559E+00
PF5L	-1.130E+02	7.126E+01	1.506E+02	-1.741E+02	1.829E+01	7.860E-01
PF6L	1.536E+02	-1.345E+02	-2.380E+00	1.506E+02	-8.760E+00	6.480E-02
PF7L	-9.582E+01	9.549E+01	-6.780E+00	-8.133E+01	3.740E+00	5.700E-03

EOC003

	Rout	Rin	Rn	Zn	Zp	Ip
PF1U	-8.544E-06	2.914E-06	3.888E-06	-2.624E-07	-7.197E-03	7.008E-03
PF2U	3.058E-06	1.384E-06	-2.384E-06	-2.278E-06	-1.189E-03	7.040E-03
PF3U	3.540E-05	-2.826E-06	-1.986E-05	-8.057E-06	-4.055E-04	0.0
PF4U	1.011E-05	0.0	-1.972E-06	-7.017E-06	-2.062E-04	0.0
PF5U	-2.288E-05	1.481E-05	4.959E-05	-5.213E-05	-4.452E-04	0.0
PF6U	1.172E-04	-9.097E-05	0.0	1.347E-04	-4.017E-03	0.0
PF7U	-2.705E-05	3.233E-05	-3.036E-06	-2.270E-05	-2.511E-03	0.0
PF1L	-8.544E-06	2.914E-06	3.888E-06	-2.624E-07	-1.058E-02	7.008E-03
PF2L	3.058E-06	1.384E-06	-2.384E-06	-2.278E-06	7.030E-02	7.040E-03
PF3L	3.540E-05	0.0	-1.986E-05	-8.057E-06	0.0	0.0
PF4L	1.011E-05	0.0	-1.972E-06	-7.017E-06	0.0	0.0
PF5L	-2.288E-05	1.481E-05	4.959E-05	-5.213E-05	1.150E-01	0.0
PF6L	1.172E-04	-9.097E-05	0.0	1.347E-04	-1.789E-01	0.0
PF7L	-2.705E-05	3.233E-05	-3.036E-06	-2.270E-05	1.698E-02	0.0

Table 4.3-IV (Continued)

H002

	Rout	Rin	Rn	Zn	Zp	Ip
PF1U	-5.359E+01	1.720E+01	2.485E+01	-2.570E+00	-7.659E+01	1.453E+00
PF2U	-5.359E+01	1.720E+01	2.485E+01	-2.570E+00	1.014E+02	1.453E+00
PF3U	3.719E+02	-1.179E+02	-2.282E+02	-1.630E+00	-2.679E+02	1.533E+00
PF4U	-2.807E+02	1.993E+02	1.796E+02	-5.149E+01	2.992E+02	1.559E+00
PF5U	3.900E+01	3.571E+01	2.557E+01	-1.039E+02	-1.196E+02	7.860E-01
PF6U	1.172E+02	-1.136E+02	-2.812E+01	3.144E+01	1.963E+01	6.480E-02
PF7U	-4.022E+01	4.308E+01	-2.335E+01	-5.000E+01	-1.160E+00	5.700E-03
PF1L	-5.359E+01	1.720E+01	2.485E+01	-2.570E+00	3.879E+00	1.453E+00
PF2L	-5.359E+01	1.720E+01	2.485E+01	-2.570E+00	1.791E+00	1.453E+00
PF3L	3.719E+02	-1.179E+02	-2.282E+02	-1.630E+00	7.917E+00	1.533E+00
PF4L	-2.807E+02	1.993E+02	1.796E+02	-5.149E+01	-9.306E+00	1.559E+00
PF5L	3.900E+01	3.571E+01	2.557E+01	-1.039E+02	7.436E+00	7.860E-01
PF6L	1.172E+02	-1.136E+02	-2.812E+01	3.144E+01	-9.930E-01	6.480E-02
PF7L	-4.022E+01	4.308E+01	-2.335E+01	-5.000E+01	3.650E-01	5.700E-03

I002

	Rout	Rin	Rn	Zn	Zp	Ip
PF1U	-3.561E+01	1.140E+01	1.665E+01	-1.680E+00	-5.396E+01	1.453E+00
PF2U	-3.561E+01	1.140E+01	1.665E+01	-1.680E+00	7.478E+01	1.453E+00
PF3U	2.476E+02	-7.900E+01	-1.538E+02	1.580E+00	-1.895E+02	1.533E+00
PF4U	-1.866E+02	1.341E+02	1.240E+02	-3.748E+01	2.093E+02	1.559E+00
PF5U	2.606E+01	-2.450E+01	1.617E+01	-6.760E+01	-8.101E+01	7.860E-01
PF6U	3.640E+01	-3.417E+01	2.254E+01	6.131E+01	1.301E+01	6.480E-02
PF7U	-2.671E+01	2.846E+01	-1.567E+01	-3.319E+01	-5.800E-01	5.700E-03
PF1L	-3.561E+01	1.140E+01	1.665E+01	-1.680E+00	2.428E+00	1.453E+00
PF2L	-3.561E+01	1.140E+01	1.665E+01	-1.680E+00	1.754E+00	1.453E+00
PF3L	2.476E+02	-7.900E+01	-1.538E+02	1.580E+00	4.143E+00	1.533E+00
PF4L	-1.866E+02	1.341E+02	1.240E+02	-3.748E+01	-4.455E+00	1.559E+00
PF5L	2.606E+01	-2.450E+01	1.617E+01	-6.760E+01	4.410E+00	7.860E-01
PF6L	3.640E+01	-3.417E+01	2.254E+01	6.131E+01	-5.330E-01	6.480E-02
PF7L	-2.671E+01	2.846E+01	-1.567E+01	-3.319E+01	3.110E-01	5.700E-03

Table 4.3-V Requirements on coil voltage at EOB 22kA [kV]. Control speed are assumed is follows:

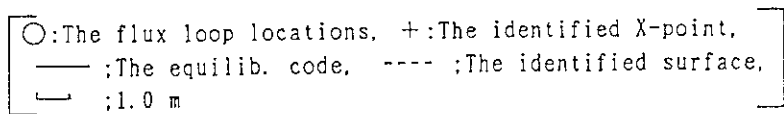$2cm/0.25Hz$ for R_{out}, R_{in}, Z_n, Z_p
$4cm/0.25Hz$ for R_n
$-400kA/0.25Hz$ for I_p
$-0.05/0.25Hz$ for β_p
$-0.01/0.25Hz$ for l_i

	R_{out}	R_{in}	R_n	Z_n	Z_p	I_p	poloidal beta	l_i	REQUIRED (Min.kV)
PF1U	-0.4	0.21	0.35	-0.04	-0.3	2.80	0.0	0.004	+/-2.8
PF2U	0.10	0.12	-0.2	-0.12	0.82	2.82	0.12	-0.18	+/-2.8
PF3U	1.54	-0.1	-1.7	-0.32	-1.3	2.84	0.45	-0.68	+/-2.9
PF4U	0.42	0.02	-0.2	-0.30	-0.4	2.51	0.38	-0.06	+/-2.5
PF5U	-1.2	0.85	4.14	-2.29	0.57	3.11	0.60	1.29	+/-4.2
PF6U	5.77	-4.6	0.04	5.65	-3.2	2.26	-0.85	-4.7	+/-5.9
PF7U	-1.2	1.59	-0.3	-0.91	0.79	1.17	1.58	1.22	+/-1.6
PF1L					-0.17				
PF2L					0.12				
PF3L	(same with above)				0.06	(same with above)			
PF4L					-0.004				
PF5L					0.24				
PF6L					-0.33				
PF7L					0.048				

β=0.1,Type A,η=1.0   β=0.1,Type A,η=0.7   β=1.0,Type A,η=1.0   β=1.0,Type A,η=0.7
(a)   (b)

β=0.1,Type B,η=1.0   β=0.1,Type B,η=0.7   β=1.0,Type B,η=1.0   β=1.0,Type B,η=0.7
(c)   (d)

(e)Type B,η=1.0   (f)Type B,η=1.0

○:The flux loop locations. ＋:The identified X-point.
───:The equilib. code. ----:The identified surface.
└─┘ :1.0 m

Fig. 4.1-1   Identified ITER plasma shape by TOLFEX method and
comparisons of them with the results of equilibrium code.

Plasma initiation & Ip ramp-up with 1MA/s
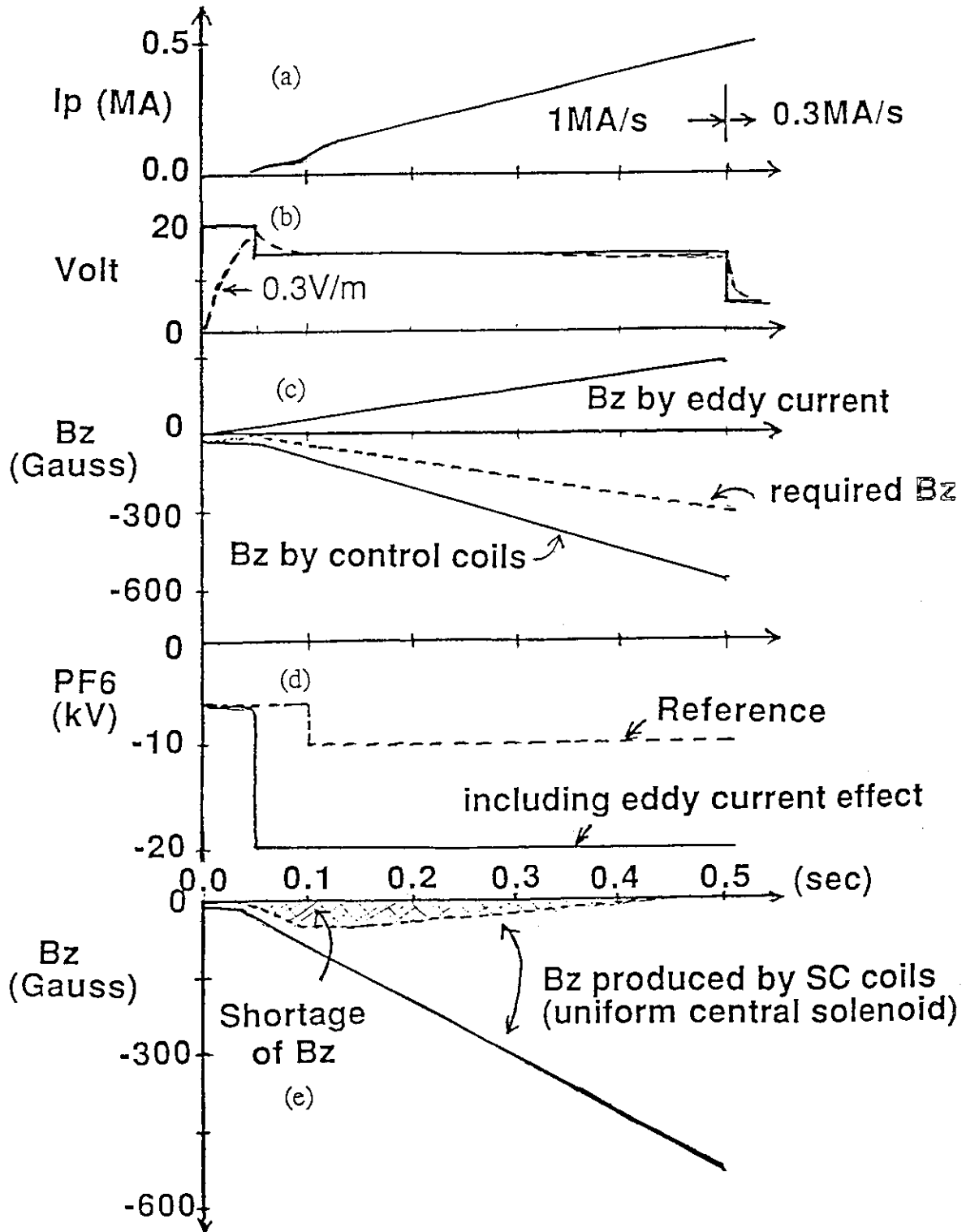
Fig. 4.2-1 General view of the plasma initiation and current ramp-up
with 1MA/s. (a) plasma current, (b) loop voltage, (c) B_z
generated by eddy current and PF coils, (d) voltage of PF6
coil (-10kV is the reference design value without including
the eddy current effect), (e) comparison of the required B_z
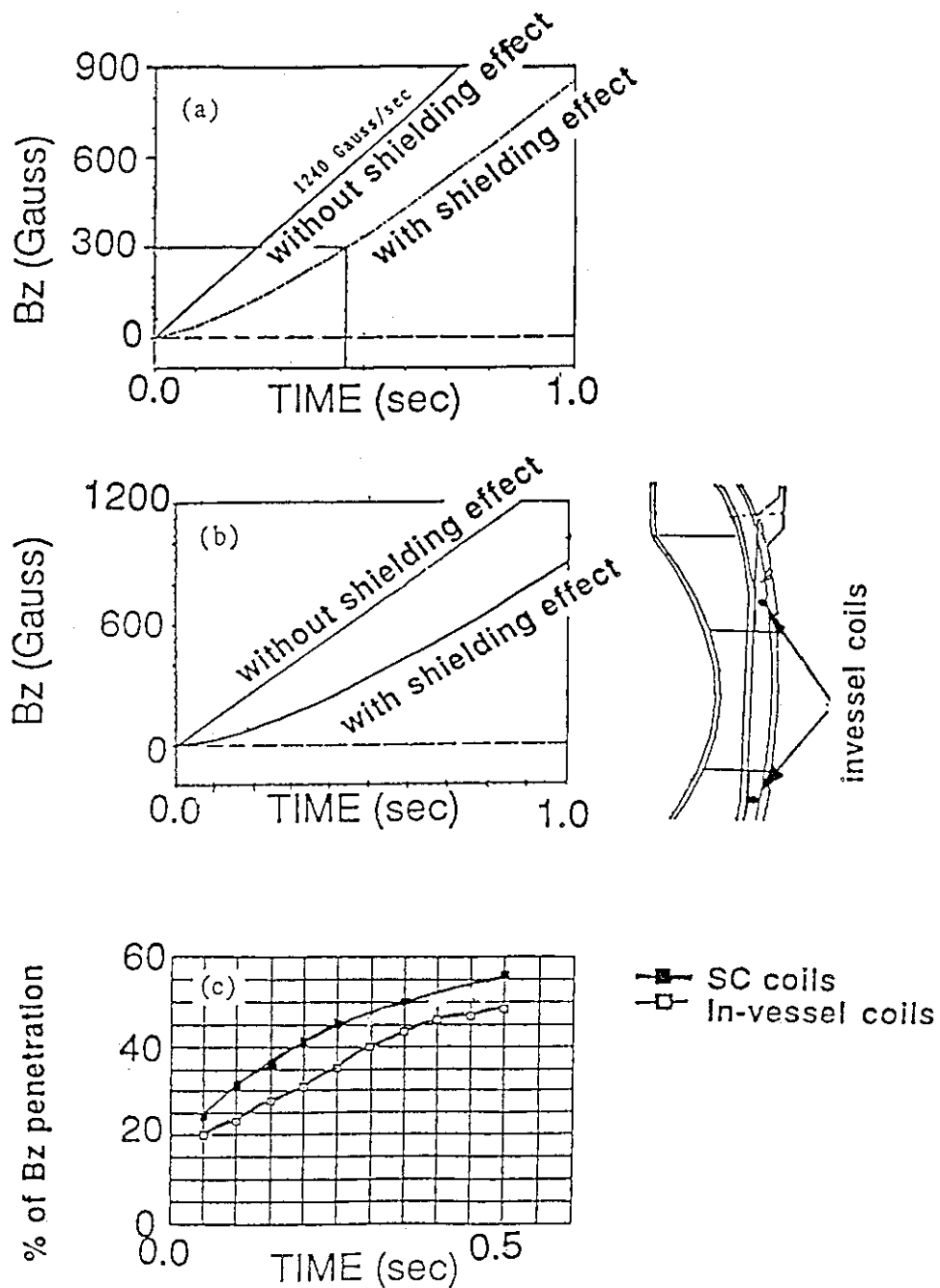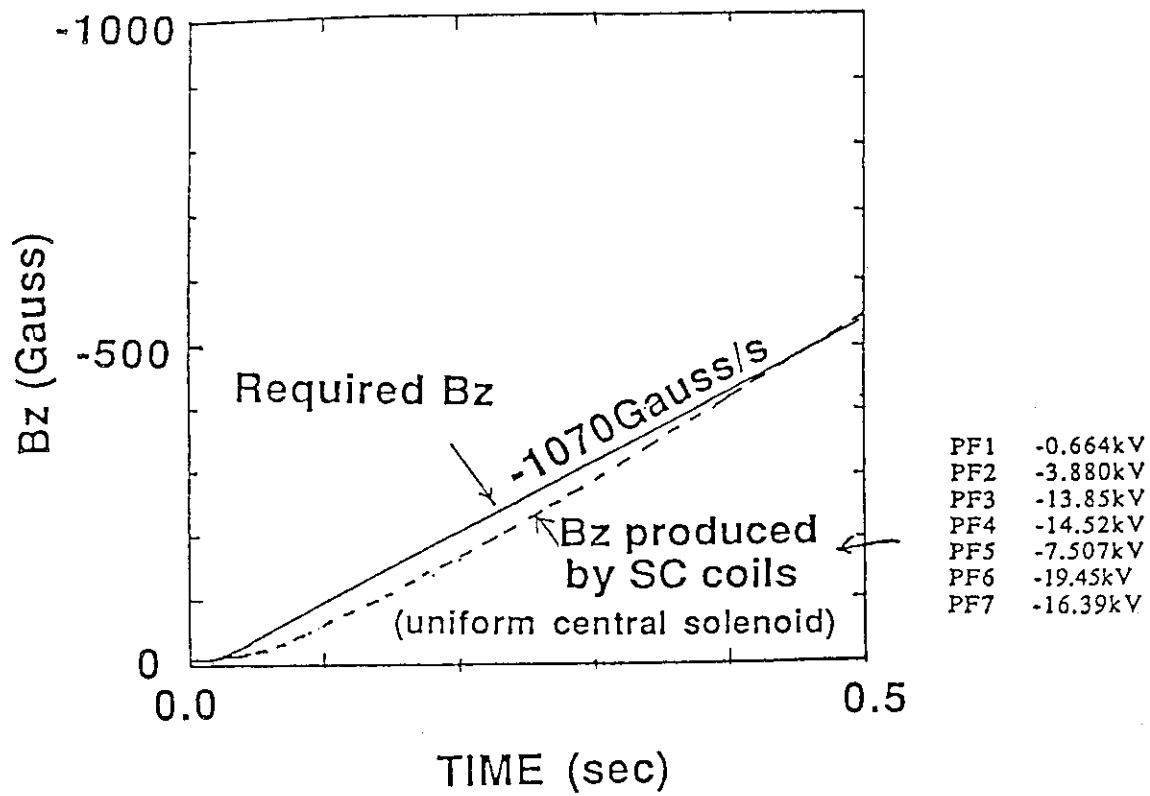and produced B_z.

Fig. 4.2-2   Shielding effect of eddy currents against the penetration
of B_Z.   Penetration of the vertical field with the linear
rampup generated by (a) PF coils and (b) in-vessel coils
installed at R=9.1m, Z=±2.6m (c) percentage of the pene-
trated B_Z compared with the generated B_Z.

	dBz/dt	$(dBz/dt)/(dBz^{req}/dt)$	ΔR from 4.5m
t=0.1sec	-620Gauss/s	57%	+1.4m
t=0.2sec	-820Gauss/s	77%	+0.6m
t=0.3sec	-940Gauss/s	88%	+0.3m
t=0.4sec	-1040Gauss/s	97%	+0.1m
t=0.5sec	-1100Gauss/s	103%	-0.1m

Fig. 4.2-3 Required B_z and produced B_z. Plasma shifts largely to the outside at t=∿0.1 s owing to the shortage of B_z.
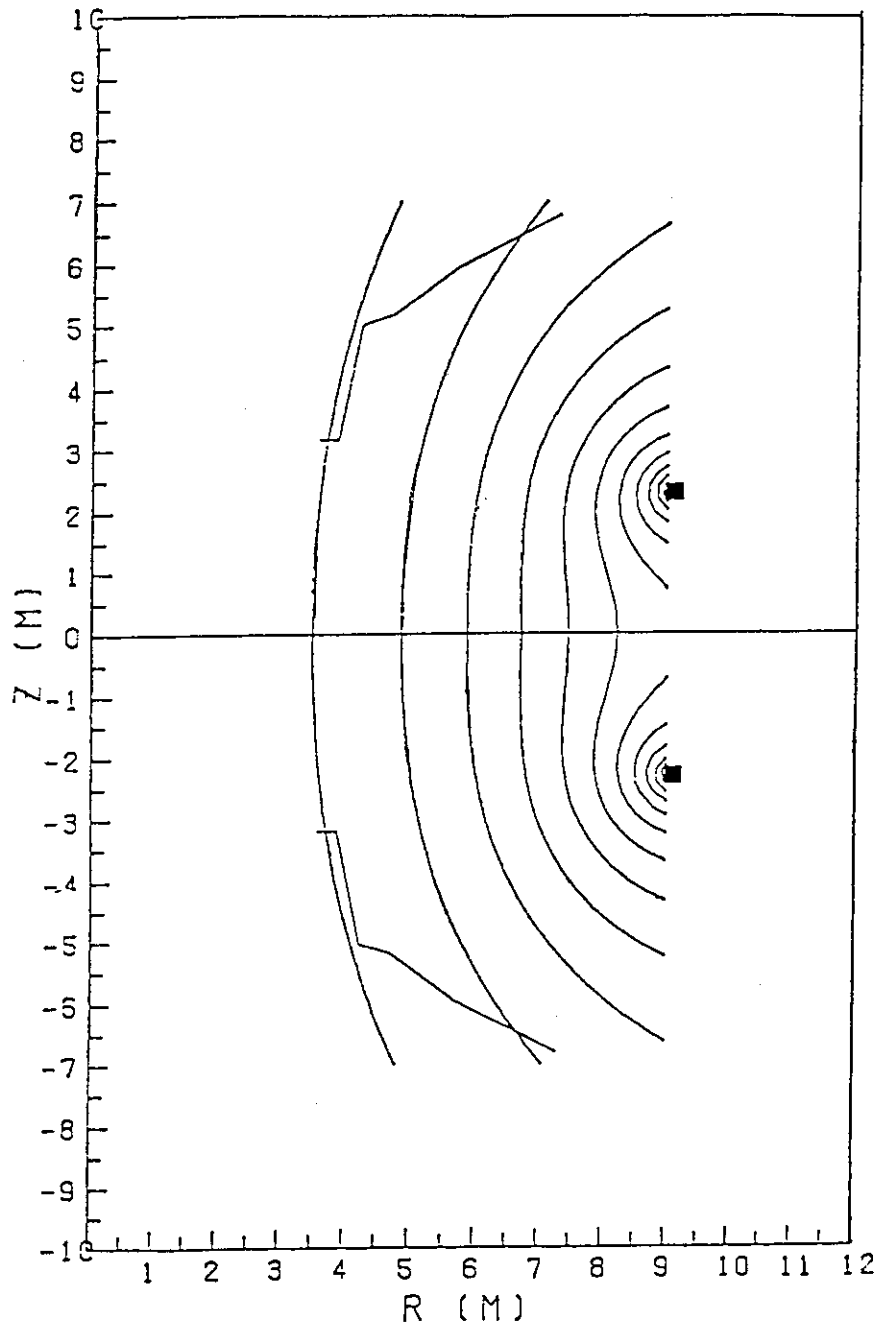
Field Pattern of In-vessel Coils
(150Gauss/100kAT)

Fig. 4.2-4   Field Pattern produced by in-vessel coils at R=0.1m and
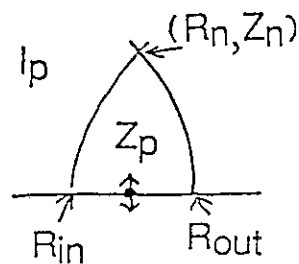Z=±2.6m.

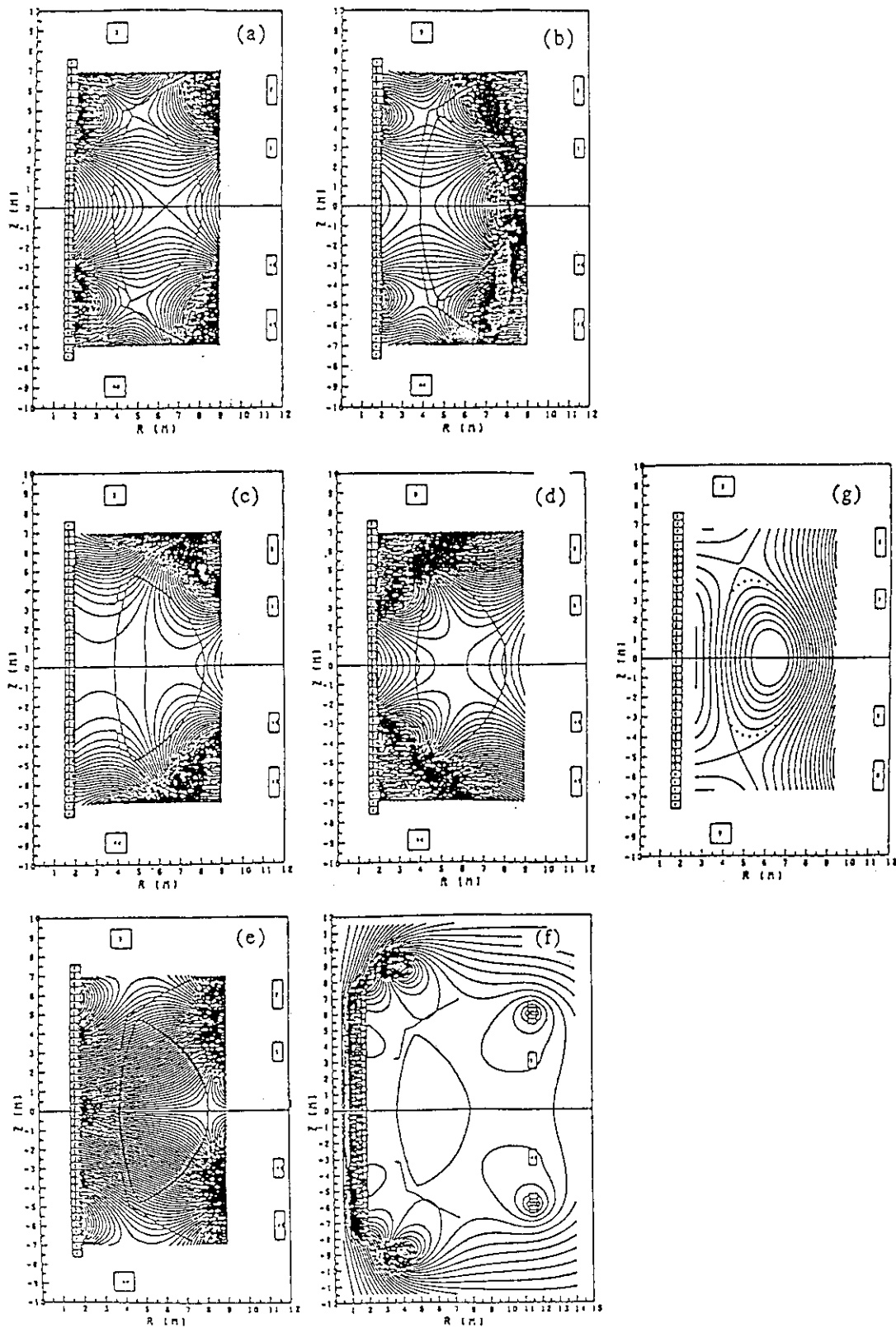Fig. 4.3-1   Control variables in the ITER plasma shape control.

Fig. 4.3-2 Magnetic field pattern to produce the displacement only for
the specified control variable (a) R_{in}, (b) R_{out}, (c) Z_n,
(d) R_n, (e) Z_p, and (f) I_p. (g) shows the Reference plasma
configuration. Plasma parameters of (g) is same with the
of Table 4.3-II.

5. Separatrix sweep and ergodization

5.1 Separatrix sweep

Heat load on the divertor plate is mitigated by the expansion of the flux tube near the null point, and the effect will be assisted further by inclining the divertor plate to the magnetic line of force. Separatrix sweep can be considered as an equivalent broadening of the flux tube or further inclination of the divertor plate, and is one of the credible candidates to mitigate the heat load on the divertor plate.

Although there exist two essential factors in separatrix sweep, i.e., frequency and amplitude of the sweep, product of the above two factors seems to be a decisive parameter, if the amplitude is larger than a certain minimum value decided by the width of the heat flow. The critical values of the above parameters should be decided by completing the time-dependent heat transport analysis of the divertor plate.

Detailed calculation shows that 2-3 Hz-cm with minimum amplitude of 10 cm is considered as a critical value for the heat load of about 15 MW/m^2 in ITER, below which the surface temperature exceeds 1000°C specified as a critical temperature for the occurrence of carbon bloom.

The other important points to be evaluated in the engineering aspect are electric power requirement and AC loss in the super-conducting magnet. Both restrict the upper bound of the frequency and amplitude of the sweep. Benefit of the in-vessel coils, though the coils must be made of normal conductor, must be assessed from this view point.

As the stored energy in the PF6 dominates the major part of the total stored energy, sweep direction, for which ampere-turns of the PF6 are not altered so much, was investigated. Figure 5.1-1 shows the result for the PFC without in-vessel coils together with the cases of various sweep directions. The figure indicates that almost horizontal sweep but somewhat downward (for the upper half plasma) in the radially outside direction is preferable (denoted by open circle).

Table 5.1-I summarizes the change of ampere-turns of the

poloidal field coils for the horizontal null point sweep of 7.5cm by using only poloidal field coils, which correspond to 20cm sweep amplitude on the inclined divertor plate. Large amount of the changes in ampere-turns will cause excessive AC loss in the super conductor of the toroidal and poloidal field coils, even if the electric power requirement is not so large.

In-vessel coils help separatrix sweep much with keeping the electric power requirement and AC loss in the super-conducting magnet relatively low. Co-use of the super-conducting PFC and in-vessel coils with normal conductor is another possibility for the separatrix sweep. Sweeping by in-vessel coils were studied for the ampere-turns combination of Inner/Outer=-2. Table 5.1-II shows a result for the Outer coil amplitude of 150kAT, i.e., Inner of 300kAT. Sweeping amplitude is about 8cm (again, the sweep amplitude on the divertor plate is about 20cm) though the inward sweep is a little larger than the outward sweep. The amplitude has a good linearity for the change in the in-vessel coil ampere-turns. Equilibrium calculation was carried out using fixed boundary flux method which allows changes in the ampere-turns of the poloidal field coils. Since the changes are small, in-vessel coils and the poloidal field coils can be controlled separately.

An example of the sweeping method, which utilizes the maximum allowable current for in-vessel coils, e.g., 150kAT and 75kAT in the inner and outer coils, respectively, and additive super-conducting poloidal field coil currents for the rest of the required currents, was examined. In this method, the in-vessel coil can sweep separatrix by 6.5cm (13cm peak-to-peak) on the divertor plate with frequency up to 1Hz. Super-conducting poloidal field coils give additive sweep with 2.5Hz-cm for slower frequencies. The total sweep amplitude on the divertor plate is as follows;

$d_{Total}=2.5/f+6.5$ (cm) ,

where f is the sweeping frequency by SC coils.

In either of the sweeping scheme, AC loss will be most restricting constraints, and detailed calculation must be performed on AC loss before specifying definite design guideline for sweeping.

5.2 Ergodization [9]

Ergodic magnetic layer (EML) near the separatrix produced by some inherent or intentionally produced error field will broaden the power scrape-off width and then mitigate the maximum power load per area on the divertor plate. Intentional production of such error field can easily be done in ITER. In fact, the easiest way to produce EML is to use the existing in-vessel coils for vertical position control. Position and size of these in-vessel coils are shown in Fig. 5.2-1. Amplitude and poloidal distribution of the perpendicular component of the error field produced by these coils with 10 kA is shown in Fig. 5.2-2(a). Penetration of this error field into the core plasma is shown in Fig. 5.2-2(b). Ergodized nature of the field line near the separatrix is shown in Fig. 5.2-3. For simplicity, harmonic component of n=1 is taken into account in this evaluation. Figure 5.2-4 shows the ergodized nature of the field line at the divertor plate hitting point. As is obviously seen from Fig. 5.2-4, the ergodic layer clearly has a n=1 structure, since only n=1 component is considered. Actually, there should exist many higher harmonic components, and thus, this structure will become blurred to some extent. In addition, the diffusion process should accelerate this bluring process. However, more fine structure will remain in any case, and the non-uniformity of the power load on the divertor plate could not be avoided. Possible method to avoid this non-uniform power load is to divide the in-vessel coil toroidally in several parts, and to rotate the EML by changing the phase of current in each coil segments. Required rotation speed will be around 1 Hz on the basis of the time constant of temperature rise of the divertor plate, so that this requirement should not be technically a demanding one.

Equivalent diffusion coefficient evaluated by the random kick on electrons due to the error field produced by 10 kA of coil current is about 1 m^2/s. The diffusion coefficient near the edge region of ITER under the H-mode confinement with frequent small amplitude ELM (Edge Localized Mode) is assumed about 2 m^2/s. Thus, the equivalent diffusion coefficient produced by 20 kA of coil current will become comparable to that of background plasmas. Higher coil current than 20 kA will impair the background confinement. Consequently, the maximum allowable coil current will be around 20

kA, which produces about 6 cm of ergodized width on the divertor plate.

Substantial reduction effect of the peak power load on the divertor plate is expected by this EML. Maximum allowable ergodic width on the divertor plate of about 6 cm corresponds to 2.5 mm at the upstream SOL on midplane of the torus. Significant enhancement of the diffusion coefficient within this ergodic width widens the power scrape-off width, which produces the subsequent reduction of the peak power load on the plate. This reduction is more effective, when the original power load profile is more narrow. For instance, power scrape-off width at the midplane becomes only 1.25 mm when physics uncertainties are taken into account in ITER steady state operation mode. EML can assure the minimum power scrape-off width larger than about 2.5 mm, if it is to be implemented in the ITER design. Accordingly, the operation regime of ITER could be widened substantially.

Tbale 5.1-I   Changes in ampere-turns for separatrix sweep by
super-conducting poloidal field coils.

Coil No.	Rc (m)	Zc (m)	ΔR_n=-7.5 cm	ΔR_n=+7.5 cm
PF1	1.58	0.95	-0.55	0.58
PF2	1.58	2.85	0.23	-0.35
PF3	1.58	4.75	1.48	-1.53
PF4	1.58	6.65	1.03	-0.98
PF5	3.9	8.20	-0.86	0.81
PF6	11.50	6.0	-0.56	0.53
PF7	11.50	3.0	0.40	-0.38

Table 5.1-II   Changes in ampere-turns for separatrix sweep by
in-vessel coils.

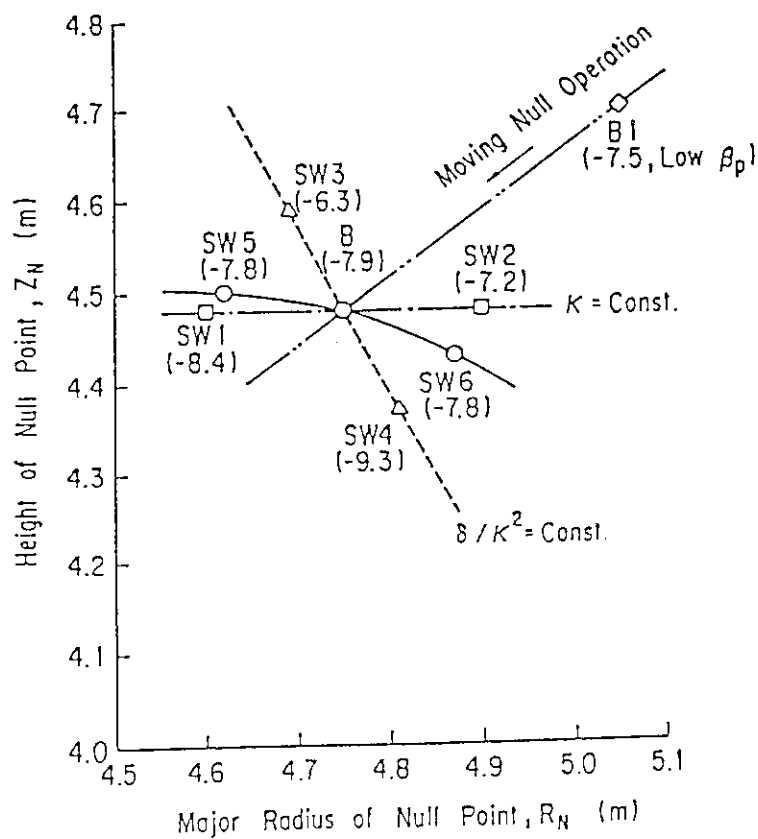| Coil No.	Rc (m)	Zc (m)	ΔR_n=-8.5 cm	ΔR_n=+7.9 cm
Inner	3.5	4.0	0.30	-0.30
Outer	6.5	4.6	-0.15	0.15
PF1	1.58	0.95	-0.06	0.06
PF2	1.58	2.85	-0.03	0.03
PF3	1.58	4.75	0.	-0.01
PF4	1.58	6.65	-0.03	0.02
PF5	3.9	8.20	0.02	-0.02
PF6	11.50	6.0	-0.02	0.02
PF7	11.50	3.0	0.01	-0.09
$\Sigma|I|$			1.0	0.7

Fig. 5.1-1 Loci of the null point for various separatrix sweep of the basic plasma. The direction of the moving null point operation is also shown.
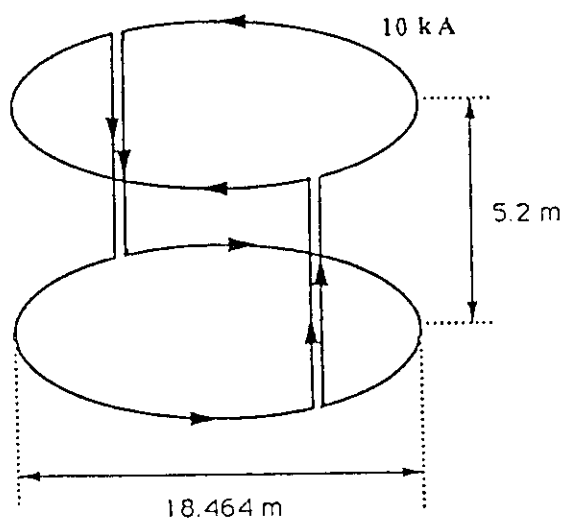

Fig. 5.2-1 Position and size of in-vessel control coils for ITER.
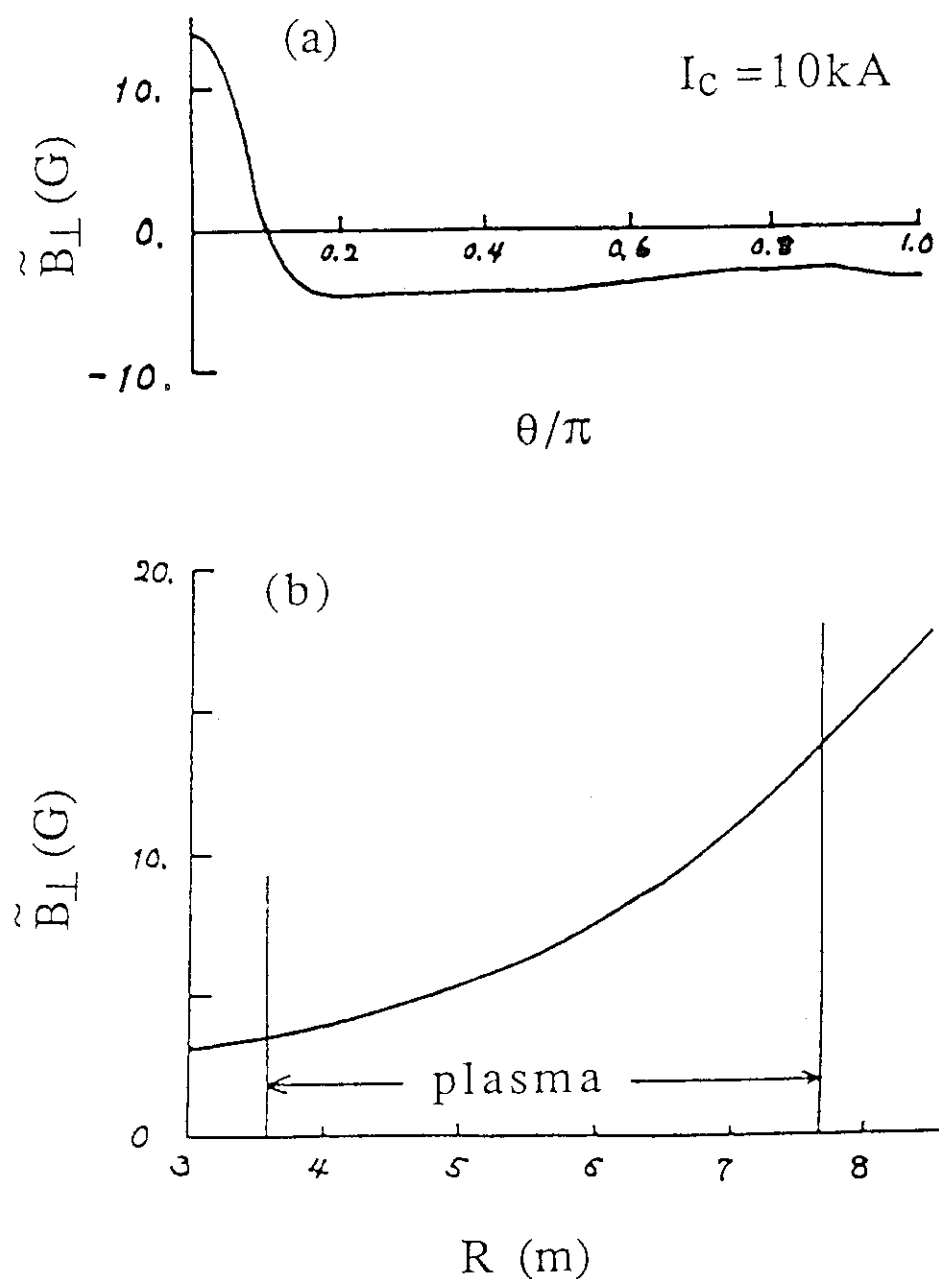
Fig. 5.2-2 (a) Amplitude and poloidal distribution of perpendicular
            component of error magnetic field produced by 10 kA of
            coil current. (b) Radial profile on the midplane of the
            perpendicular component of error magnetic field produced
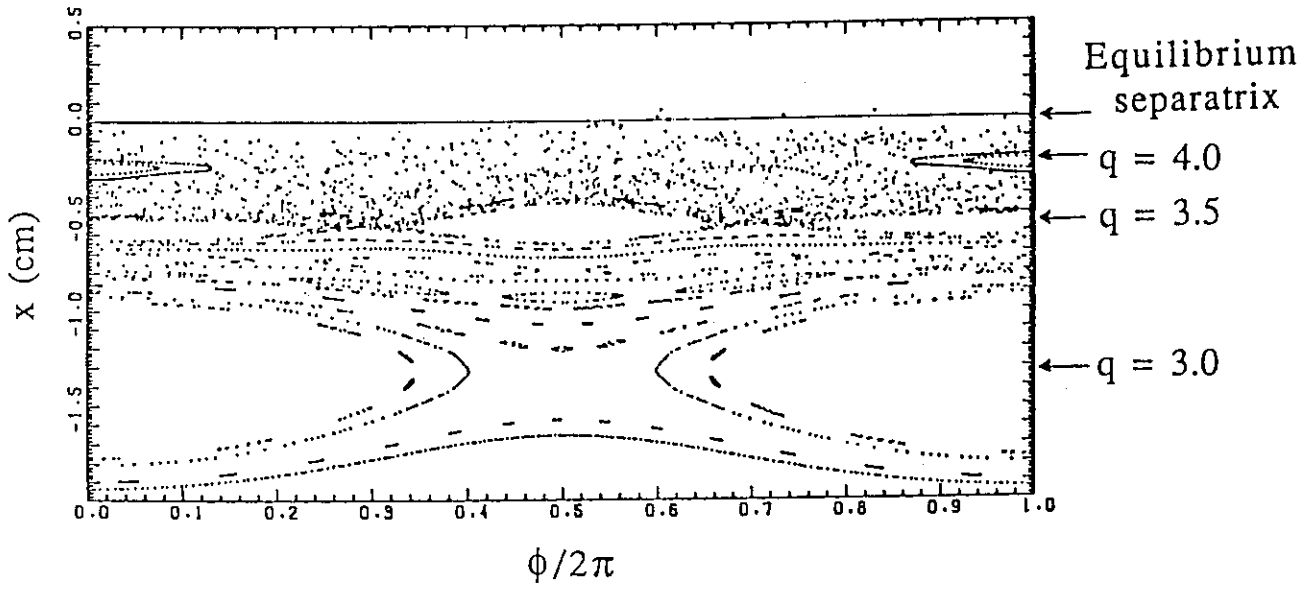   by 10 kA of coil current.

Fig. 5.2-3   Poincare map of magnetic field lines in (ϕ, x) space
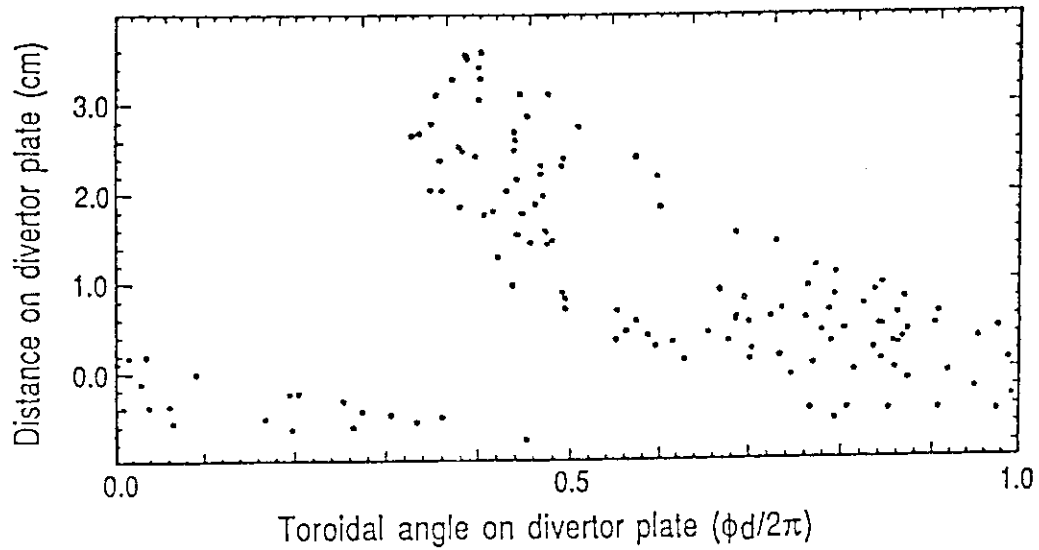on midplane produced by 10 kA of coil current.

Fig. 5.2-4   Ergodized nature of the field line on the divertor
plate produced by 10 kA of coil current.

6. Simulation of plasma dynamic behavior by TSC code

In ITER physics design, the positional instability in vertical direction is considered to be one of the most dangerous MHD instabilities as well as the plasma disruption. It is therefore particularly important to develop a model, which simulates the dynamic behavior of positional instability including the passive stabilizing shell effect as accurately as possible.

In this chapter, we describe the use of $\underline{T}$okamak $\underline{S}$imulation $\underline{C}$ode (TSC)[10] to simulate ITER positional instability in order to predict the instability evolution in a self-consistent manner with stabilizing effect of a vacuum vessel and passive shell.

TSC is a numerical model of a free-boundary axisymmetric tokamak plasma interacting with a set of axisymmetric conductors, that obey circuit equations with active feedback amplifiers included. Modified magnetohydrodynamic equations are solved inside a domain that includes a plasma region, a vacuum region, and a specified number of solid conductors or coils. The interaction of the plasma (motion and current change) with passive conducting structures is treated in a self-consistent manner. TSC code has already been applied to many problems in designing work and experiments [11-14]. One can use the TSC results for the detailed control analysis of plasma position and its shape, and the separatrix separation due to double/single null transition, and so on.

TSC uses an inertial enhancement technique to make the solution of the plasma force balance equation

$$\partial \mathbf{m}/\partial t + \mathbf{F_V(m)} = \mathbf{J} \times \mathbf{B} - \nabla p \, , \qquad (6.1)$$

computationally feasible. Here, $\mathbf{m}$ is the plasma momentum density. The mass and viscosity terms on the left side of Eq. (6.1) are multiplied by enhancement factors chosen to make time integration feasible while keeping the left side of Eq. (6.1) small compared with the terms on the right side. Selected cases must be repeated with smaller enhancement factors to ensure convergence in these quantities.

In the calculations of ITER positional instability, a thermal quench is introduced at $t = 0$ in order to lose the stability of initial

equilibrium. In our TSC simulation, the plasma current is forced to hold almost constant throughout the period of instability process by feedback control of plasma current.

Figure 6-1 illustrates TSC computational domain and configurations of ITER poloidal field coil systems. The coil series external to the TSC computational grid are ITER poloidal field coil system. These coil currents were considered to be unchanged throughout the period of time-evolution in our TSC simulation. Conducting structures internal to the grid were represented by a series of passive filamentary wires with specified resistivity and inductance, which are listed in Table 6-I. Each filamentary wire is disconnected from other wires. The inner C-shaped group of wires indicates a part of vacuum vessel. The rest part of vacuum vessel is neglected here, since this part is located far from the plasma. The axisymmetric TSC code can evaluate the induced poloidal current on a vacuum vessel together with the toroidal current due to poloidal flux changes. One source of the poloidal current can be estimated from change of the plasma paramagnetic flux during a thermal quench. However, in the present TSC model the poloidal current flowing on the vacuum vessel is not allowed, because the vacuum vessel is disconnected along the poloidal direction. The outer group of wires indicates a passive shell to stabilize vertical displacement of positional instability. The circuit constants of the coil series internal to the computational grid in Table 6-I are adjusted so that they become equal to those of actual shell. Typical L/R times of wires are estimated to be 10-25 msec. The sizes of Cartesian grid are 18 cm and 25 cm in the radial and vertical directions, respectively.

Figure 6-2 shows the obtained poloidal flux contour for an initial equilibrium (I_p=22MA, β_p=0.68, p_0=2.09 $\times 10^6 N/m^2$, n_0=3.3 $\times 10^{20}/m^3$, T_0=18.9keV). The density profile and the pressure profile are assumed as $n=n_0\Psi^{1/2}$ and $p=p_0\Psi^{3/2}$, respectively. Here, $\Psi(=(\Psi-\Psi_s)/(\Psi_{axis}-\Psi_s))$ is the normalized poloidal flux. Also shown is the Ψ-value on a midplane.

For the simulation of vertically unstable plasma, an initial vertical displacement was introduced by amount of 1 cm below midplane. After the convergence to this initial equilibrium, that was used as a starting point for the development of vertical instability, we introduced the thermal quench as shown in Fig. 6-3, which was

initiated by enhancement of the plasma thermal conductivity by magnitude of 3×10^5. The thermal quench phase typically lasts for 500 μs-1.0 msec ; during this time, beta decreases by magnitude of 5 $\times 10^2$, and the magnetic axis of plasma moves inward by 50 cm. The thermal quench with 50 cm radial shift also causes a vertical displacement of magnetic axis by amount of 3 cm below midplane mainly due to the magnetic interaction between outer passive shell and plasma being asymmetric about midplane. These transient behaviors are illustrated in Fig. 6-4, where time evolution of the position of magnetic axis is shown (ZMAG and XMAG denote the vertical and radial position of magnetic axis, respectively).

From Fig. 6-4, it is observed that the time evolution of vertically moving plasma due to positional instability after thermal quench. The time evolution until $t = 60$ msec is followed and the magnetic axis at that time is 30 cm below midplane, while the radial position remains almost unchanged as 5.5-5.6 m. The converged growth rate of vertical instability is estimated to be 30/sec, which is considered to be reasonable compared with the adopted L/R time constant of wires. Plasma current is also kept constant (22MA) as shown in Fig. 6-5. Each of the trajectories of plasma current in Fig. 6-5 are evaluated by different ways, that is, Ampere's law on grid boundary and the full volume integral of plasma region. It is to be desired that they should be coincident to each other throughout the entire period of TSC simulation. Time-history of toroidal current profile are also shown in Fig. 6-6.

Figure 6-7 shows the time evolution of positions of the upper and lower X-points (NULLRU and NULLZL denote radial and vertical position of the X-point, respectively. The symbols U and L in both figures indicate upper and lower X-points, respectively). It is seen that the radial positions of upper and lower X-points are almost same during the simulation after thermal quench. On the other hand, the asymmetry of vertical positions with respect to midplane becomes larger as the time elapses. This indicates that the positional instability causes the double/single null transition of separatrix. Figure 6-8 shows snapshots of the computed poloidal flux contour and velocity field on a poloidal plane at different times $t = 2.6, 7.7, 15.2, 58.4$ msec during the evolution of positional instability.

In order to study precisely the undesirable plasma boundary

contact with a wall and the double/single null transition of separatrix, we need the detail of plasma boundary shape throughout the development of positional instability rather than the location of magnetic axis. Interpolation is difficult to find precise locations of wall contacting surface and X-point, because the grid size in the present calculation is 18-25 cm at the moment.

Future works are summarized as follows;

• Initial vertical offset *vs* rapid vertical displacement due to the thermal quench from a viewpoint of plasma control accuracy

• More precise simulation of plasma boundary contact with a wall from a viewpoint of plasma control accuracy

• Quantitative study on vertical location of magnetic axis *vs* double /single null transition characteristics

• TSC model improvement of ITER conducting structures

• Simulation of major disruption process

The efforts to perform the future works mentioned are now under way.

Table 6-I The circuit constants of coil series internal to the computational grid : These equivalent TSC circuit constants were adjusted so that they were equal to the ones of actual geometric shell.

R (m)	Z (m)	Resistance (Ω)	Inductance (μH)
4.5	6.85	8.22×10^{-4}	18.8
4.0	6.75	7.31×10^{-4}	16.1
3.7	6.25	6.76×10^{-4}	14.5
3.4	5.75	6.21×10^{-4}	13.0
3.2	5.25	5.84×10^{-4}	12.0
3.1	4.50	2.83×10^{-4}	9.61
3.1	3.50	2.83×10^{-4}	9.61
3.1	2.50	2.83×10^{-4}	9.61
3.1	1.50	2.83×10^{-4}	9.61
3.1	0.50	2.83×10^{-4}	9.61
3.1	-0.50	2.83×10^{-4}	9.61
3.1	-1.50	2.83×10^{-4}	9.61
3.1	-2.50	2.83×10^{-4}	9.61
3.1	-3.50	2.83×10^{-4}	9.61
3.1	-4.50	2.83×10^{-4}	9.61
3.2	-5.25	5.84×10^{-4}	12.0
3.4	-5.75	6.21×10^{-4}	13.0
3.7	-6.25	6.76×10^{-4}	14.5
4.0	-6.75	7.31×10^{-4}	16.1
4.5	-6.85	8.22×10^{-4}	18.8

(axisymmetric wires for a part of vacuum vessel)

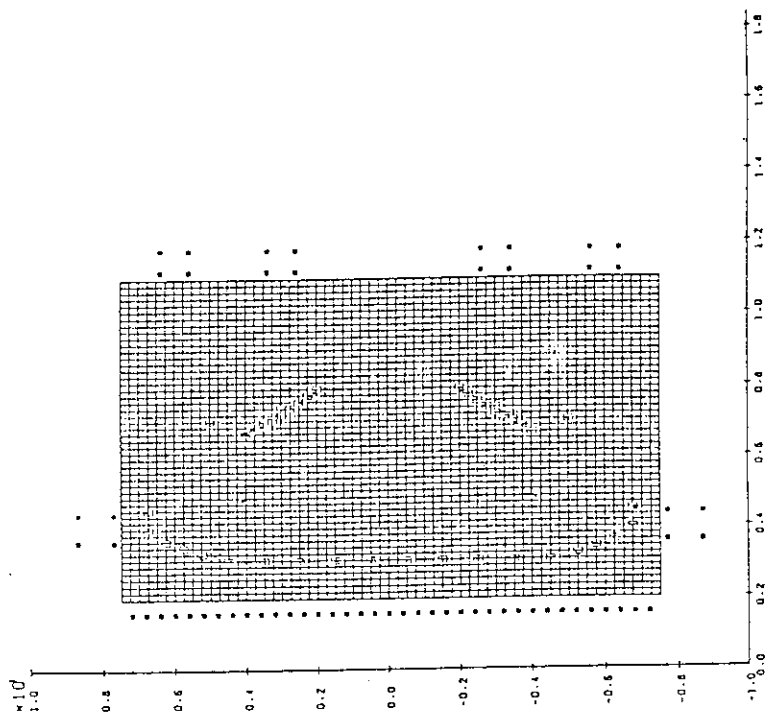| R (m)	Z (m)	Resistance (Ω)	Inductance (μH)
6.70	4.0	4.18×10^{-3}	38.2
6.83	3.78	4.26×10^{-3}	39.1
6.96	3.56	4.34×10^{-3}	40.0
7.09	3.34	4.42×10^{-3}	40.9
7.22	3.12	4.50×10^{-3}	41.8
7.35	2.90	4.59×10^{-3}	42.8
7.48	2.68	4.67×10^{-3}	43.7
7.61	2.46	4.75×10^{-3}	44.6
7.74	2.24	4.83×10^{-3}	45.5
7.87	2.02	4.91×10^{-3}	46.5
7.87	-2.02	4.91×10^{-3}	46.5
7.74	-2.24	4.83×10^{-3}	45.5
7.61	-2.46	4.75×10^{-3}	44.6
7.48	-2.68	4.67×10^{-3}	43.7
7.35	-2.90	4.59×10^{-3}	42.8
7.22	-3.12	4.50×10^{-3}	41.8
7.09	-3.34	4.42×10^{-3}	40.9
6.96	-3.56	4.34×10^{-3}	40.0
6.83	-3.78	4.26×10^{-3}	39.1
6.70	-4.0	4.18×10^{-3}	38.2

(axisymmetric wires for passive shell)

Fig. 6-1 Computational domain and configurations of ITER poloidal field coil systems : The coil series external to the TSC computational grid are ITER poloidal field coil system. These coil currents were considered to be unchanged throughout the period of time-evolution. Conducting structures internal to the grid were represented by a series of passive filamentary wires of specified resistivity and inductance. The inner C-shaped group of wires indicates a part of vacuum vessel. The outer one indicates a passive shell to stabilize vertical displacement of positional instability.
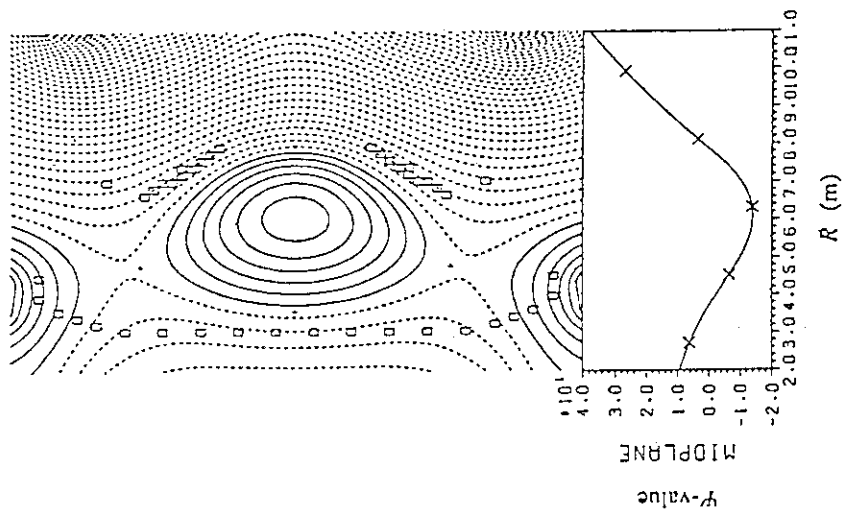
Fig. 6-2 Poloidal flux contour for an initial equilibrium (I_p=22MA, β_p=0.68, p_0=2.09×10^6N/m^2, n_0=3.3×10^{20}/m^3, T_0=18.9keV). The density profile and the pressure profile are assumed as $n=n_0\psi^{1/2}$ and $p=p_0\psi^{3/2}$, respectively. Here, $\psi(=(\psi-\psi_s)/(\psi_{axis}-\psi_s))$ is the normalized poloidal flux. Also shown is the ψ-value on a midplane.
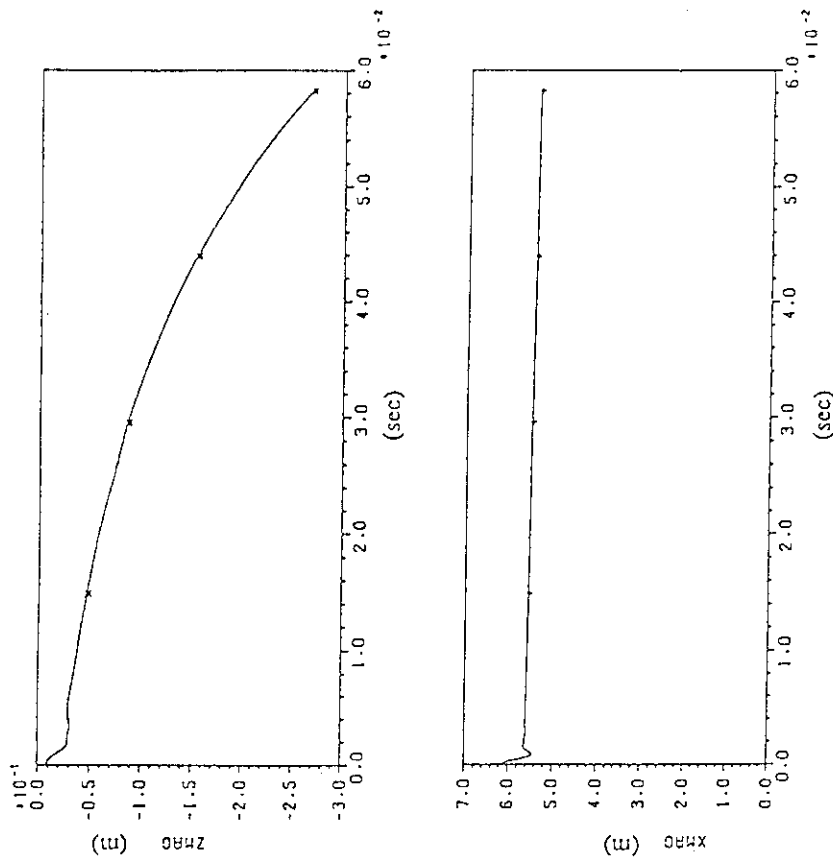
Fig. 6-4 Time-history of the position of magnetic axis (ZMAG and XMAG denote the vertical position and radial position of magnetic axis, respectively). Growth rate of vertical instability was estimated to be 30/sec.
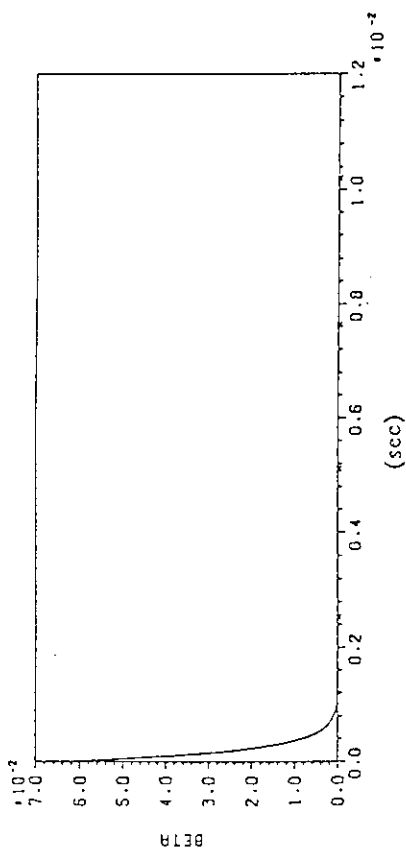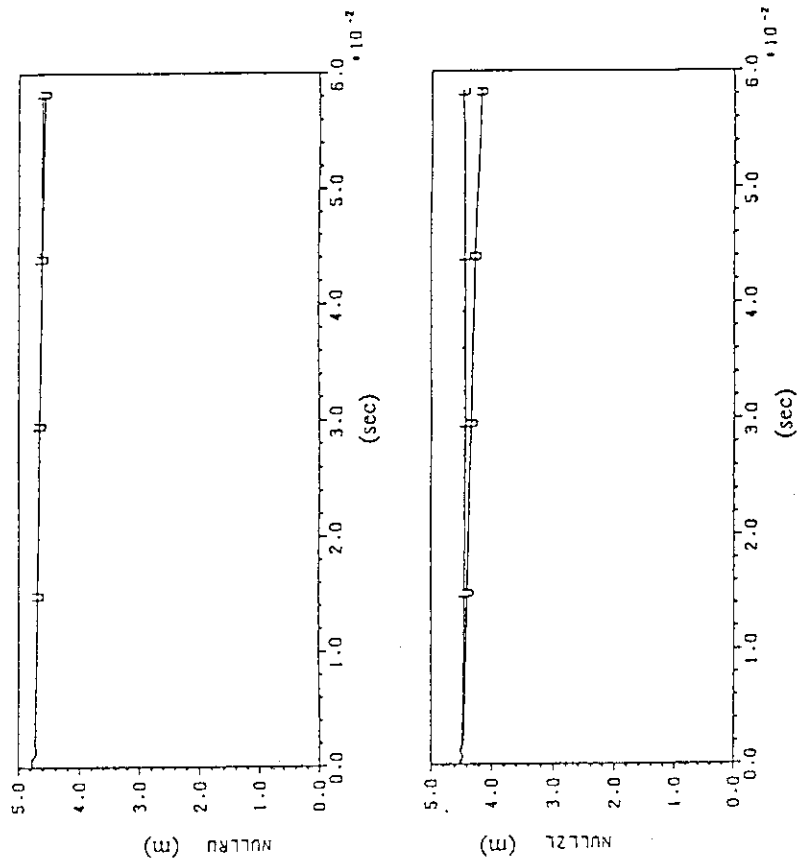

Fig. 6-3 βp perturbation for simulation of vertically moving plasma : The thermal quench was initiated by enhancement of the plasma thermal conductivity.
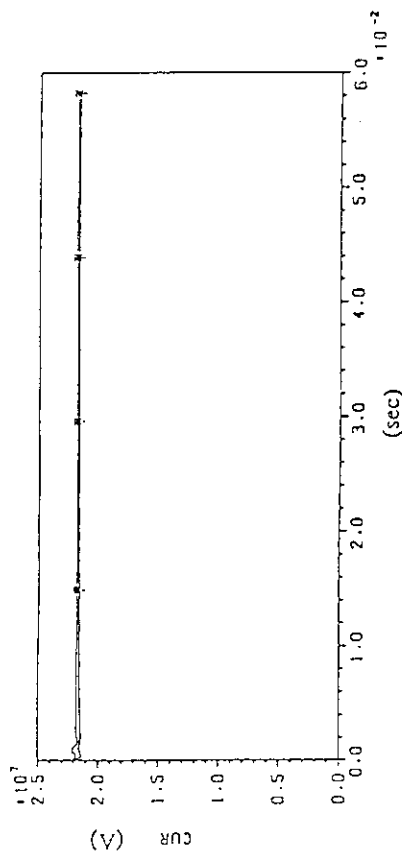
Fig. 6-5 Time-evolution of plasma current. Two trajectories of plasma current are the ones evaluated by different ways, that is, Ampere's law on grid boundary and the full volume integral of plasma region. It is to be desired that they should be close proximity to each other throughout the entire period of TSC simulation.

Fig. 6-7 Time-evolution of positions of the upper and lower X-points (NULLRU and NULLZL denote radial position and vertical position, respectively. The symbols U and L in both figures indicate upper and lower X-points, respectively).
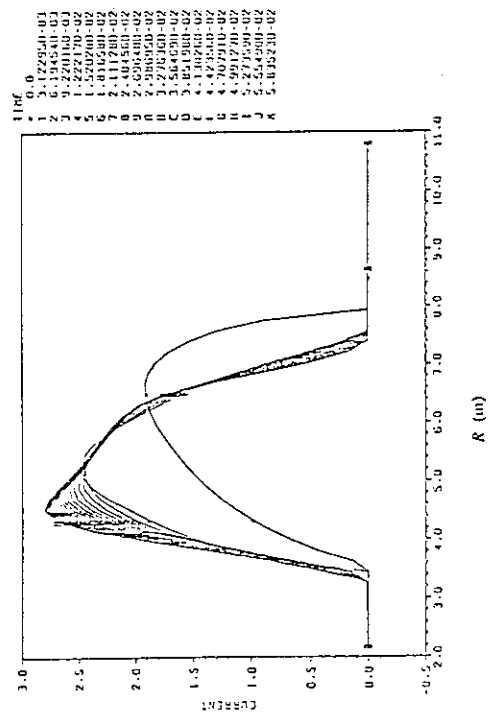
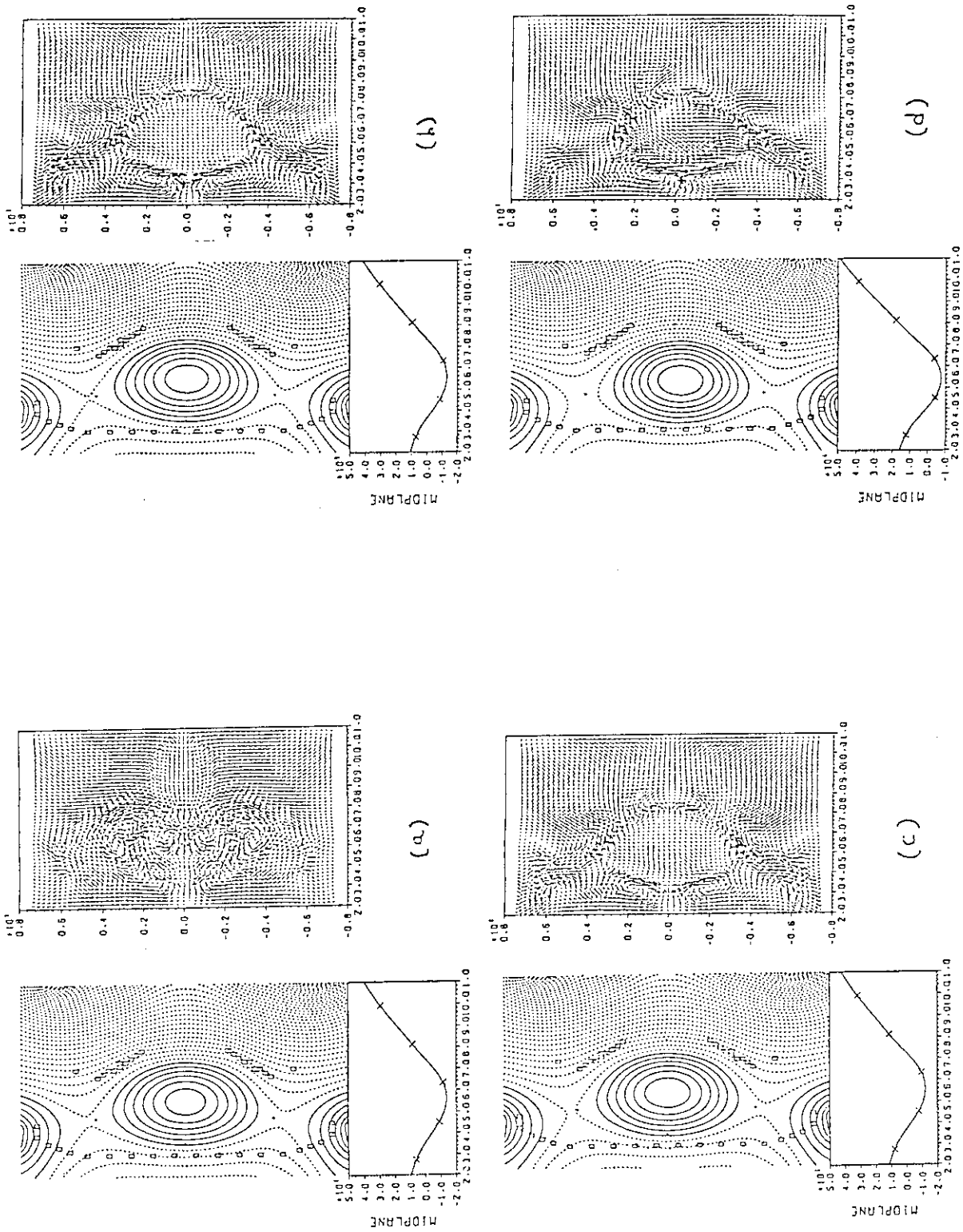Fig. 6-6 Time-development of toroidal current profile.

Fig. 6-8 Snapshots of poloidal flux contour and velocity field on a poloidal plane at 2.6 msec (a), 7.7 msec (b), 15.2 msec (c), and 58.4 msec (d) after the thermal quench.

7. Summary

Major Japanese contributions of the poloidal field systems design to the ITER CDA during past three years are presented. Many of the results have made large contribution to the CDA and, in fact, have been incorporated into the CDA final report. Many of the results are not fully complete yet, while should be sufficient to demonstrate the feasibility of the CDA design. The studies are to be continued and deepened in future.

7. Summary

Major Japanese contributions of the poloidal field systems design to the ITER CDA during past three years are presented. Many of the results have made large contribution to the CDA and, in fact, have been incorporated into the CDA final report. Many of the results are not fully complete yet, while should be sufficient to demonstrate the feasibility of the CDA design. The studies are to be continued and deepened in future.

References

[1] Y.Shimomura, et al., "ITER Poloidal Field System", IAEA/ITER/DS/27, IAEA, Vienna (1991).

[2] K. Shinya, M. Sugihara, S. Nishio, "Study on Poloidal Field Coil Optimization and Equilibrium Control of ITER", JAERI-M89-028 (1989).

[3] ITER Specialists' Meeting on P.F. System and operation scenario,Conclusions on session B, Garching 24-27 May 1988.

[4] M. Yamane, E. Coccorese, A. Kameari, M.Sugihara ; Passive control of Vertical Instabilities in ITER, IAEA/ITER/DS/4, IAEA, Vienna (1989).

[5] K. Kurihara, T. Kimura, M. Takahashi, Y. Kawamata, S. Sakata et al., 'Tokamak Plasma Shape Identification with a Legendre-Fourier Expansion of the Vacuum Poloidal Flux Function in the Toroidal Coordinates', JAERI-M90-001 (1990) (in Japanese).

[6] K. Kurihara,'Improvement of Tokamak Plasma Shape Identification with a Legendre-Fourier Expansion of the Vacuum Poloidal Flux Function', to be published in Fusion Technology.

[7] R.Yoshino et al., "Control of Divertor Configuration in JT-60", Proc. 13th Symp. on Fusion Technology, Vol.1, (1984) 483.

[8] R.Yoshino et al., "Control of the Plasma Configuration in ITER", JAERI-M 91-049 (1991).

[9] M.Azumi, T.Takizuka, M.Sugihara, M.Shimada, Y.Shimomura, "Reduction of heat load at the divertor plate by magnetic field perturbation with in-vessel coils", ITER-IL-PH-13-0-J-5 (1990).

[10] S. C. Jardin, N. Pomphrey, and J. Delucia, "Dynamic Modeling of Transport and Positional Control of Tokamaks," J. Comput. Phys. 66, 481 (1986).

[11] B. J. Merrill and S. C. Jardin, "DSTAR : A Comprehensive Tokamak Resistive Disruption Model for Vacuum Vessel Components," Fusion Eng. Des. 5, 235 (1987).

[12] R. O. Sayer, Y-K. M. Peng, and S. C. Jardin, "Disruption-Induced Forces. on a Vacuum Vessel from TSC Poloidal Eddy Currents," Bull. Am. Phys. Soc. 33, 1972 (1988).

[13] S. C. Jardin et al., "Modeling of Post-Disruptive Plasma Loss in the Princeton Beta Experiment," Nucl. Fusion 27, 569 (1987).

[14] R. O. Sayer, Y-K. M. Peng, D. J. Strickler and S. C. Jardin, "TSC Disruption Scenarios and CIT Vacuum Vessel Force Evolution," ORNL/FEDC-89/3, (1990).